DOE/ER/40757--076

UTEXAS-HEP-95-20
KL-460H

The University of Texas at Austin
Department of Physics

All Strange and Terrible Events: A Search for the H Dibaryon

Brent Ware

December 1995

RECEIVED
JUN 27 1996
OSTI

DISCLAIMER

This report was prepared as an account of work sponsored by an agency of the United States Government. Neither the United States Government nor any agency thereof, nor any of their employees, makes any warranty, express or implied, or assumes any legal liability or responsibility for the accuracy, completeness, or usefulness of any information, apparatus, product, or process disclosed, or represents that its use would not infringe privately owned rights. Reference herein to any specific commercial product, process, or service by trade name, trademark, manufacturer, or otherwise does not necessarily constitute or imply its endorsement, recommendation, or favoring by the United States Government or any agency thereof. The views and opinions of authors expressed herein do not necessarily state or reflect those of the United States Government or any agency thereof.

MASTER

Department of Energy Grant DE-FG03-93ER40757-076

DISTRIBUTION OF THIS DOCUMENT IS UNLIMITED

All Strange and Terrible Events:
A Search for the H Dibaryon

Approved by
Dissertation Committee:

Supervisor: _____

_____

_____

_____

_____

© Copyright
by
Carlton Brent Ware
1995

"All strange and terrible events are welcome,
But comforts we despise."
William Shakespeare, Antony and Cleopatra

"Poverty has strange bedfellows."
Edward George Bulwer-Lytton, Baron Lytton 1803–1873, The Caxtons

"Three monkeys, ten minutes."
Dogbert, Dilbert

All Strange and Terrible Events: A Search for the H Dibaryon

by

Carlton Brent Ware, BSEE, MSEE

Dissertation
Presented to the Faculty of the Graduate School of
The University of Texas at Austin
in Partial Fulfillment
of the Requirements
for the Degree of

Doctor of Philosophy

The University of Texas at Austin
December 1995

Acknowledgements

As with all high-energy physics experiments in these latter days following the demise of the SSC, E888 was the combined work of many people. In particular, the following people should be thanked. Val Fitch came up with the idea for this experiment, and Alan Schwartz and Bob Cousins took the ball and ran with it. Alan's and Bob's effort and Val's imprimatur pushed it through the approval process and convinced a busy group of E791/E871 collaborators that this experiment was worth wasting protons on. Alan also gently corrected many of my physics misconceptions and steered me onto right paths as the leader of the analysis.

Thanks go to the E791/E871 collaborators for their forbearance and hard work on this project when they might have been working on their own experiment, but instead made the sacrifice of time and effort for new physics data. Special mention should be made of Jim McDonough, Steve Kettell, Milind Diwan, and Virgil Highland, who went above and beyond the call of duty as their normal mode of operation. Virgil will be missed, proof that you can be a nice guy *and* a good high-energy physicist. Ralph Brown, Freddie Kobaciuk, the AGS machine shop crew, Steve Pendola and Jackie Timko gave lie the canard about rude, unhelpful New Yorkers, cheerfully getting things done. Various Brookhaven personnel loaned me tools, materials, and expertise graciously. Not everyone did, so those who did were appreciated.

I'd especially like to thank my friends and colleagues. Josh Klein made the original presentation to E871 proposing the use of their experiment to search for the H, and made a cold, wet, dismal February at Brookhaven rebuilding drift chambers with limited resources tolerable and even fun ("Start spreading the news, I'm leaving today..."). Karl Ecklund has been an invaluable source of code and support, making things run on the Princeton IBM. Steve Worm let me throw darts in his office and has been a sounding board for my physics problems. Scott Graessle listened to my griping and encouraged me to keep working at this endeavor, and patiently answered my Unix questions. James Lee has been a friend for many years, patient and more confident in me than I was in myself. My parents provided moral support.

There are many others who should be thanked individually for their support and friendship, fellow graduate students and post-docs who suffered with me, and friends who kept my head above water, but there isn't room enough.

If nothing else, I discovered climbing during my tenure at UT. That made it all worthwhile. Thanks to my climbing partners, too numerous to mention by name. Climbing kept me sane, and you made it fun to go. I redpointed my first 5.12, *Liposuction*, July 30, 1995, and did my first big wall (*The Prow*, 5.7 A2+) September 23-26, 1995, so I can graduate now.

All Strange and Terrible Events:
A Search for the H Dibaryon

Publication No. _____

Carlton Brent Ware, Ph.D.
The University of Texas at Austin, 1995

Supervisor: Jack Ritchie

No six-quark bound hadron, (other than the loosely bound deuteron) has been observed, despite several experimental searches. Some models of quark dynamics predict the existence of such a state, the doubly-strange six-quark H dibaryon ($uuddss$) being the most likely. The mass of the H would be between that of the deuteron and the $2m_\Lambda$ strong interaction decay threshold. In 1992, Experiment E888 at Brookhaven National Lab's Alternating Gradient Synchrotron collected data to search for this particle. The detector consisted of a two-arm spectrometer with drift chamber tracking and two magnets for momentum analysis, scintillator hodoscope triggering, Čerenkov particle identification, an electromagnetic calorimeter, and a muon hodoscope and rangefinder. The experiment searched for the decay $\Lambda \rightarrow p\pi^-$ from the weak decays of $H \rightarrow \Lambda n$ and $H \rightarrow \Sigma^0 n$ (followed by $\Sigma^0 \rightarrow \Lambda\gamma$). This search was sensitive to weakly decaying H dibaryons with lifetimes from 6-230 ns with production cross-sections greater than ~ 2 μb/steradian.

Table of Contents

Acknowledgements v

Abstract vii

List of Tables xii

List of Figures xiii

Chapter 1. H Theory 1
1.1 Phenomenological Models 3
1.1.1 Bag model 4
1.1.2 Lattice QCD 5
1.1.3 Skyrmions 6
1.1.4 Other models 7
1.2 Lifetime of the H 9
1.3 H Production 12
1.4 Other Multiquark States 14

Chapter 2. Other Searches 18
2.1 Past Searches 19
2.1.1 Collision experiments 19
2.1.2 Hypernuclei H experiments 22
2.1.3 Double weak decays of nuclei 24
2.2 Current Searches 25
2.2.1 Collision experiments 25
2.2.2 Heavy ion experiments 26

Chapter 3. Experimental Apparatus 28
3.1 History . . . 28
3.1.1 Experimental overview . . . 31
3.2 Two phases: He-N_2 and Freon . . . 33
3.3 Target and Beam . . . 35
3.4 Tracking Detectors . . . 39
3.4.1 Trigger scintillators . . . 39
3.4.2 Spectrometer . . . 40
3.5 Particle Identification . . . 45
3.5.1 Čerenkov counters . . . 45
3.5.2 Lead-glass calorimeter . . . 48
3.5.3 Muon hodoscope . . . 51
3.5.4 Muon rangefinder . . . 51

Chapter 4. Data Acquisition System 53
4.1 Overview . . . 53
4.2 Trigger . . . 55
4.2.1 Level 0 and Level 1 . . . 55
4.2.2 Level 3 . . . 59
4.3 Event Readout . . . 60
4.4 Online . . . 61
4.5 Monitoring . . . 62
4.6 Digitization . . . 62
4.6.1 ADCs . . . 62
4.6.2 TDCs . . . 64
4.6.3 Latches . . . 65

Chapter 5. Analysis 66
5.1 Sensitivity of the Experiment . . . 67

Chapter 6. Offline 70
6.1 Monte Carlo . . . 73
6.2 Pattern Recognition . . . 75
6.3 Fitting . . . 78

Chapter 7. Data Reduction 81
7.1 Pass 1 . . . 82
7.2 Event Strips . . . 85

Chapter 8. Background 87
8.1 Backgrounds . . . 88
8.1.1 Lambda daughters . . . 88
8.1.2 Kaons . . . 89
8.1.3 Secondary neutral interactions . . . 91
8.2 Background Estimation . . . 96
8.2.1 Counting kaons . . . 97
8.2.2 Counting secondary neutral interaction Λ background . . . 99

Chapter 9. H selection 101
9.1 General Cuts . . . 101
9.1.1 Event quality . . . 101
9.1.2 Fiducial volume . . . 102
9.1.3 Particle identification . . . 102
9.1.4 Kinematic . . . 105
9.2 Tight Cuts . . . 106
9.2.1 Fiducial volume . . . 106
9.2.2 Event quality . . . 110
9.2.3 Electron particle identification . . . 113
9.2.4 Kinematic . . . 114
9.3 Opening the Box . . . 115
9.4 Re-analysis without Particle Identification . . . 118
9.5 Other Background Estimates . . . 119
9.6 Background from Secondary Neutral Interactions in Gas . . . 123

Chapter 10. Normalization 124
10.1 Counting Target Lambdas . . . 124
10.2 Acceptance . . . 125
10.2.1 Production . . . 127
10.2.2 Numerical results . . . 134

10.3 H Acceptance 137
10.4 Single Event Sensitivity 140
10.5 Estimated Λ Production 142

Chapter 11. Results 144
11.1 Summary 144
11.2 Differential Production Cross Section Measurement 148
11.3 Total Production Cross Section Estimate 150

Chapter 12. Conclusion 152

Appendix A. Cut Summaries 156

Appendix B. Acceptance 161

Appendix C. BNL E888 Collaboration 168

References 169

Vita 178

List of Tables

3.1 Čerenkov threshold momentum for He-N_2 and Freon gas mixtures 46
3.2 Properties of Schott F2 lead glass 48

4.1 Level 1 physics trigger definitions 58

7.1 Total event summary 84

10.1 Kinematic variables of E888 and other Λ production experiments 128
10.2 Coefficients of fits to Λ production spectra 129
10.3 Mass and lifetime of Donoghue Hs 141
10.4 H single event sensitivity 142
10.5 Comparison of E888 results using the Beretvas, Abe, and Blobel lambda fits. 143

11.1 Summary of signal event characteristics 146
11.2 H production cross section limit (90% C.L.) 149
11.3 H production cross section limit, relative to the Λ production cross section 149

A.1 Summary of initial cuts applied to physics data 157
A.2 Summary of cuts applied to the high-$\not{p}_T$ H-decay data 158
A.3 Summary of cuts applied to the low-θ_C^2 normalization data . . . 159
A.4 Summary of cuts applied to the minimum bias data 160

B.1 Production-independent acceptance of E888 detector 162
B.2 Production-independent acceptance of E888 detector, cont. . . . 163
B.3 Production-independent acceptance of E888 detector, cont. . . . 164
B.4 Production-independent acceptance of E888 detector, cont. . . . 165

List of Figures

1.1 Theoretical predictions of the H mass versus year 8
1.2 Lifetime versus mass of the H 11

3.1 Broken wires from one of the vandalized drift chambers 30
3.2 The E888 detector and beamline. 34
3.3 Side view of the upstream beamline 37
3.4 Plan view of the downstream beamline 38
3.5 TSC vertical slat arrangement 40
3.6 Plan view of E791 spectrometer 42
3.7 Drift chamber cell structure 44
3.8 Čerenkov counter schematic diagram 47
3.9 Lead-glass calorimeter schematic diagram 50

4.1 Level 1 trigger schematic 56

6.1 Offline analysis flowchart 71
6.2 An idealized track in a drift chamber 76

7.1 Flowchart of events through Pass1 83

8.1 $\not{p}_T$ signature of Monte Carlo Hs 88
8.2 Monte Carlo $K_{\ell 3}$ decays reconstructed as $p\pi$ 90
8.3 π and μ momenta from $K_{\mu 3}$s which mimic Λs 92
8.4 π and e momenta from K_{e3}s which mimic Λs 92
8.5 Monte Carlo $K_{\mu 3}$s reconstructed as $\pi\pi$ 93
8.6 Schematic diagram of target and decay volume, showing definitions of collinearity (θ_C), p_T, d/p, and z_s 94
8.7 N_τ versus $\not{p}_T$ for Monte Carlo Hs 95
8.8 N_τ versus $\not{p}_T$ for Monte Carlo $K_{\ell 3}$s 96
8.9 Secondary neutral interaction background estimation 100

9.1 E_c/E_T versus E/p for MB events 104
9.2 Secondary Λ hot spots 107
9.3 x versus y snapshots of the projection of Λ momentum vectors . 108
9.4 Collimators and decay volumes of E888 detector as mapped by Λs 109
9.5 Distribution of signal events versus z_s and N_τ 110
9.6 QT vertex χ^2 of the target Λ sample 111
9.7 QT x- and y-view track χ^2s of the target Λ sample 111
9.8 Number of hits used by the fitter to fit the track in the x-view . 112
9.9 Electron rejection inefficiencies of Čerenkov counter and lead-glass calorimeter versus momentum. 115
9.10 The signal region before opening the box 116
9.11 The final N_τ versus $\not{p}_T$ distributions 117
9.12 Freon data re-analyzed without the left-side Čerenkov veto . . . 120

10.1 Normalization Λ θ_C^2 versus mass 125
10.2 Normalization Λ mass and collinearity distributions 126
10.3 Comparison of Abe and Beretvas Λ production momentum spectra 131
10.4 Comparison of Blobel and Beretvas Λ production momentum spectra to Abe data 133
10.5 Comparison of the invariant cross sections of the Beretvas, Abe, and Blobel fits 134
10.6 Comparison of observed data to the fits of Beretvas, Abe, and Blobel Λ momentum spectra 135
10.7 z vertex and number of lifetimes traveled of target Λs 136
10.8 Momentum and Feynman x of target Λs 136
10.9 Left and right track momentum of target Λs 137
10.10 Sample Monte Carlo H acceptance calculation 139
10.11 H production momentum spectra used to calculate acceptance . 140

11.1 Comparison of $m_{\pi\pi}$ versus $\not{p}_T$ of signal sample and MB $K_{\mu 3}$s . . 147
11.2 Comparison of calorimeter response of signal candidates and minimum bias K_{e3}s 147
11.3 90% C.L. H production cross section in terms of the Λ production cross section 150

B.1 Production-independent acceptance of E888 detector 166

Chapter 1

H Theory

Lepidus: *What manner o' thing is your crocodile?*
Antony: *It is shaped, sir, like itself,*
and it is as broad as it hath breadth;
it is just so high as it is,
and moves with its own organs;
it lives by that which nourisheth it;
and the elements once out of it, it transmigrates.
Lepidus: *What colour is it of?*
Antony: *Of its own colour too.*
Lepidus: *'Tis a strange serpent.*
Antony: *'Tis so; and the tears of it are wet.*
–William Shakespeare, Antony and Cleopatra

The theory of quantum chromodynamics (QCD) imposes no limitation *per se* on the number of quarks composing hadrons other than that they be color singlet states. Only qqq ($\bar{q}\bar{q}\bar{q}$) and $q\bar{q}$ states have been observed experimentally, though in theory, color singlet states can be composed of four, five, six (and larger) quark combinations. In 1977, Jaffe proposed that a six-quark totally symmetric spin zero combination *uuddss* might be stable due to the strong color-magnetic binding lent by the strange quark flavor [1]. The mass of this H (*Hexaquark*) state might then be less than twice the Λ hyperon (uds) mass and would be stable against strong decays. The H would decay weakly to $H \rightarrow \Lambda n$, $H \rightarrow \Sigma^0 n$, and $H \rightarrow \Sigma^- p$, depending on the H mass (m_H).

Theoretical estimates of m_H vary depending on the phenomenological model used, from 1.2 to 2.8 GeV/c^2, though the existence of the deuteron defines the lower mass limit, and a stable bound state cannot exist above $2m_\Lambda$. The lifetime and branching ratio of the H depends on its mass. Donoghue *et al.* calculated the H lifetime to be 10^{-9} s near the $2m_\Lambda$ threshold to over 10^7 s near the deuteron threshold [2]. These relatively long lifetimes allow the possibility that the H might be found in a neutral hadron beam.

If m_H were near the $2m_\Lambda$ threshold, the H would resemble the deuteron, being a lightly bound state of two nuclei. If the binding energy were larger, the H would become something else entirely, a highly symmetric six-quark state, a *dibaryon*, a new thing in itself.

It is not entirely surprising that the mass of a doubly-strange six-quark object might be less than the sum of two three-quark objects having the same flavor content because of color-magnetic hyperfine splitting. This is analogous to the electrodynamic hyperfine splitting observed in the hydrogen atom, but the effect is much more pronounced due to the relative magnitude of the strong force. The same phenomenon can be observed in the known hadron spectrum; *e.g.*, the $^1S_0$ particles π, K, and η are hundreds of MeV/c^2 lighter than their $^3S_1$ counterparts ρ, K^*, and ϕ, with identical quark content.

Despite several experimental searches, unambiguous proof of the existence of the H has not yet been found, and given the state of the theory of QCD interactions, no decisive proof of its non-existence can yet be made, either on *a priori* theoretical grounds or by ruling it out on the basis of prior searches. Without some theoretical limitation, it is difficult to confine the boundaries of the search such that the H can be ruled out decisively by experiment. So we

search for it in the phase space available to our experiments. If we were to find it, theories of quark hadrons would be forced to include it, and QCD (and its many models) would have another state to confine its boundaries; if we do not, it is still possible that it might exist in some dusty corner not yet explored. Aside from being interesting in its own right, the existence of the H dibaryon has somewhat fantastic implications – strange matter in neutron stars, and a source of free energy are just two possibilities.

This missive documents one such search. Before the dry description of the experiment begins, I will attempt to provide a flavor of the reasons why otherwise reasonable people think that such a strange serpent might exist, and in what strange countries they have searched.

1.1 Phenomenological Models

Due to the asymptotic nature of the strong interaction, QCD describes high energy interactions well, but the low-energy calculations necessary to describe hadronic states are so far intractable. Since it is very difficult to make low energy predictions using QCD (not even confinement of known hadrons has been theoretically demonstrated as of this writing, though progress is being made), many simplified models of the strong interaction of quarks in hadrons have been developed. These models usually have a few free parameters which are determined by modeling known hadrons and adjusting the parameters to arrive at the measured characteristics (mass, spin, etc.). Using these models, the properties of the H can then be predicted. A few of the more popular models and their predictions for the H mass are discussed below. Figure 1.1 shows predictions of H mass versus the year the prediction was made, and the

model used.

1.1.1 Bag model

The bag model has had some success in describing the known hadron mass spectrum. In it, quarks are confined by definition. Hadrons in this model are bags of colored quarks interacting with massless colored gluons. Only color singlet states are possible. The bag is a sphere of radius R and pressure B, where all the quarks exist in the $1s$ ground state. Quarks interact by one gluon exchanges, proportional to $g\lambda_a^c\sigma_k$, where g is the gluon coupling constant, λ_a^c are the eight generators of color SU(3), and σ_k are the three generators of spin SU(2). There are no gluon self-interactions, so the model resembles QED. One can therefore speak of separate color-magnetic and color-electric interactions.

This model can reproduce the mass spectroscopy of known baryons and mesons by adjusting the few parameters available: the bag pressure, the quark-gluon coupling constant, the zero-point energy, and the strange quark mass. The number of quarks in the bag can be up to 18 (2 spin states, 3 color states, and 3 flavor states), so it is a relatively simple matter put in six quarks and, with the parameters derived from calculating the masses of known hadrons, calculate the expected mass of the dibaryon.

The mass of the hadron is $M = E_B + E_q + E_c + E_m$. E_B is the bag energy, E_q the mass and kinetic energies of the quarks, E_c the energy due to color-electric interaction, and E_m the energy of the color-magnetic interaction. The last is the term that provides the binding energy of the particle, and the

one we are interested in. In the Fermi-Breit approximation,

$$E_m = -\frac{\alpha}{R}\sum_{i,j} M_{ij}(R)(\lambda^c \cdot \sigma)_i(\lambda^c \cdot \sigma)_j \tag{1.1}$$

where α is the strong coupling constant, and $M_{ij}(R)$ measures the strength of the quark interaction. The sum of this last term over all the quarks in the bag gives

$$E_m \propto \frac{1}{4}N(N-10) + \frac{1}{3}J(J-1) + \frac{1}{2}f_c^2 + f_f^2 \tag{1.2}$$

where N is the number of quarks, J the spin, and $f_{c,f}^2$ the eigenvalue of the quadratic Casimir operators of $SU(3)_{color,\,flavor}$. Then the state having $J = f_c^2 = f_f^2 = 0$ – the color, spin, and flavor singlet – has the largest color-magnetic attraction [3]. Using this model, Jaffe calculated the mass of the H as 2.15 GeV/c^2 [1].

Improvements on the calculation, such as pionic cloud, center-of-mass quark motion, and other higher-order corrections alter the predicted mass (2.12-2.19 GeV/c^2 predicted) [4, 5, 6, 7]. Some of these modifications move the H mass above the $2m_\Lambda$ threshold, others below. The most recent predictions still find a bound H in this model. These changes are shown chronologically in Figure 1.1.

1.1.2 Lattice QCD

Since exact results are difficult to obtain with QCD, one solution is to use a computer simulation to model reality. Lattice QCD represents the differential equations describing quark interactions on a matrix of spatial points as difference equations, and calculates the field at each of these points. This requires that the resolution of the matrix be fine enough to model the quarks

($\sim$ 10 MeV/c^2) and also be much larger than the hadrons which it attempts to model ($\sim$ 1 GeV/c^2), so that the matrix is effectively infinite as far as the hadron is concerned. This means that lattice computations swiftly approach the practical maximum computing times even on supercomputers. Higher-order effects are often ignored in order to reduce the computation needed.

For these purposes, lattice QCD has not had success comparable to that of the bag model. It does not reproduce the mass spectroscopy of the hadrons very well. Rather than hadron masses, the ratios of M_π/M_ρ and M_N/M_ρ are used as figures of merit, and tend to be high by as much as a factor of two. Nonetheless, estimates of the dibaryon mass in lattice QCD have indicated a very deeply bound H of mass 1.88 GeV/c^2 [8], as well as a very unbound H.

1.1.3 Skyrmions

Skyrme noticed that an SU(2) × SU(2) representation of a chiral quark model could be formed with two parameters such that solutions of the Lagrangian had finite radius and energy. These solutions resembled solitons in the Sine-Gordon equation, and were dubbed *skyrmions*. As with solitons, there is a topological conserved charge, the winding number, which is associated with the conserved baryon number.

In the two-flavor representation of this model, there are no six-quark stable states, but Balachandran *et al.* expanded the model to include a third flavor, and found a spin-zero six-quark color singlet with winding number of two, which they identified with the H [9]. The mass predicted by this model was 2.21 GeV/c^2.

Using variations of this model, Thomas and Scoccola found the H

slightly bound (34 MeV/c^2), but their calculation didn't describe the deuteron well, and they surmised that with the higher-order corrections necessary to do so, the H becomes unbound [10]. A more recent calculation by Klebanov and Westerberg found the H bound by 90 MeV/c^2[11].

1.1.4 Other models

There are several other models of QCD interactions in which the mass of the H has been estimated, with no more concrete results than those discussed above. These include QCD sum rules (2.19 GeV/c^2) [12], instanton interactions (less than 10 MeV/c^2 of binding energy) [13], and color dielectric models (binding energy of 100 MeV/c^2) [14], as recently as 1995 [11]. The results of these calculations are also shown in Figure 1.1.

The basics of the bag, Skyrmion, QCD sum rule, and quark potential models are all discussed in Ref. [15].

The basic point to take from all these discussions is that in all models used to represent QCD, stable H dibaryons have been found using the parameters derived from modeling known hadrons. While some improvements designed to make the models more accurately reflect reality move the predicted m_H above the $2m_\Lambda$ limit of stability against strong decay, most still predict a bound H. This bias towards the side of existence makes the search for the H promising.

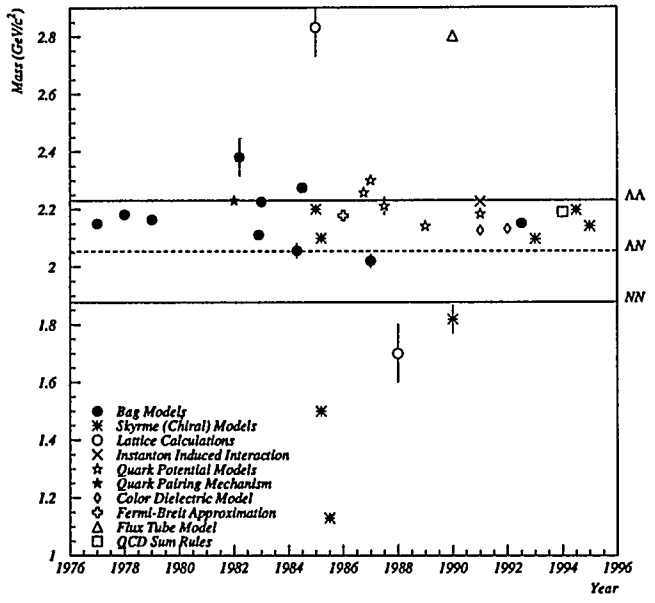

Figure 1.1: Theoretical predictions of the H mass versus year. Error bars are shown only if they were explicitly given in the calculation. If a range of masses was given, the central value was used. After Klein [46].

1.2 Lifetime of the H

The lifetime of the H is a crucial parameter in any experiment searching for it. In calculating the lifetime of these particles, the difficulty lies in finding a plausible way of moving from the artificial confinement of the models to the real two-baryon final state of the decay.

If the H mass is near $2m_\Lambda$, then the H is like the deuteron, a weakly bound two-baryon composite, and the decay properties of the lambda determine its decay properties. For more deeply bound Hs, where the object really is a six-quark bound state of highly similar wavefunctions, the decay properties of the particle are quite different.

If the wavefunction of the H is stated in the combined $SU(6)_{colorspin}$ representation, spin-zero states can only occur in three of the ground state SU(3)-flavor representations, only two of which are relevant here. One is the singlet state of the H. The other is the **27**-plet which contains the allowable baryon final states to which the H can decay. Based on these symmetry arguments, Donoghue, Golowich, and Holstein used well-understood dynamics of the weak decay and general properties of the bag model to calculate the lifetime of the H [2].

The $\Delta S = 1$ non-leptonic weak Hamiltonian is

$$H^{\Delta S=1} = \frac{G_F \cos\theta_C \sin\theta_C}{2\sqrt{2}} \sum_{i=1}^{6} c_i O_i \qquad (1.3)$$

where the c_i are numerical coefficients and the O_i are chiral four-quark operators. Only the c_3 and c_4 **27**-plet terms are relevant for this calculation, where the coefficients correspond to the $\Delta I = 1/2$ and $\Delta I = 3/2$ terms respectively. The fact that c_4 is larger than c_3 leads to the interesting result that the

$\Delta I = 1/2$ modes are suppressed with respect to $\Delta I = 3/2$, the only known situation in hadronic weak decays where this is true. The effect of this operator is to convert s quarks to d quarks, leaving a $uuddds$ bag state. This artificial bag state is related to the two-baryon final states by the P-matrix formalism of Jaffe and Low [16].

The calculation of the weak decay Hamiltonian was done in two parts. The first, the calculation of spin and color Clebsch-Gordan coefficients, is model independent. The second, the calculation of the spatial wave-function overlap, is model-dependent. Donoghue used the MIT bag model to calculate these functions. The lifetime of the H in this calculation is shown in Figure 1.2. This estimate is based only on the S-wave contributions; they were unable to calculate the P-wave contributions to the lifetime due to lack of experimental data on the P-matrix poles (though the two contributions should be roughly equivalent), so the lifetimes shown in these plots might be lower by as much as a factor of two.

This lifetime by this calculation is much longer than might be expected. Near the $2m_\Lambda$ threshold, the lifetime is ~ 2 ns, where one might expect it to be closer to one-half the Λ lifetime ($\tau_\Lambda = 0.26$ ns). If $m_H < m_\Sigma + m_n$, the decay will be very long-lived due to the suppression of $\Delta S = 2$ modes by the extra factor of G_F in the Hamiltonian. For Hs above the $\Delta S = 2$ threshold, though, the lifetimes are in the range that make the search for Hs in existing hadronic beams promising. For the remainder of this thesis, all calculations will assume the Donoghue mass, lifetime, and branching ratio relationships.

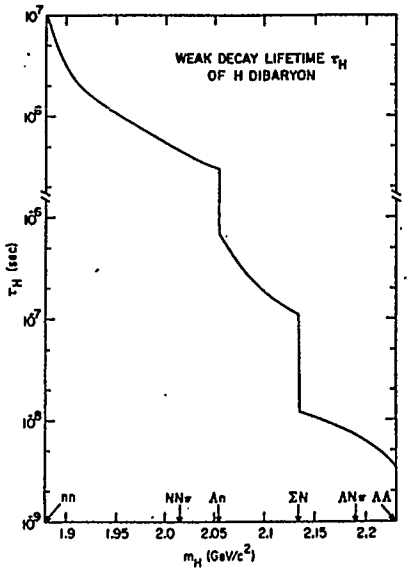

Figure 1.2: Lifetime versus mass of the H as calculated by Donoghue *et al.* [2].

1.3 H Production

Since we do not know the mass or lifetime of the H, it is difficult to predict the characteristics of production in a hadronic collision. It is difficult to make predictions about particle production in systems about which we know much more. Regge pole theory has had some success describing the production of hadrons at high energies and small angles, and 'fireball' thermodynamic models have been used to predict low energy heavy ion production. There are few published estimates of H production. Some of these efforts are described below.

Badalyan and Simonov [17] used the formalism of Jaffe and Low [16] and the constituent quark bag model to calculate the production cross section of the H at threshold production momenta. Their calculation predicts the experimentally measured ratio of $\sigma(pp \rightarrow \pi^+\pi^- d)/\sigma(pp \rightarrow \pi^+\pi^- pn)$ reasonably well. They found $\sigma_H \simeq 4 \times 10^{-3}\sigma_{\Lambda\Lambda}$. Using the results of an early H search [39] to estimate the $\Lambda\Lambda$ production cross section and obtain an upper limit, and using the limits of a double hypernuclei experiment to set a lower limit ([48]), they found $\sigma_H \simeq 0.8 - 2.0$ nb for $p + p$ at 2.2 GeV/c.

Cousins and Klein calculated the production cross section based on a coalescence model similar to those used successfully to estimate deuteron production. This model assumed that two Λs would coalesce into the more energetically favorable (if the H exists) dibaryon state if the Λs were produced within a certain distance of each other and had low enough relative momentum. The distance d and relative momentum p_0 are parameters of the model. The first Λ was assumed to be a leading particle, with quarks from the incident proton, and produced according the spectrum of Blobel (Section 10.2.1). The second Λ

was produced according to two methods. One assumed that the second Λ was centrally produced from new quarks created in the collision, and thus should be similar to $\overline{\Lambda}$ production, resulting in a central-like production momentum spectrum [18]. The other method assumed that the second Λ was also produced according to the Blobel spectrum [19]. Based on the latter model, Cousins and Klein estimated that the production cross section was greater than 100 μb/sr. This model used only the $\Lambda\Lambda$ part of the two-baryon basis state

$$\Psi_H = \frac{1}{\sqrt{8}}(\Lambda\Lambda + \Xi^0 n + n\Xi^0 + \Sigma^0\Sigma^0 + \Sigma^+\Sigma^- + \Sigma^-\Sigma^+ + \Xi^- p + p\Xi^-) \quad (1.4)$$

to calculate these quantities, but there are other factors involving the probability of the two Λs being in the proper relative spin states to form a spin-zero dibaryon which should roughly compensate for the missing terms.

Rotondo [20] used the $\Xi^0 n$ state in Equation 1.4 to calculate the production cross section at Fermilab energies. He argued that $\sigma_H = F_1 F_2 \sigma_{\Xi^0 n}$, and that because each of the four distinct two-baryon basis states should be approximately equally likely, $F_1 \sim 4$. The second factor takes into account the difference between the formation of a $\Xi^0 n$ nuclear state and an H dibaryon (the former would have a radius of 2 fm, similar to a deuteron; the latter 1 fm, similar to a baryon). Since coalescence becomes less likely the farther apart the particles are produced (as $[R_{composite}/R]^3$), the H is 1/8 as likely to coalesce as a $\Xi^0 n$ state. Thus the product $F_1 F_2$ is approximately one. Then using measurements of inclusive Ξ^0 production at Fermilab, and a 'penalty factor' for the coalescence of a neutron based on measurements of the ratio of deuteron production to protons and pions, Rotondo estimated that $\sigma_H \simeq 1.2$ μb at Fermilab energies.

Cole *et al.* [21] used the RQMD cascade model [22] to simulate $p + A$ interactions at 28.4 GeV/c (maximum BNL AGS energies). This model predicts the total H production cross section $\sigma_{tot} \approx 3 \times 10^{-5} \sigma_{inelastic}$. Taking $\sigma_{inelastic}$ as $\approx$ 500 mb [58], $\sigma_{tot} \approx 15$ μb. Maximum dibaryon formation was predicted to occur at rapidity $y \sim 1$, falling to zero by $y \sim 2$. E888 had a rapidity range of $0.9 < y < 1.5$, with peak at $y \sim 1.2$.

1.4 Other Multiquark States

If a six-quark stable state of matter were to be found, then one might reasonably ask whether $3 < N_q < 6$ or $N_q > 6$ stable states might exist, and what their physical and cosmological implications might be. Experiments searched for dimesons ($q\bar{q}q\bar{q}$) [24, 25, 26], pentaquarks ($q\bar{q}qqq$) [27, 28], and strangelets ($N_q > 6$) [29, 30], thus far without success. The dimeson and pentaquark states are theoretically less promising than the H though some models find slightly bound states or resonances. There is more theoretical support for strangelets, and experiments designed to search for these states at heavy-ion accelerators are in progress. The existence of $N_q \gg 6$ states, or *strange matter* arises in the study of early phases of the universe, dark and missing matter, and neutron stars [31, 32, 33, 34]. The H is a signpost to these multiquark states, since they are unlikely to be stable if the simpler and more symmetric six-quark state is not.

Strange Matter: $N_q \gg 6$

Witten [35] pointed out that a quark gas containing three flavors could have its pressure reduced by the addition of the third flavor versus a normal

two-flavor quark-matter gas for the same total number of quarks because the number of states available increases. The pressure of the gas could then be reduced by more than the energy difference added by the increased mass of the quark. While strange quarks do not necessarily stabilize nuclear matter because strange baryons are heavier than non-strange baryons, quark matter is a different story.

This effect can be illustrated using the bag model (the following argument is taken from Ref. [35]). Each quark flavor contributes a Fermi momentum of $p_F/4\pi^2$ to the quark gas. Let the Fermi momentum of the up quark be μ. Then to maintain charge neutrality, the chemical potential contributed by the down quarks must be $2^{1/3}\mu$. The total pressure is then $(1+2^{4/3})\mu^4/4\pi^2$. Ignoring the strange quark mass, the three flavors of quarks should exert the same pressure, with a common Fermi momentum of

$$\tilde{\mu} = \left[\frac{1}{3}(1+2^{4/3})\right]^{1/4}\mu\,. \tag{1.5}$$

The average quark kinetic energy is proportional to μ, so since the pressure is common to both two- and three-flavor cases, the kinetic energy of the latter case is smaller by

$$\frac{\tilde{\mu}}{(\frac{1}{3}\mu+\frac{2}{3}2^{1/3}\mu)} = \left[\frac{3}{(1+2^{4/3})}\right]^{3/4} \simeq 0.89\,. \tag{1.6}$$

Strange matter could then be bound by as much as 100 MeV/c^2 per baryon, neglecting the strange quark mass. Even with the strange quark mass being non-zero, strange matter might still be bound by 30-50 MeV/c^2 per baryon, leading to the conclusion that strange matter is more stable than normal up and down quark matter. It is not likely that ordinary matter would

spontaneously convert to strange matter, because of the improbability of the necessary number of down quarks simultaneously converting to strange quarks via the weak interaction. If strange matter were the lowest energy state of matter in the universe, there is a possibility that pockets might still exist in the universe, left over from the quark gas conditions following the Big Bang.

It is also possible that some neutron stars might be made of strange matter, since in that compressed environment, the weak decay of $ud \rightarrow us$ would be more probable. The radius and density of such a strange neutron star could, in principle, differ enough from the more usual type to be detected. It would be more dense and so spin faster, so one method of detecting them would be to search for pulsars rotating faster than a normal matter pulsar of the same mass. It may be that only the center of the neutron star reaches the density needed to undergo this conversion, in which case there would be a strange quark core, but the outer shell would be normal neutron star matter. This type of pulsar would resemble a normal pulsar in almost every way, and would be difficult to detect.

The most interesting property of strange matter, however, is that it could be a free source of energy [36]. Once strange matter exists, it creates an environment in which it is energetically favorable for quarks in normal matter to convert to strange quarks. This conversion would be exothermic, so if we had a lump of strange matter, we could shoot neutrons into it and get energy back. This sounds suspiciously like the stuff of bad science fiction movies (or good ones, for that matter), and one might reasonably wonder what keeps our strange nugget from gobbling up the earth. But normal nuclei (except iron) can also undergo exothermic nuclear reactions, though they do not except

under special circumstances. This is because under normal circumstances the nucleus is positively charged. Strange quark matter will have a positive charge on the surface (though *in toto* electrically neutral) for the same reason as a nucleus. The ratio of *u:d:s* quarks in strange matter would be about 2:3:1, so that $\mu_d - \mu_u \simeq 50$ MeV/c^2. To balance this chemical potential difference, there would be an equal electrostatic potential at the surface, enough to repel positively charged nuclei.

Having now explained why the H might exist, and some of its more interesting properties, it would be surprising if no one had yet searched for it. Let us consider some of the experimental research in this field.

Chapter 2

Other Searches

Say, from whence
You owe this strange intelligence? or why
Upon this blasted heath you stop our way
With such prophetic greeting?
–William Shakespeare, Macbeth

Strange matter, in all its forms, has been looked for in many regions, though in many experiments, as in this one, the search was subsidiary to some other goal. Lying as it does on the boundary between high-energy and nuclear physics, neither camp has made a full-bore attempt to find this decay. The H and strange matter have recently attracted a good deal of scientific and popular attention [31, 37], so this will change in the near future, as several groups have experiments in progress or on the drawing board designed to look for this particle and other strange matter.

It is difficult to search for a particle about which we know so little. Is the H a baryon, such as the Λ, or is it a loosely bound state similar to the deuteron? Not knowing its mass or lifetime, it is difficult to construct experiments which are optimized to find it. This leads to another difficulty, that of trying to compare results from the various experimental searches. Since each is sensitive to a different region of phase space, it is difficult to compare

the results. Nonetheless, we will examine some of these experiments and try to summarize their results.

2.1 Past Searches

2.1.1 Collision experiments

Several experiments have used the fixed target collisions to search for the H. There are two basic ways to go about this. One is to use a proton beam, which has the advantage of high luminosity and having the proper baryon number to produce the H. The disadvantage of this approach is that the rate of production of two strange quarks in a non-strange beam having the proper spin state to form the H may be very small. However, if it is possible, it will occur eventually given enough collisions. An alternative is to use a beam with an initial degree of strangeness. These beams are typically less luminous, though.

Gustafson *et al.* [38] (1976) used the 300 GeV/c beam at Fermilab to search for heavy neutral integrally charged quarks and stable charmed mesons, using a total absorption calorimeter and time-of-flight (TOF) measurements to determine the mass. Gustafson saw 14 events in the 2.0-3.0 GeV/c^2 mass range, but these events were consistent with their background from neutrons. They were able to set a 90% confidence level (C.L.) limit on $Ed^3\sigma/d^3p$ of 1.1×10^{-32} cm^2/GeV^2 per nucleon, corresponding to $\sigma_H < 65$ nb/nucleon. This experiment was, however, limited to small regions in Feynman x_F of $-0.05 < x_F < 0.09$ and transverse momentum of $0.13 < p_T < 0.32$ GeV/c, and lifetimes greater than 100 ns.

Carroll *et al.* [39] (1978) used a method suggested by Jaffe in his original

paper to search for the H. Jaffe had suggested that $p + p \rightarrow H + K^+ + K^+$, and that by observing the two kaons, the missing mass of the H could be reconstructed. This experiment used a double-armed spectrometer and several planes of Čerenkov counters optimized to discriminate kaons from protons and pions. As with the previous experiment, this detector was also designed for charmed particle searches, but was modified to improve its kaon discrimination in the appropriate momentum range. The range of incident proton momentum available, 5.1-5.9 GeV/c, made them sensitive to m_H of 2.0-2.5 GeV/c^2. They observed several events with $m_X < m_{\Lambda\Lambda}$, but these were all consistent with the expected background. Their 90% C.L. upper limit on H production cross section, based on the assumption of a flat production phase space, was $\sigma_H < 130$ nb for $2.0 < m_H < 2.1$ GeV/c^2, and $\sigma_H < 40$ nb for $2.1 < m_H < 2.23$ GeV/c^2.

Shahbazian *et al.* [40] (1988), in an experiment at Dubna, reported one H event in a bubble chamber experiment. A 10 GeV/c proton beam was fired into the bubble chamber and the subsequent decay of the H looked for. They saw one event which they interpreted as $p + d \rightarrow H + p + K^+ + K^0$, followed by $H \rightarrow \Sigma^- + p$, and also found a subsequent topology consistent with $H + p \rightarrow \Lambda\Lambda + p$. Neither the K^0 nor the Σ^- was observed to decay, though there was only an 11% chance of the Σ^- escaping their detector undecayed. They found the mass of this H candidate to be 2.173 GeV/c^2. They also saw a resonance in their 57 $\Lambda\Lambda$ events at 2.365 GeV/c^2, with a width of 45 MeV/c^2.

Shahbazian *et al.* [41] (1992) later claimed to see two heavy neutral Hs of mass 2408.9 ± 11.2 and 2384.9 ± 31.0 MeV/c^2 and two charged dibaryons (H^+) of mass 2375.8 ± 9.3 and 2409 ± 13.0 MeV/c^2, all above the $2m_\Lambda$ strong decay threshold. Based on these last four events, they quote a total production

cross section of 60 nb/nucleon.

Alekseev *et al.* [42] (1990) used a neutral beam on a carbon target and measured the momenta of the charged decay products downstream. They rejected charged particles out of the target with an veto counter at the target. They found two events which they interpreted as $H \rightarrow \Lambda + p + \pi^-$ with a mass of 2.200 GeV/c^2. These events are questionable because the reconstructed decay vertices were inside the target or veto counter, where the backgrounds were large. They also observed 67 $\Lambda\Lambda$ events, but found no resonance above $2m_\Lambda$. They stated the cross section in terms of the branching ratio of this decay and the probability of the H leaving the carbon target as $\sigma_H \mathrm{Br}(H \rightarrow \Lambda p\pi^-)P_H = 18$ nb.

Aoki *et al.* [43] (1990) used the 1.66 GeV/c K^- beam at KEK to strike an emulsion target and looked for the reaction $K^- + p \rightarrow H + K^+$. This experiment set a 90% C.L. upper limit of 0.2-0.6% that of quasifree Ξ^- production in the mass range 1.09-2.16 GeV/c^2, and based on a theoretical calculation [23], a differential cross section of 500 nb/sr ($m_H = 2.1$ GeV/c^2).

The RISK collaboration at Serpukhov [44] (1986) used a 40 GeV/c π beam with several targets to study the reaction $\pi + N \rightarrow H \rightarrow \Sigma^- p$. The decay products were tracked by a streamer chamber within a magnet, allowing them to identify the $\Sigma^- \rightarrow \pi^- n$ by the kink in the track due to the unseen neutron, and measure its momentum. Particles were identified by a series of four Čerenkov counters. They found five events with a kink in the negative track, out of 1720 reconstructed V's. These events did not have a consistent invariant mass corresponding to an H, and were probably Λ's, K_S, or secondary interactions in the chamber walls. Based on this, they found the H production

cross section between 160-970 μb, depending on the target.

The other half of E888, the *dissociation* search [45] (1992), used a diffractive dissociator placed in the neutral beam 21 m downstream of the target to search for the process $H + A \rightarrow \Lambda\Lambda + A$. The dissociator was a stack of scintillators instrumented with phototubes to measure the recoil energy of the nucleus in this reaction. The last scintillator was used as a charged particle veto. The experimental apparatus was much the same as the one described in this dissertation (the *decay* search); the dissociation search is described in detail in Ref. [46]. This experiment was sensitive to more deeply bound Hs than the decay search, due to the distance of the dissociator from the target. It placed a 90% C.L. on the production cross section $d\sigma/d\Omega < 1$ mb/sr for Hs with a lifetime greater than 100 ns. The dissociation search also searched for very short-lived Hs produced by interactions of the neutral beam (primarily neutrons and kaons) in the dissociator. In addition to a large number of ΛK_S diffractive dissociations, this experiment observed 40 $\Lambda\Lambda$ events, but saw no resonance above the $2m_\Lambda$ threshold. Together, the two halves of this experiment explored a large range of mass, lifetime, and momentum phase space, and two very different methods of H decay.

2.1.2 Hypernuclei H experiments

An obvious place to search for a multi-quark object is in the quark-rich environment of the nucleus. Many experiments have observed hypernuclei decays, where one of the nucleons is replaced by a Λ, which then decays weakly. If double hypernuclei (two Λs replacing nucleons) were observed, this would cast doubt on the existence of the H. If it could be shown that a nuclear $\Lambda\Lambda$ state

existed in a light nucleus but did not coalescence into an H, this would imply that the H could not exist as a bound state. The coalescence of two Λs into an H would take place on a time scale set by the strong interaction ($\mathcal{O}(10^{-20})$ s), and if $m_H < 2m_\Lambda$, would seem likely to occur within the confines of a light nuclei, while the decay occurs weakly ($\mathcal{O}(10^{-9})$ s). Three double hypernuclei candidates have been observed in three different experiments over the last 32 years.

Both Danysz (1963) [47] and Prowse (1966) [48] detected a double pion decay in emulsion, which they claimed to be consistent with the decay of the two Λs from a double hypernuclei. Both experiments relied on Ξ^- capture by a carbon nuclei in the emulsion to form the double hypernuclei. Dalitz [52] reviewed both these events in 1989, and found the emulsion of Danysz not inconsistent with the original interpretation. Dalitz was unable to verify the Prowse data, as the original emulsion was lost, and Prowse had died in the interim. One troubling aspect of both these experiments is the improbability of a Ξ^- stopping in their emulsions. Dalitz estimated that, at most, only one or two Ξ^-s should have been stopped in their emulsions. Also, the estimated binding energy of the two events does not agree with each other.

The third, more recent hypernuclei candidate was reported by Aoki *et al.* [49, 50] (1991). If this candidate is accepted, the mass of the H should it exist, is unlikely to be less than 2.202 GeV/c^2 ($m_{\Lambda\Lambda} - (B_{\Lambda\Lambda} + \Delta B_{\Lambda\Lambda}$, where $B_{\Lambda\Lambda}$ is the binding energy of the two Λs to the nucleus and $\Delta B_{\Lambda\Lambda}$ the binding energy of the two Λs to each other). However, Dover *et al.* point out that Aoki's interpretation of the decay chain of of this experiment leads to a repulsive $\Lambda\Lambda$ interaction, which disagrees with most models of the nuclear interaction [51].

In any case, the paucity of events observed by this experiment casts doubt on the events of Danysz and Prowse, as the production rate observed by this latest experiment was far too small for it to be likely that an event was produced in either of the two earlier experiments.

Klein points out that all three of these events are consistent with the weak decay of an H formed in the nucleus [46].

2.1.3 Double weak decays of nuclei

The lower limit on the mass of the H is set by the existence of the deuteron. If the mass of the H were much less than that of the deuteron, most deuterons in the universe would have decayed into Hs, which apparently has not happened since deuterons are relatively common. Ejiri *et al.* [53] (1989) extended this argument further. They examined several double weak decays of nuclei and by estimating the decay rates of the H and comparing to known decay rates limited the mass of the H to $m_H > 1.875$ GeV/c^2 ($m_d = 1.8756$ GeV/c^2).

To summarize the above descriptions, several experiments have claimed to see single H events, though all can be questioned in some aspect, and none agree with any of the others. The most believable one, that of the double hypernuclei decay found by Aoki, does not rule out the existence of a lightly-bound H, and is yet unverified by any other experiment.

These experiments are discussed in more detail in Klein [46].

2.2 Current Searches

There are several experiments currently analyzing data, in progress, or scheduled to take data in the near future. I describe some of these below.

2.2.1 Collision experiments

BNL E813 (1991-5) at BNL uses a 2 GeV/c K^- beam incident on a liquid ^{2}He target to produce $\Xi^- + K^+$. A magnetic spectrometer and TOF apparatus identify the K^+ and measure its momentum. Events with the appropriate missing mass are tagged as Ξ^-. These events pass into a tungsten moderator, then a liquid deuterium target. The slowed Ξ^- interacts with the deuteron, then decays to $H + n$. The mono-energetic neutron from this decay is detected by another TOF array. The experiment is sensitive to Hs in the mass range $2m_\Lambda - 80 < m_H < 2m_\Lambda + 20$ MeV/c^2.

BNL E836 (1994-5) is an upgrade to E813. The two component target above is replaced by a ^{3}He target. The decay sought is $K^- + {}^3\mathrm{He} \rightarrow K^+ + H + n$. Due to the change in target, this experiment is sensitive to lower masses than E813.

BNL E885 (1995) also uses the E836 kaon beam and spectrometer to search for double hypernuclei. The targets are CH_2 and ^{6}Li so the reaction chain is $K^- + p \rightarrow \Xi^- + K^+ \rightarrow \Xi^- + {}^6\mathrm{Li} \rightarrow {}^{6}_{\Lambda\Lambda}\mathrm{Li} + n$ where the mono-energetic neutron is again detected by time-of-flight detectors. Background is rejected by detecting the $\Lambda \rightarrow p\pi^-$ decays with scintillators on either side of the beam. This experiment may also search for H decays via the mechanism of $K^- + {}^{12}\mathrm{C} \rightarrow K^+ + H + X$ (similar to that of the Aoki emulsion experiment), and reconstructing the missing mass.

KEK-248 searches for the H in the same manner as Carroll, above, in the 12 GeV/c beam at KEK. This experiment has been running since 1991.

2.2.2 Heavy ion experiments

BNL E810 [54] (1991) used a 14.6A GeV/cheavy ion beam to study the reaction Si + Pb $\rightarrow$ H $\rightarrow$ $\Sigma^- + p$. Charged tracks were recorded using three time projection chambers in a magnetic field. Out of 5000 events, this experiment has found 33 candidates with an estimated background of 11, and fit these 20 events to an H mass of 2.18 GeV/c^{2}and a $c\tau$ of 10 cm. The FWHM of this mass distribution was 52 MeV/c^2. This experiment is still running and should increase the number of events by a factor of five.

BNL E878 [30] (1995) used a 10.8A GeV/c Au + Au target to search for strangelets. This experiment used a two-segment focusing spectrometer and four TOF measurements to measure the momentum and charge of particles. Particle identification consisted of two gas and two aerogel Čerenkov counters. Strangelets would have mass-to-charge ratios outside the range expected for normal matter. This experiment found no evidence for new particles with lifetimes greater than 100 ns.

BNL E896 will use an 11.7×A GeV/c Au beam to search for shortlived Hs via the $H \rightarrow \Sigma^- p$ decay. The detector will consist of a dipole magnet to sweep charged particles, a low mass "distributed" drift chamber with low efficiency for neutrons and gammas, and a small array of silicon drift detectors. The experiment will trigger on neutral Vs in the drift chamber, and will be sensitive to Hs with lifetimes greater $c\tau > 4$ cm.

Some of these experiments are discussed in more detail in [55, 56]. Other

experiments are planned or in progress at CERN and KEK.

Chapter 3

Experimental Apparatus

Yet beauty, though injurious, hath strange power,
After offence returning, to regain
Love once possess'd.
–John Milton, Paradise Lost

3.1 History

The history of the E888 detector is worth exploring briefly, if only to minimize confusion between the different experiments using the same apparatus. This detector started its life as a rare kaon decay experiment, E791. It first took data in 1987, and though the spectrometer was incomplete, the collaboration was able to publish data [57], and ran for four years with only minor changes, reaching the lowest sensitivity of any experiment in the world for the rare decays $K_L \to \mu^{\pm}e^{\mp}$, $K_L \to e^+e^-$, and $K_L \to \mu^+\mu^-$. E791 at the time had the most intense neutral beam in the world, and set branching ratio limits for $K_L \to \mu^{\pm}e^{\mp}$ and $K_L \to e^+e^-$ on the order of 10^{-11} [58, 59, 60], and observed the largest number of $K_L \to \mu^+\mu^-$ seen up to that time [61]. Despite these successes, some theories predict $K_L \to \mu^{\pm}e^{\mp}$ at a lower limit than that reached by E791, and the Standard Model unitarity limit for $K_L \to e^+e^-$ was not reached. Detector technology having improved sufficiently to make

an upgrade of E791 feasible, E871 was conceived. With many of the same collaborators, E871 began test runs in the E791 experimental area in 1991.

One of the main features of the upgrade was an integral beamstop within one of the spectrometer magnets. One of the tasks during the test run was to build this beamstop, study materials and configurations, and their effects on the surrounding detectors. The 1992 proton run (a short one, due to DOE budget constraints) was planned as a further test run with the E871 electronics in place. E888 was approved as a two-week parasitic experiment during this short run. Unfortunately, during the break between the 1991-2 runs, thieves entered the deserted B5 experimental area and stole much of the copper used in the beamstop. In the course of this theft, they committed the larger, if unintentional, crime of destroying four of the drift chambers used by E791. This was a devastating setback for the planned E888 physics run. After a crash course in drift chamber construction, Josh Klein and I went to BNL, where we spent a cold, snowy February in the unheated experimental area, removing and replacing 800 very small broken wires. Figure 3.1 shows a photograph of one of the chambers after the damage.

Despite an FBI investigation, the thieves were never identified nor caught, and the copper was not recovered.

So the experimental apparatus used by E888 was that of E791, with the E871 collaborators allowing us to run parasitically during their engineering run. From here on, I will refer to the experimental apparatus as E888, having acknowledged that, for the decay phase of this search, it was identical to that of E791, and has been described in many places [62, 63, 64, 65]. The E888 collaboration was almost identical to the E791 rare kaon decay experi-

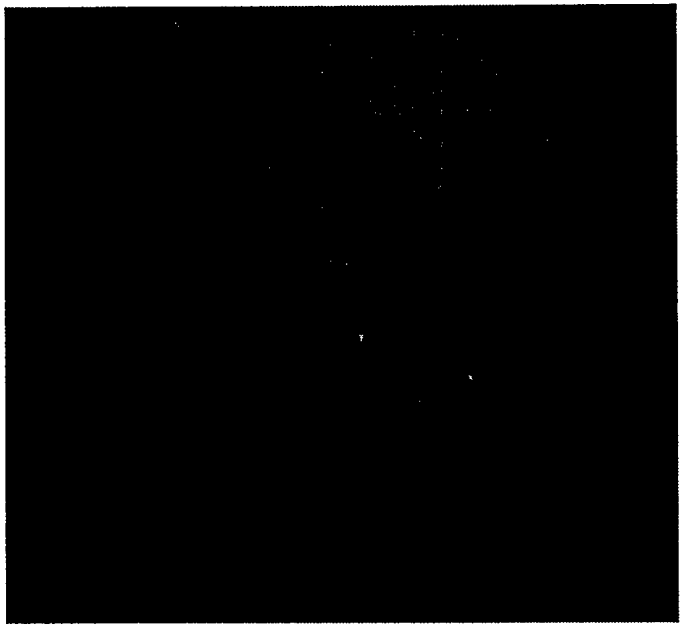

Figure 3.1: Broken wires from one of the vandalized drift chambers. The visible wires are the 4.3 mil (109 μm) field wires; the 1 mil (25.4 μm) sense wires are invisible in this picture, and indeed were invisible except in a dark room under a bright light.

mental group, with the addition of the Princeton and Brookhaven collaborators (Appendix C).

3.1.1 Experimental overview

A neutral beam was produced using the AGS 24 GeV/c proton beam, and that neutral beam was collimated into a series of vacuum chambers. The experiment was sensitive only to particles which decay in the vacuum regions. A spectrometer consisting of two-magnets and five pairs (left and right) of drift chambers measured the decay products' momenta: two drift chambers upstream of the first magnet, one between the two magnets, and two downstream of the second magnet. The magnets' fields were arranged to deliver transverse momentum impulses of $\sim$ 300 GeV/c of opposite sign, thus preserving the opening angle of the decay and providing a large $\int \mathbf{B} \cdot d\mathbf{l}$. Two pairs of trigger scintillator hodoscopes, a pair on each end of the Čerenkov counters, provided the primary event trigger. The Čerenkov counters were used to discriminate protons and electrons from pions and muons. A lead-glass electromagnetic calorimeter measured the energy of electrons, and aided discrimination of pions and electrons. A 0.91 m iron block, the hadron filter, ideally absorbed all remaining particles except muons. A scintillator hodoscope located the x-y positions of the remaining muons, which ranged out in the absorber/drift tube rangefinder, providing additional discrimination between hadrons and muons. The *Level 0* trigger was formed by signals from the trigger scintillators indicating a charged track in each arm. Signals from the drift chambers and particle identification from the Čerenkov counters and the muon hodoscope were added to form the *Level 1* trigger. A top view of the experiment is shown in Figure 3.2.

Each of these detectors will be considered in detail in this chapter.

3.2 Two phases: He-N_2 and Freon

Now, by two-headed Janus,
Nature hath fram'd strange fellows in her time.
–William Shakespeare, The Merchant of Venice

If the H has mass greater than ~ 2.06 GeV/c^2, its lifetime should be long enough for it to have a significant signal in the region for which E888 had acceptance. The decay search of E888 took data for two weeks looking for the inclusive reaction $p + \mathrm{Cu} \rightarrow H + X$, sensitive to an H mass greater than 2.06 GeV/c^2 and lifetimes longer than a few nanoseconds. The observable decays were $H \rightarrow \Lambda n$ and $H \rightarrow \Sigma^0 n$ ($\Sigma^0 \rightarrow \Lambda\gamma$), so that the final observable decay was a $\Lambda \rightarrow p\pi^-$ with missing transverse momentum ($\not{p}_T$).

The decay search took place in two distinct phases. In the first, both Čerenkov counters were filled with a He-N_2 gas mixture. This was the normal configuration for this detector and was well-understood from previous analysis. By taking a portion of the data in this configuration, we hoped to have a sample of data with no suprises from unconsidered side-effects. During the second half of the decay run, the left Čerenkov counter was filled with Freon 12, which has a higher index of refraction. The Čerenkov threshold momentum of a particle traversing a material is

$$p_{\mathrm{thr}} = \frac{m}{\sqrt{n^2 - 1}} \tag{3.1}$$

where m is the mass of the particle, and n is the index of refraction of the Čerenkov material. In the He-N_2 mixture, only electrons and very high momentum pions ($p_{\mathrm{thr}} = 6.8$ GeV/c) and muons ($p_{\mathrm{thr}} = 8.3$ GeV/c) would trigger the counters. The threshold momentum of pions in the Freon is lower ($p_{\mathrm{thr}} = 3$ GeV/c), so that most pions from background decays were above threshold,

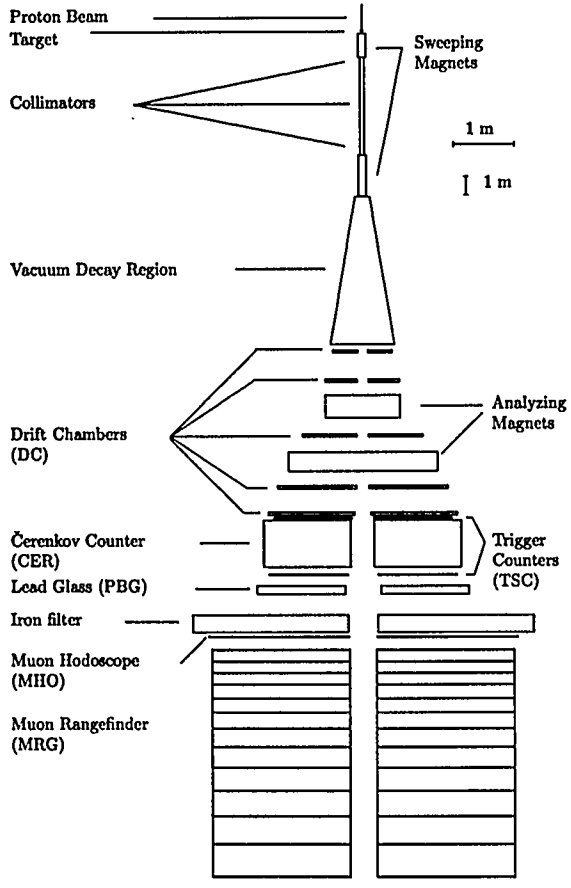

Figure 3.2: The E888 detector and beamline.

and allowed the discrimination of pions from protons ($p_{\rm thr} = 20$ GeV/c) on the left side.

The advantage of using Freon in only the left detector becomes apparent when one considers the specifics of the Λ decay in this detector. Due to the lack of excess kinetic energy in the decay $\Lambda \rightarrow p\pi^-$ ($m_\Lambda - (m_p + m_\pi) \simeq 40$ MeV/c^2) and the greatly different masses of the daughters, the proton would be hard and the pion soft ($p_\parallel = \gamma(p^*_\parallel + \beta E^*) \simeq \gamma m$). The detector was left-right symmetric, and the Λ decay was rotationally symmetric, but these symmetries were broken by the first magnet and the fact that the detector accepted decays only within a finite area. Then $\Lambda \rightarrow p\pi^-$ decays which traversed the entire detector were primarily $p_L\pi^-_R$, because the soft pions from $p_R\pi^-_L$ decays were bent inward by the first magnet and crossed the beamline, and could not be reconstructed by pattern recognition. This asymmetry is why the lower-threshold Freon gas was used in the left-side Čerenkov counter, and is an important consideration in studying the backgrounds which mimic Λs. The two phases of the decay search will be referred to as *He-N_2* and *Freon*.

In the remainder of this thesis, I take $c = 1$, so that all momenta and masses are in GeV. The units used throughout the analysis were SI, but much of the experimental apparatus was specified and built in English units. To avoid a foolish consistency, I have stated dimensions in the most appropriate units, whether SI or English.

3.3 Target and Beam

The neutral beam of E888 was produced by directing a portion of the 24 GeV AGS proton "slow extracted beam" onto a copper target 1/8″ by 1/8″ by 8″ long (1.38 hadronic interaction lengths). The target was mounted at an angle of 48 mrad (2.75°) to the horizontal, and the proton beam pitched down into the long dimension of the target. The target was centered 12 cm upstream of the origin of the E791/B5 coordinate system (nominal target zero, or NTZ)[1].

The resulting beam passed through a series of 17 lead foils 5 mm thick and 5 cm apart to convert photons to electrons, giving gamma attenuation greater than 10^6. A pitching magnet (B5P4) swept charged particles out of the beam, and the particles produced at an angle of 48 mr to the beam direction were collimated by a series of metal apertures to a beam profile of 65 μsr with a 1:10 aspect ratio (horizontal to vertical). A final pitching magnet (B5P5) swept any remaining charged particles out of the beam, resulting in a relatively pure neutral beam. The neutral beam passed into two high-vacuum decay volumes, a small one from 9.79 m to 11.07 m, and a larger one from 11.73 m to 17.75 m. The vacuum inside these two chambers was maintained at 3×10^{-4} torr. The beamline from the target to the first decay tank is shown in Figure 3.3. The beamline from the small decay tank to the vacuum window is shown in Figure 3.4. The window was made of 130 μm Mylar and 17 mil Kevlar 29 (49.6 mg/cm^2). The center of this window was 2.39 cm above the nominal beam center ($x = y = 0$).

The length of the spill varied between 0.2 and 0.8 s, with a cycle time of three seconds. E888 ran at low intensities for the first part of the run, less than 10^{12} protons per spill (10^{12} protons $\equiv$ 1 Tp), increasing to 2 Tp at times in the

[1]The coordinate system originated at NTZ (for historical reasons), and the center of the neutral beam formed the z axis. z increased from upstream to downstream and positive y was up, so positive x increased from beam center to left.

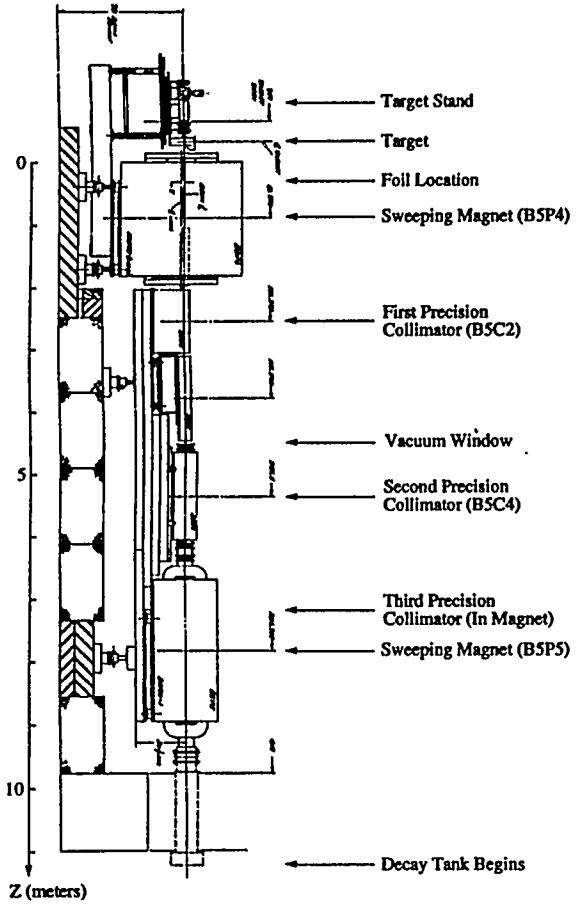

Figure 3.3: Side view of the upstream beamline, showing the target, sweeping magnets, collimators, and first vacuum tank.

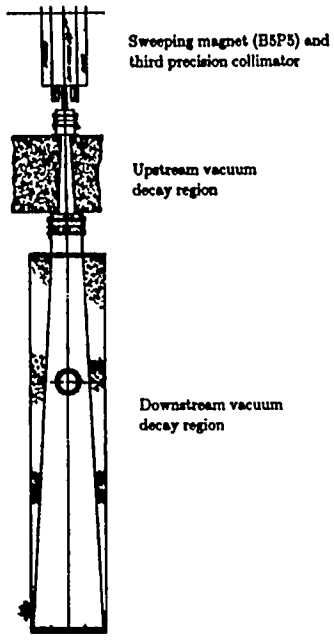

Figure 3.4: Plan view of the downstream beamline, the *vacuum decay region*.

latter part of the run. The AGS proton beam position was monitored using a series of segmented wire ionization chambers (SWICs) and a camera-monitored beam flag. The proton beam intensity was monitored using a combination of telescopes (B5T1 and B5T2) and secondary emission counters (B5SEC and B5SEC'). Both targeting and intensity were also observed with scalars derived from the hardware event triggers.

The beam angles, target composition, and size were optimized for the E791 rare kaon decay experiment, and were used for this experiment because of the difficulty of changing the highly radioactive target immediately after a high intensity E871 test run, and because we had no information which would have allowed us to construct a better target (Section 1.3). .

3.4 Tracking Detectors

3.4.1 Trigger scintillators

The trigger scintillator hodoscopes (TSCs) were the primary triggering signal for the experiment. A left-right pair was located both upstream and downstream of the Čerenkov counters, 3.3 m apart in z. Each of the four banks consisted of 60 vertical counters and 63 horizontal counters. The vertical scintillator slats were 20.1 mm and 1.8 m long. The horizontal slats were 28.1 mm by 1.28 m. The upstream scintillators were 5 mm thick; the downstream 10 mm. Each horizontal slat had one photomultiplier tube (PMT) on the outboard end. The vertical scintillators had PMTs on both ends, each connected to *two* slats. These tubes were staggered so that the exact slat that a particle passed through could be determined from the coincident PMT signals (Figure 3.5) . The scintillator slats were made of Kyowa Glass SCSN-38

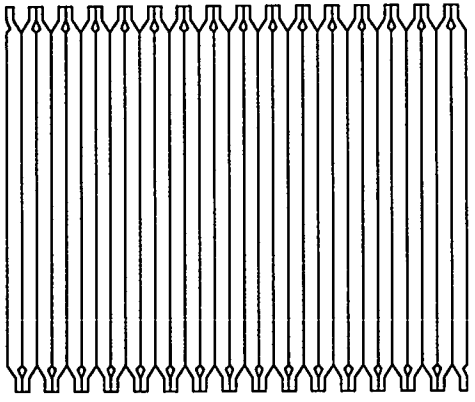

Figure 3.5: Schematic of TSC vertical slat arrangement. The phototubes were placed on the adjoining ends of the slats so that each tube viewed two slats.

scintillator. The PMTs were Hamamatsu R1398.

The signals from the TSC PMTs were sent through RG-8 coax to discriminators, providing the signals used in the initial event trigger. The signals were also sent to the 8-bit, 210 ps resolution Stanford fast time-to-digital converters (FTDCs) for digitization. Signals from these discriminators initiated the triggers determining which events were to be recorded.

The attenuation length of these scintillators was measured to be 1.8 m, and individually, the scintillators were better than 99% efficient.

3.4.2 Spectrometer

The spectrometer was the first detector element encountered by decay products leaving the vacuum decay region. It consisted of five left-right pairs of

drift chambers and two dipole magnets, with the spaces between occupied with helium-filled bags to minimize multiple scattering. The spectrometer provided particle tracking and kinematic information; it measured the momentum of charged particles in the detector. Signals from the first two sets of chambers were also used as part of the initial event trigger. The positions of the chambers and magnets are shown in Figure 3.6.

Magnets

The spectrometer had two magnets of opposite polarity and equal strength, so that particles leaving the spectrometer had approximately the same opening angle as upon entrance. The upstream 48D48 magnet (B5D2) operated at a central field of 6.3 kG, imparting a transverse momentum (p_T) of 300 MeV, such that a positively charged particle was deflected to beam left. Its center was at 21.0 m NTZ. The downstream 96D40 (B5D3) also operated at 6.3 kG (p_T = 318 MeV), and opposite polarity. Its center was at 24.0 m NTZ. Decays were classified as *inbending* or *outbending* depending on the direction of deflection in the first magnet.

The x and y components of the field were measured in January 1986 and again in February 1987. Two Hall probes were mounted on a track, and the fields mapped with a resolution of 2″. During the run, the field strength of each magnet was monitored by a pair of Hall probes mounted to the top-center of each field plate.

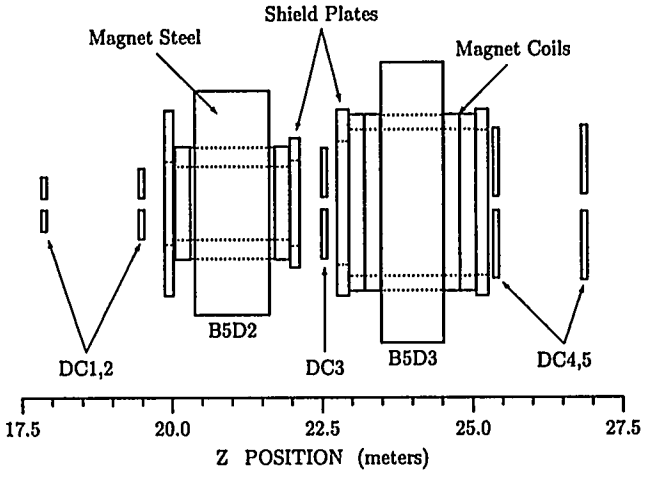

Figure 3.6: Plan view of the E791 spectrometer.

Drift Chambers

There were five left-right pairs of drift chambers (DC), each containing two x and two y wire planes. The first two sets, DC1 and DC2, were located just downstream of the decay vacuum decay window and just upstream of the first magnet. DC3 was between the two magnets, and DC4 downstream of the second magnet. DC5 was upstream of the Čerenkov counters. This arrangement allowed the largest moment arm for the spectrometer possible, and the dual sets of chambers upstream and downstream of the spectrometer provided redundant tracking of particles.

Each left-right set of chambers was a different size, increasing with z,

but the basic construction characteristics of each chamber were the same. A chamber was made of an aluminum frame supporting a G-10 printed circuit board (PCB) on each of the four sides. The PCB was laid out so that each 4.23 mil gold-plated tungsten sense wire was surrounded by a hexagonal cell of 4.3 mil gold-plated aluminum field and guard wires. Each sense wire connection was surrounded by a hexagonal grounded shield trace on the PCB. The wires were soldered into place under tension, 40 gm for the sense wires, and 140 gm for the field wires. The surface of the PCB was covered with a conformal coating compound to prevent the high voltage from arcing. Figure 3.7 shows the layout of one plane of wires.

Each chamber frame was enclosed with an aluminum (0.35 mil) and mylar (0.5 mil) laminate gas-tight skin and a 49/49/2 argon/ethane/ethanol gas mixture flowed through the chambers. Since the 1992 run took place during a particularly humid spring, several of the chamber electronic rails were sealed, and nitrogen gas flowed through the rails to prevent arcing from field wire to guard ring. The total radiation length of each DC, including gas, wires, and Mylar skins was 1.76×10^{-3} radiation lengths (r.l.).

The field wires were operated at 2500 V which was ramped during the beam spill to prevent discharge. The guard wires were held at ground potential to shape the electric field near the edge of the chamber. The sense wires were connected to preamplifiers, mounted on the upper and outermost sides of the chamber. Each preamplifier had a nominal 300 Ω input impedance and a gain of 20. The 8-channel preamps were connected via 17′ 50 Ω ribbon cables to groups of four 8-channel amplifiers which fed 32-channel discriminators and meantimers, located in racks near the drift chambers. The meantimers pro-

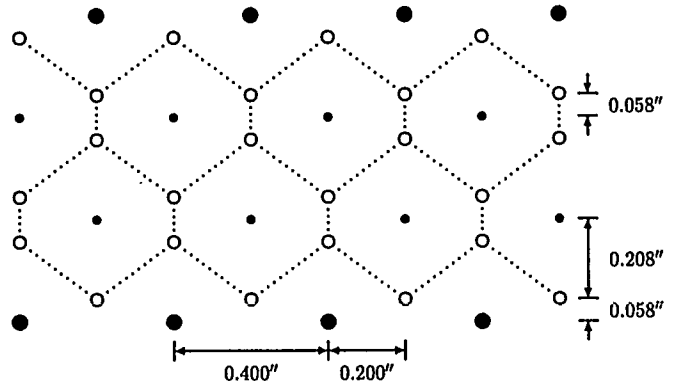

Figure 3.7: Drift chamber cell structure. The open circles represent the field wires, the smaller closed circles the sense wires, and the larger closed circles the grounded guard wires.

duced an ECL signal whose timing corresponded to the sum of times of signals from adjacent wires. Because the sum of the drift times was nearly constant, the meantimer signals were generated at a fixed time with respect to the ionizing particles which generated the signals. The meantimer signals were used to generate the event trigger. The discriminator signals were input to 6-bit 2.5 ns least-significant-bit (LSB) UCLA TDCs via 333′ Ansley cables.

The chambers typically achieved a spatial resolution of 120 μm with a single wire efficiency better than 99%. To achieve this spatial accuracy, the rough positions of the drift chambers were initially found by an optical survey, then the fine positions of the wires found by using straight-through tracks (events with the magnets off). These straight-through tracks were fit

by pattern recognition, and the positions of the chambers as stored in the offline code adjusted to minimize errors. The mass reconstruction of the decay $K_L \rightarrow \pi^+\pi^-$ was used to measure the overall resolution of the spectrometer. These events were also used to adjust the time offsets of the DC meantimers at the TDCs, as corrected in the offline reconstruction code. Further details about the construction, operation, and calibration of the drift chambers can be found in [62].

3.5 Particle Identification

3.5.1 Čerenkov counters

Located between the upstream and downstream trigger scintillators, the threshold Čerenkov counters (CER) were used for particle identification. With a 60/40 mix of He-N_2 gas ($n - 1 = 141 \times 10^{-6}$), the Čerenkov threshold for heavier particles was comparatively high, allowing electron identification. For the first half of the decay search, both counters were filled with the He-N_2 mix. In the second half of the decay search, the left side counter was filled with Freon 12 ($n - 1 = 11 \times 10^{-4}$). In this configuration, the threshold for pions was much lower, allowing discrimination of pions from protons, and rejection of both left- and right-side electrons, and most left-side pions and muons in the Level 1 trigger. The He-N_2 gas mixture was chosen as a compromise between pion and muon thresholds and the number of photoelectrons seen and efficiency. A typical electron in the He-N_2 gas mixture would yield a 4 photoelectron signal. The counters were held at an overpressure of 1.5-3.3 cm of water above atmosphere to prevent contamination. Table 3.1 summarizes the particle momentum thresholds for charged particles in each of the gasses.

		Threshold Momentum (GeV)	
Particle	Mass (GeV)	Helium-Nitrogen	Freon
e	0.000511	0.031	0.0109
μ	0.10566	6.31	2.25
π	0.13957	8.34	2.98
p	0.93827	56.1	20.0

Table 3.1: Čerenkov threshold momentum of charged particles for the two gas mixtures used in E888. $n_{\mathrm{He-N_2}} = 1.000114$, $n_{\mathrm{Fr}} = 1.0011$.

The Čerenkov gas containers were approximately 3 m long × 2 m high × 1.6 m wide, made of 1/16″ aluminum sheet metal boxes on 2″ aluminum beam frame supports, with 1/32″ thick windows on the upstream and downstream end of each counter. The windows were held in place by a 2″ aluminum flange pressed onto a 6 mm O-ring to maintain a gas- and light-tight seal. Figure 3.8 shows a plan view of a counter. Each counter had eight spherical mirrors (radius 2.2 m), arranged in two rows of four. The upper (lower) mirrors focused light onto the PMTs mounted on the top (bottom) of the counter.

Each mirror was made of black acrylic, 1/4″ thick × 39 cm × 89 cm, coated with aluminum evaporated deposition 1 μm thick and a 40 μm MgF_2 anti-oxidation coating. The mirrors were mounted above and below the $y = 0$ axis. Originally, each mirror was optimized to focus the light from the electron from a $K_L \rightarrow \mu^{\pm}e^{\mp}$ decay into a 5″ RCA 8854 Quanticon PMT coated with para-Terphenyl wave-shifter. For the Freon data sample, the left-side Čerenkov mirrors were readjusted so that light from pions was maximized.

The photomultiplier tubes were mounted in steel housings to minimize the effects of residual magnetic fields from the spectrometer. The PMTs were

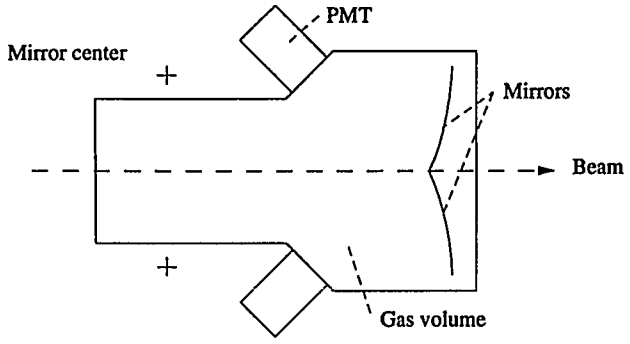

Figure 3.8: Schematic diagram of a Čerenkov counter, side view.

isolated from the helium inside the counters (deadly to PMTs) by a synthetic quartz window, and each tube housing was flushed with pure nitrogen. The housing also contained an aluminized Mylar funnel which served to focus light and increase the effective photocathode area.

The gas mixture was monitored by a Mach-Zehnder laser interferometer system which measured the index of refraction by comparing light traveling through the gas mixture to that passing through a vacuum, and counting the fringes. This system maintained an uncertainty of less than 4×10^{-6} in the index of refraction.

The Čerenkov signals were sent via RG-8 coaxial cable to an 80/20 amplitude splitter panel in the condo, where the larger signal was sent to the Stanford 8-bit fast analog-to-digital converters (FADCs) for pulse-height digitization, and the smaller signal went to CAMAC discriminators. The discrim-

composition by weight	46%	SiO_2
	45%	PbO
	5%	Na_2
	4%	K_2O
density	3.6	g/cm^3
radiation length	3.06	cm
hadronic interaction length	35.0	cm
index of refraction	1.62	

Table 3.2: Properties of the Schott F2 lead glass used in the experiment.

inator outputs were sent both to Level 1 as a part of the online trigger, and to the Stanford FTDCs for event timing.

3.5.2 Lead-glass calorimeter

The purpose of the lead-glass calorimeter (PbG) was to measure the energy of electrons, and to discriminate electrons from hadrons. This glass had been previously used in a SLAC bubble chamber experiment [66] and at SPEAR.

The glass was Schott F2, with 45% PbO composition (Table 3.2). Its density was 3.6 gm/cm^3, with a 3.06 cm radiation length and a 35 cm hadronic interaction length. The glass was somewhat susceptible to radiation yellowing due to impurities in the glass, which could be reversed with exposure to intense ultra-violet light [67]. Radiation damage was not an issue for this short, low-intensity run, but it did affect the design of the calorimeter and its enclosure.

The lead-glass calorimeter consisted of two main parts, the *converters* and the *back* (or absorber) blocks, arranged as shown in Figure 3.9. Each converter block measured $90 \times 10.9 \times 10$ cm. The converters were arranged in

four groups of 13. Each block had a 3.5″ PMT attached, with the innermost 24 tubes using the fast rise-time EMI 9531R PMT and the outermost 28 using slower rise-time Amperex 3462 PMT. Each back block measured 15.3 × 15.3 × 32.2 cm, and were arranged in two arrays of 9 × 12 blocks. Each back block had a 5″ PMT attached via a plastic light guide[2], with the innermost four columns of blocks having fast rise-time Amperex 58AVP PMTs, and the remainder using the slower EMI 9618R PMTs. Each block was wrapped in aluminized mylar and black plastic except for one side to allow for the UV curing of radiation damage; the downstream side of the converters and the upstream side of the back blocks. Both the converter and back blocks were mounted on movable metal frames that allowed the four sections to be moved independently for the UV curing. The entire lead-glass calorimeter was housed in a light-tight hut, which also allowed for temperature control of the array.

Each block had a fiber-optic cable attached to its front via a connector glued to a prism. These fibers were bundled into an incoherent array on the other end, where a nitrogen laser pulsed a blue dye to simulate Čerenkov light from an electromagnetic shower. This pulse, in conjunction with a reference PMT viewing an ^{241}Am α source embedded in a scintillator, monitored light loss due to radiation damage in the glass and variations in PMT performance. The PMTs were sensitive to changes in temperature and high voltage, and some of the PMTs were unstable. The source provided a constant calibration, and it was assumed that the reference PMT changed in the same manner as the

[2]This light guide, the "cookie," was later shown to be the source of the *Marqulies effect*, whereby muons and pions which traversed the cookie deposited slightly more energy than those which did not. This resulted in a two-humped energy peak when these particles were selected, which was for a time quite puzzling.

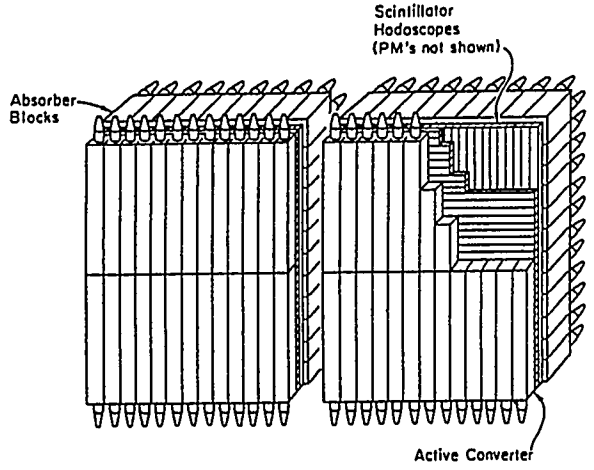

Figure 3.9: Schematic diagram of the lead-glass calorimeter array. The scintillator hodoscope shown were the finger counters, which were not used in E888.

detector PMTs. By monitoring the laser/source references, the calibrations could be compensated for gain changes. The energy/light calibration of the detector was done using electrons from $K_L \rightarrow \pi e \bar{\nu}$ decays.

Each PMT was connected to the counting house via RG8 coaxial cable. There the signal was split 80/20; the larger signal going to the Stanford 8-bit fast analog-to-digital converters (FADCs), the smaller amplified, discriminated and sent to the FTDCs. The calorimeter system was also monitored by a parasitic acquisition system separate from the main acquisition, allowing careful study and monitoring of the calorimeter on an almost constant basis.

Averaging over both fast and slow PMTs, the energy resolution of the PbG was approximately $10\%/\sqrt{\mathrm{E(GeV)}}$. Further information on the lead-glass calorimeter can be found in [69].

3.5.3 Muon hodoscope

The muon hodoscope (MHO) was located between the PbG and the MRG, just downstream of the 0.91 m thick iron hadron filter (8.7 hadronic interaction lengths, 52 radiation lengths).

The MHO was an x-y scintillator hodoscope, consisting of two banks of 11 vertical 2.69 m and 14 horizontal 2.29 m Nuclear Enterprises NE110 scintillators. Each counter was 18.8 cm wide and 1″ thick, and had a 2″ XP2230 PMT attached on both the top and bottom of the vertical counters, and on the outermost end of the horizontal counters. Each scintillator was tapered to 5 cm at the PMT end to improve light collection. The scintillators were wrapped in aluminized Mylar and black plastic. The y measuring slats had the non-PMT end blacked out to prevent reflections. Each signal was discriminated and sent to both a Stanford FTDC and the Level 1 trigger logic.

3.5.4 Muon rangefinder

Downstream of the MHO, the muon rangefinder was composed of marble and aluminum slabs, interspersed with drift tubes. The MRG discriminated muons from any hadrons which survived the PbG and iron by determining where they stopped in the absorber material. Any hadron which did not shower in the upstream material would almost certainly do so in the MRG and stop shorter than a muon of the same momentum, which loses energy only by ionization. Also, muons from $\pi \rightarrow \mu\nu$ which decayed upstream of the MRG could be discriminated from those from $K_L \rightarrow \pi\mu\bar{\nu}$ because the muons from pion decay would stop shorter than expected from the momentum measured by the spectrometer.

Each arm of the MRG was made up of 75 slabs of 3″ marble separated by 3″ gaps. The marble slabs were followed by 25 3″ aluminum slabs on the same spacing. The drift tubes were arranged in the gaps so that a 10% momentum resolution could be attained. The total energy loss for a muon passing through the massive part of the experiment (PbG, iron filter, and MRG) would be ~ 6 GeV.

A total of 13 pairs of x-y measuring drift tube panels were used. Each drift tube was made of aluminum panels forming eight cells arranged in parallelograms. Two 3 mil diameter gold-plated tungsten wires ran down the center of each cell under a tension of 500 gm. Each wire was connected to positive high voltage (2650 V). A 49/49/2 argon/ethane/ethanol gas mixture flowed through the cells. The panels were 18.8 cm wide and 1.2 cm thick. Eleven panels 2.98 m long were glued together to form a vertical plane; fourteen panels 2.22 m long were glued together to form a horizontal plane. Together they formed an active area of 2.25 × 3.01 m.

The capacitively coupled signals from the 16 wires in each plane were amplified and discriminated in electronics modules mounted on the drift planes. The signals were OR'ed together and provided the inputs to the custom latch modules which were read and recorded for every event. The latches recorded the state of each channel as a single bit, which was set if a signal arrived within a 190 ns gate. Efficiencies were measured to be 84-95%.

Chapter 4

Data Acquisition System

4.1 Overview

The E888 acquisition system was designed to handle the data necessary to observe rare decays at the level of one in 10^{11}. This involved the reduction of data from the interactions of more than 10^{12} protons on target in one second, occurring every three seconds, to the 10^4 events/spill that could be written to tape, with very little deadtime. To accomplish this, the E888 acquisition used:

- multi-level programmable hardware and software triggers,
- 200 ns digitization of hit channels,
- sparse readout of only the hit channels,
- two-level buffered event digitizer outputs,
- parallel readout of events in the buffers,
- eight parallel online CPUs with dual-port input buffers.

The signals from the detectors were sent to the lower level of the two-story counting house next to the experimental area. Signals from the various parts of the experiment were delayed with coaxial and ribbon cable so that

they arrived at the appropriate time (determined by their distance from the electronics and the length of time needed to incorporate each level of decision-making logic).

The TSCs initiated every event with signals indicating at least one charged particle track in each arm of the detector, forming the *Level 0* trigger. The discriminated outputs from the DCs, CER, and MHO were delayed and added to the logic to form the *Level 1* trigger. In this way, the first stage of data reduction was accomplished – the TSCs and DCs required at least one charged particle in each arm of the detector, the CER was used to require or reject electrons in either or both arms, and the MHO similarly detected the presence or absence of muons in either arm. Once the Level 1 trigger had made a decision, the analog time and amplitude signals from the experiment, which had been delayed to arrive at their destination after the Level 1 had time to make a decision, arrived at the various digitizers in the custom E791 crates. Each crate contained up to 16 E791 custom digitizer cards. The digitized hit channels in each crate were read out by a Crate Scanner, which in turn were controlled by the Readout Supervisor. The data from each crate was bussed to a set of eight first-in, first-out (FIFO) memories, each of which was dedicated to an online CPU. The Readout Supervisor and the CPU's handshaked to determine which memory/processor was available to accept data. Each CPU ran a fast software pattern recognition algorithm, *Level 3*[1]. The Level 3 software made a very loose mass cut on the reconstructed events to reduce data.

[1]Level 2 was hardware pattern recognition logic, built but never used.

Events which passed the Level 3 algorithm were uploaded to a DEC MicroVAX II via a DR11W interface, controlled by the Readout Supervisor via GPIB, and finally written to 9 track 6250 bits-per-inch (bpi) tape. These tapes were then copied onto 200 Mb IBM 3480 cartridges for archival storage and offline processing.

These stages are explored in more detail below. The acquisition system is described in Ref. [68].

4.2 Trigger

E888 used a three level trigger to determine which events to write to tape. Figure 4.1 shows a schematic diagram of the logic used to generate the signals described below.

4.2.1 Level 0 and Level 1

The first two levels of triggering were Level 0 (L0) and Level 1 (L1). They were comprised of commercial CAMAC electronics, programmable logic, and memory. The inputs to the trigger were the TSC and DC meantimers, and TSC, CER, and MHO signals. The logic was based on coincidences from ECL discriminator signals, which were timed in with the proper amount of delay from cables.

The TSCs initiated each event. Hits in both sides of this detector occurring at the same time (referred to as *in-time* or *coincident*) indicated a charged particle in both arms. The discriminated signals from the upper and lower PMTs of a given x-measuring counter were input to a meantimer; the signals from both the upstream and downstream x-meantimers were required to be

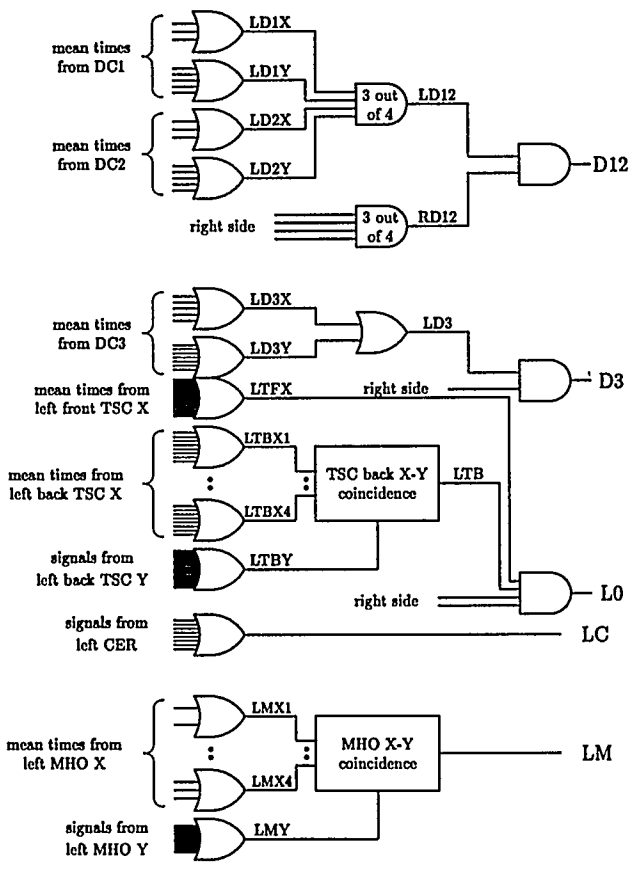

Figure 4.1: Schematic diagram of the Level 1 trigger logic used during the 1992 run. Only the left side CER and MHO signals are shown; the logic for the the right side signals was identical.

coincident with each other and with the downstream y-measuring counter (the upstream y counter was not used in the trigger). This requirement formed the basis of the Level 0 trigger. The resolving time of the TSC coincidence was 16 ns.

Signals from the DCs were used with the L0 trigger to form a *minimum bias* (MB) trigger. A minimum bias event was defined as one which had meantimer signals from at least three of the four planes of DC1 and DC2 ($1x$, $1y$, $2x$, $2y$) and from one or both of the two planes of DC3, in coincidence with each other and with the L0 trigger. The resolution of the former coincidence was 30 ns, the latter 50 ns. The resolving time of the DCs was 56 ns. This relatively long time was due to the wide range of angles of ionizing particles in the DCs, resulting in long dispersion times in the meantimers.

The minimum bias trigger defines the least restrictive condition that can qualify as an event; that is, an in-time charged particle track in both arms of the detector, with no particle identification vetoes or kinematic cuts. A prescaled sample of minimum bias events was recorded along with the physics data (every 100^{th}, 500^{th}, or 1000^{th} event, depending on the L1 trigger). The MB sample was used to monitor the performance of the detector, study the effect of particle identification vetoes, study backgrounds, and provide a valuable particle decay sample, $K_L \rightarrow \pi^+\pi^-$, used for normalization and calibration of the detector.

The Level 1 trigger consisted of the minimum bias trigger in coincidence with signals from the fast particle identification detectors (CER and MHO). The CER and MHO discriminator signals were used to identify electrons, pions, and muons. A 'physics event' was one which met the MB criteria, plus the additional requirements imposed by the L1 trigger. The latter depended on

Definition	Explanation
L0*DC	Minimum Bias
L0*DC*($\overline{\text{LMHO} + \text{RMHO} + \text{LCER} + \text{RCER}}$)	He-N_2– μ_L, μ_R and e_L, e_R veto
L0*DC*($\overline{\text{LMHO} + \text{RMHO}}$)	μ_L, μ_R veto, 10 runs
L0*DC*($\overline{\text{LMHO} + \text{RMHO} + \text{LCER}}$)	μ_L, μ_R and e_L veto, 5 runs
L0*DC*($\overline{\text{LMHO} + \text{RMHO} + \text{RCER}}$)	Freon – μ_L, μ_R and e_R veto

Table 4.1: Level 1 physics trigger definitions. The primary physics triggers were He-N_2 and Freon. Minimum bias was used for calibrations, and the others were used on only a small fraction of the data.

the way the L1 trigger was programmed and could be used either to require the presence or absence of a particle in either arm. The L1 definitions used in E888 are given in Table 4.1. During the He-N_2 phase, the L1 trigger had vetoes on events with hits in either arm of the MHO and CER, to reject events with muons and electrons. During the Freon phase, the left-side CER veto was removed, so that this rejection could be made offline and the effect of the Freon studied, while still rejecting electrons on the right side and muons on both sides.

Each event was numbered with the spill number, and an event number within the spill. This information was transferred along with other L1 information to the Level 3 processor, and written to tape.

The L1 trigger also provided calibration triggers to the data acquisition for detector calibration. These included the 50 Hz pulses which kept the PbG ADCs from saturating during the out-of-spill duty cycle, the laser triggers which the PbG used as a calibration, ADC pedestal events, and a pulser used for analyzing detector responses.

4.2.2 Level 3

Level 3 (L3) used information from the first three DCs and a magnetic field integral lookup table to calculate an approximate two-body mass. A parallel farm of eight processors each implemented this algorithm. The processors were designed at SLAC and CERN to emulate the IBM 3081 instruction set, which was the mainframe used for the offline analysis. Each processor had a dual-port FIFO memory buffering its input. Each memory was composed of several memory boards, each of which had up to 2 Mb of static RAM, and one which had 512 Kb. The processors had a handshake protocol with the Readout Supervisor to route events to the processors which were not busy, and allow those with full memory to digest their events.

L3 Algorithm

To perform the fast pattern recognition and mass calculation needed to make a decision before the next beam spill (in order to allow enough time for the event to be written out), L3 first unpacked the drift chamber time-to-digital converter information, and identified single hits, in-time hits on adjacent pairs of wires (doubles), and triple hits in the first 10 planes of the chambers (1L/Rxy, 2L/Rxy, and 3L/Rx).

To identify the tracks, all possible combinations of the hits from planes 1Lx, 1Rx, 2Lx, 2Rx were looped over, and the quantity

$$Q_x = |(x_{1Lx} + x_{1Rx}) - C_x(x_{2Lx} + x_{2Rx})| \tag{4.1}$$

evaluated. A similar equation was evaluated for the y positions. ($C_{x,y}$ were calculated offline using $K_L \rightarrow \pi^+\pi^-$ events.) The two four-hit combinations

giving the lowest values of $Q_{x,y}$ were stored, then the four-hit combination with the best vertex match chosen.

For all combinations of these tracks and the hits in the third drift chamber, the momentum of each track was calculated using a lookup table of the magnetic field integral. For combinations which had both tracks inbending or both outbending, the mass was computed as $m_{p_L\pi_R}$ and $m_{\pi_L p_R}$ ($m_{p\pi}$ and $m_{\pi p}$, for Λs and $\overline{\Lambda}$s, respectively) according to the small angle approximation

$$m_\Lambda^2 = m_L^2\left(1 + \frac{p_L}{p_R}\right) + m_R^2\left(1 + \frac{p_L}{p_R}\right) + p_L p_R \theta^2 \tag{4.2}$$

where $m_{L,R}$ and $p_{L,R}$ are the mass and momenta of the left and right side tracks, and θ is the opening between the two tracks. If any combination of the tracks and DC3x hits had $m_\Lambda^2 < 1.128$ GeV^2 (either Λ or $\overline{\Lambda}$), the event passed L3 and was written to tape.

4.3 Event Readout

The Readout Supervisor (RS) controlled the flow of events from L1, digitizers, and L3. When L1 accepted an event, it notified the RS and generated the gates and starts for the ADCs and TDCs. When the RS was unable to accept an event, whether because the last event was still being digitized or because the L3 memories were full, it disabled L1.

Each digitizer crate had a Crate Scanner (CS) module, which controlled the flow of data from the digitizers to the 3081/Es through a handshake protocol with the Readout Supervisor (RS). The CS communicated with the digitizers via a custom protocol over the backplane of each crate. A digitizer board with data ready for readout asserted a signal to the CS, which informed the RS

that it had data. When the RS was ready to route data, it enabled the CS, which then enabled each board with data in turn. Each board then sequenced through the channels with valid data, putting the data on the backplane along with the address of the channel. This continued until all the valid channels on the board were uploaded. The CS then enabled the next digitizer board in the crate to upload its data. The RS routed this data to one of the L3 3081/Es. The emulators communicated with the RS to let it know whether their input memory was full or available for more data.

In this way, only those boards, and only those channels on each board with valid data were read out (the 'sparse' read out), and the data was shunted appropriately to the L3 CPU which was available to process the data.

Each data word contained the address of the channel, board, and crate from which it came. To ensure that the digitized data matched the L1 trigger, each event was assigned an event number, which was also added to the data word. This word was checked later to verify that the digitization data matched the L1 event data.

4.4 Online

The L3 processors were connected to a DEC MicroVAX (the ACQ) which set L3 trigger, started and stopped runs, monitored detectors via online histograms, and controlled tape writing. Two 6250 bpi 9-track tape drives were controlled by the ACQ, which alternated writing between them. Maximum tape writing speed was about 10 000 events per spill, and a tape filled in about 20 minutes. The ACQ also allowed online monitoring of data and histograms to monitor detector performance for dead channels, etc.

4.5 Monitoring

Many voltages and temperatures in the experiment were monitored continuously by a scanning ADC interfaced to an Apple II computer. These ADC values were connected to an audible and visual alarm system which triggered when voltages or temperatures exceeded a preset range. In this way, the accuracy of the experiment, which depended on these values, was maintained. For instance, the accuracy of the ADCs was very sensitive to the -2 V supply used to generate the Sony A/D converter reference voltage. The PMTs in the PbG were also sensitive to temperature fluctuations, so the temperature in the PbG hut was monitored and alarmed. Temperatures in the L1, L2, and L3 areas were monitored constantly; an failure of the air conditioning, which was maintained at a blustery 65 °F (with a 20 mph wind generated by cooling fans), would have surely reduced the electronics to a pool of molten solder.

In addition to electronic monitoring, voltages, temperatures, and gas flows were checked manually every shift (nominally three times per day).

The scanning ADC values were also recorded to tape. This allowed values such as the voltage and current from the Hall magnetic field monitors to be recorded for further study.

4.6 Digitization

4.6.1 ADCs

The electron particle identification detectors (CER, PbG, and FNG) were read into the 8-bit Stanford fast analog-to-digital converters (FADC) [69]. These FADCs were charge integration devices; when L1 determined that an

event was to be digitized, it sent a gate which began the digitization process on each board. The gate signal was common to each board, and was tailored for the type of detector and PMT to be digitized. The gate triggered internal logic on the board which opened a high-impedance CMOS switch allowing charge to accumulate on a small capacitor. The pulse from the detectors was delayed to arrive simultaneously with the gate, and was amplified in the first stage of the FADC channel. At the appropriate time, the switch would close, and another would open, allowing the accumulated charge to present a steady voltage as the input to the Sony sub-ranging 8-bit A/D converter. The output of this device was buffered by a set of latches so that the next event could be digitized while the previous event was being read out. The digitization of each event required 200 ns; deadtime was minimized by buffering outputs and using the sparse readout. For increased resolution at low energies, the ADCs were bilinear. Small signals, below a count of 64, had a resolution of 0.150 pC/ LSB, while those from 65-255 counts had a resolution of 0.450 pC/LSB.

Each FADC board contained 12 ADC channels. Each channel had an individually controlled analog threshold comparator which set a level below which signals would not be digitized. Each 8-bit digital A/D output was input to a digital comparator which, when triggered, set the three bit word containing the address of the channel to be read out. This also set a flag for each channel which was OR'ed together to provide a backplane signal which informed the Readout Supervisor that this board had valid data to be read out.

The ADCs were calibrated in a three step process. The pedestals of each channel were adjusted at the beginning of the run and monitored on a daily basis to ensure that, with no signal, the digital output was greater

than zero, but not so high as to significantly reduce the dynamic range of the A/D converter. Typically, the pedestals were required to be between 3-10 counts, with a fluctuation less than 2 LSBs. The charge-to-LSB calibration was obtained by applying an accurately measured voltage to a special backplane input which was common to all channels on all boards within a crate. The energy-to-charge calibration was derived by using the electrons from K_{e3}s in a special L1 electron trigger to obtain high statistics. The momentum of these electrons was known from the spectrometer.

The ADCs used a 50 Hz signal from L1 to keep charge from accumulating on the integrating capacitor during the AGS out-of-spill time.

By maintaining this regimen of ADC calibration, including alarms on out-of-range ADC supply voltages, very good stability of the ADCs was maintained.

The ADCs were monitored by a parallel acquisition system, which parasitically intercepted calibration events and read them into a MicroVAX running a subset of the online acquisition system. This allowed the ADC systems to be monitored almost constantly.

4.6.2 TDCs

6-bit UCLA TDCs

Timing information from the DC meantimers, TSC y-meantimers, and the PbG were digitized in the UCLA-designed time-to-digital converters (TDC) [70]. Each board had 32 channels, providing a 2.5 ns LSB over 160 ns. The TDCs were also buffered for the sparse readout.

Timing of the TDCs was started by a gate from L1, common to all the

inputs. The stop signal was generated by the discriminators from the various detectors. Only channels that received a stop signal within the dynamic range of the TDC were read out. This data was available for read out within a few nanoseconds of digitization.

8-bit Fast TDCs

Timing information from the TSC x-meantimers, Čerenkov counters, and muon hodoscope was digitized using the 8-bit Stanford-designed FTDCs [71]. Their digitization and readout were identical to the FADC boards, with the analog amplifier input section replaced by a constant current source. A common start signal from L1 opened the CMOS switch on all the boards and allowed charge to accumulate on the integrating capacitor proportional to the amount of time the gate was left open. Again, the stop was provided by a discriminator signal from the appropriate detector. The voltage from the accumulated charge was then presented to the input of the A/D.

The FTDC A/Ds were linear, and had a resolution of 210 ps/LSB. The digital output was read out in exactly the same manner as the FADCs. These modules also used the sparse read out.

4.6.3 Latches

Hit information from the MRG and the TSC was recorded by 26 latch modules, each with 3 channels of 32 bits. All these bits were read out on every event.

Chapter 5

Analysis

Wheresoe'er I turn my view,
All is strange, yet nothing new;
Endless labour all along,
Endless labour to be wrong...
–Samuel Johnson

I will discuss the analysis of the data in several parts. First, I will describe the analysis software (the *offline* code), which was designed to process the data taken by this detector. Next, the method by which the data was reduced from the original tapes is described. This reduction selected events based on minimum standards of event quality, and was in many ways independent of the final processes searched for. The backgrounds of the experiment, those processes which mimic the signal we are attempting to find, will be discussed. These determine many of the cuts. Knowing the backgrounds and their characteristics, I will explain the cuts made to the signal sample to obtain the final set of events. Once the final set of cuts is established, I will describe their application to the normalization sample, and some of the other issues involved in determining the final sensitivity of the experiment. The results of the experiment can then be stated as a combination of the H signal selection and the normalization.

To set the stage for this work, I will first describe how the final results will be determined, so that in the following sections, it is clear how each part contributes to the final answer.

5.1 Sensitivity of the Experiment

The number of H dibaryons observed in the detector will be the product of the number of protons on target times the fraction of those interactions which result in an H, times the probability that the H and its' decay products enter the limited volume of the detector and have the necessary kinematics to induce a signal in the detectors, which of course are not 100% efficient. This can be written as

$$N_H^{obs} = N_p P_p^{int} \frac{\frac{d\sigma_H}{d\Omega}\Delta\Omega}{\sigma_p^{abs}} P_H^{dk}(\Delta z)\,\mathrm{Br}(H \rightarrow \Lambda X)\, A_H\, \beta^A\, \epsilon_H \qquad (5.1)$$

where

N_p is the number of protons incident on the target,

$P_p^{int} = 1 - e^{-L/\lambda_{abs}}$ is the probability that a proton interacts in the target; λ_{abs} is the proton absorption length in copper, and $L/\lambda_{abs} = 1.38$ for this target,

$\frac{d\sigma_H}{d\Omega}\Delta\Omega/\sigma_p^{abs}$ is the fraction of proton interactions that go into Hs ($p + \mathrm{Cu} \rightarrow H +$ anything),

$P_H^{dk}(\Delta z)$ is the probability that an H with momentum spectrum $\mathcal{P}_H$, where $\left(\int_{p_L}^{p_H} \mathcal{P}_H\, dp = 1\right)$, decays in the region from which decays are accepted (z_1 to z_2)

$$P_H^{dk}(\Delta z) = \int_{p_L}^{p_H} \mathcal{P}_H(p) P_H^{dk}(\Delta z, p)\, dp$$

or

$$P_H^{dk}(\Delta z) = \int_{p_L}^{p_H} \mathcal{P}_H(p)(e^{-z_1 m_H/p c\tau_H} - e^{-z_2 m_H/p c\tau_H})\, dp, \qquad (5.2)$$

$\mathrm{Br}(H \rightarrow \Lambda X)$ is the sum of the branching ratios $H \rightarrow \Sigma^0 n$ and $H \rightarrow \Lambda n$, the Λ decay modes observable in the E888 detector (for kinematically allowable values of m_H, there is also an $H \rightarrow \Sigma^- p$ mode, which cannot be reconstructed due to the undetected neutron of the $\Sigma^- \rightarrow n\pi^-$ decay).

A_H is the acceptance of the detector for Hs (defined in Section 10.2),

β^A is a Monte Carlo acceptance correction factor (Section 10.2), and

$\epsilon_H = \epsilon_H^{cuts}\epsilon_H^{det}$ where the former is the efficiency of cuts applied to Monte Carlo acceptance[1]; the latter is the efficiency of the detector, including Level 3, particle identification, reconstruction, and deadtime.

A similar discussion for Λs leads to an equation identical to Equation 5.1 with the H subscript replaced by Λ. To find the sensitivity of the experiment, we divide the two equations and solve for the differential production cross section of the H

$$\frac{d\sigma_H}{d\Omega} = \frac{N_H^{obs}}{N_\Lambda^{obs}} \frac{\mathrm{Br}(\Lambda \rightarrow p\pi^-)}{\mathrm{Br}(H \rightarrow \Lambda X)} \frac{A_\Lambda}{A_H} \frac{P_\Lambda^{dk}(\Delta z)}{P_H^{dk}(\Delta z)} \frac{\epsilon_\Lambda}{\epsilon_H} \frac{d\sigma_\Lambda}{d\Omega}. \qquad (5.3)$$

[1]The Monte Carlo typically has better event reconstruction characteristics, such that reconstruction χ^2s, for instance, are smaller than their real-world counterparts. The same cut applied to both quantities would cut fewer events in the Monte Carlo sample, so relaxed cuts are applied to MC events, then the measured efficiency of the tighter cuts on real data is applied to the total number of MC events as a percentage of events cut; e.g., if a χ^2cut of 5 reduces the number of events in the data sample by 20% relative to that of a χ^2cut of 25, the cut is said to be 80% efficient. Calculations of quantities such as number of particles predicted then have this reduction applied by hand.

N_Λ^{obs} and N_H^{obs} are the quantities we seek from the normalization and signal data samples, respectively. Br($\Lambda \rightarrow p\pi^-$) is found from the Particle Data Book [58] and Br($H \rightarrow \Lambda X$) is taken from Donoghue, *et al.* [2]. The acceptances A_Λ and A_H are found from Monte Carlo simulations. $P_\Lambda^{dk}(\Delta z)$ and $P_H^{dk}(\Delta z)$ can be calculated, given the respective Λ and H production momentum spectra. The production momentum spectrum $\mathcal{P}_H(p)$ upon which the H acceptance depends is unknown, and is thus varied to find the dependence due to this uncertainty in the initial momentum spectrum. The differential production cross section of the Λ, $d\sigma_\Lambda/d\Omega$, is derived from published experiments. It is reasonable to assume that the H and Λ efficiencies are identical since the primary observable decay product of the H is the Λ; the difference being p_T. I will take this ratio to be one throughout the analysis. All the other factors have fortunately divided out, so variables with large uncertainties, such as the number of protons striking the target, do not enter the final sensitivity calculation.

These then are the numbers we must obtain, and the rest of this thesis is devoted to the explanation of how they were gotten.

Chapter 6

Offline

The offline analysis of data occurred in stages. At different phases in the data reduction, the focus was on a particular stage. Here I give a brief overview of the offline program, then discuss each stage of the offline in detail. In the data reduction sections, I discuss how the offline was applied to each reduction of data. A flowchart of the offline is shown in Figure 6.1.

Data entered the offline processing in one of three ways. The first, of course, was real data read from tapes. The second was to generate Monte Carlo (MC) events with the offline code (Stage 1), swim them through the detector using the magnetic field maps (Stage 2), generate simulated detector responses and digitize these responses (Stage 3), and pack the digitized data in exactly the same manner as real data was recorded (Stage 4). At this point, the packed data could be (and often was) written to tape for future analysis, or continue directly into the next stage. Analysis was fast; generation was slow, so MC events were precious and were reused whenever possible. After Stage 4, MC and experimental data were treated identically.

All events went into a raw event buffer and were unpacked (Stage 5). Unpacking was the process of assigning the data from an electronics channel (*e.g.*, an ADC or TDC output) to a particular PMT or wire. The responses of

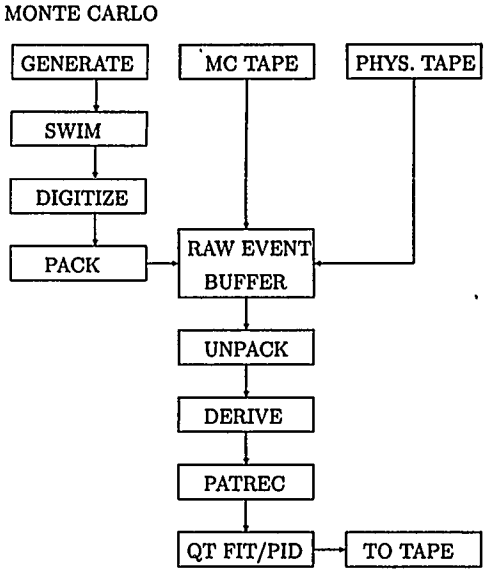

Figure 6.1: Offline analysis flowchart.

the detector were derived (Stage 6), *i.e.*, the energies, positions, and momenta were derived from the digitized events and the calibrations of the detectors. The events were pattern recognized (Stage 7); that is, detector responses were associated with tracks in the tracking detectors (DCs, TSCs), and events whose hits in the detector did not form connectable tracks and or had tracks which exited the detector were discarded. These tracks were associated with particle identification detectors (Stage 8) by projecting the tracks to the detector elements (track-counter association). Events surviving pattern recognition were then fit by the FT and QT fitters, which performed a more accurate fit using the entire magnetic field integral and calculated event quality measures (Stage 9). Often track-counter association was redone (or done for the first time) in this stage with the better track fits. Track-counter association also simulated the PID detector response based on the projection information and momentum and compared the actual hit to the simulated hit for various particle hypotheses, calculating different measures of goodness for the hit.

Event quality cuts could be made in this stage, discarding those with large χ^2, for instance. Particle identification (PID) was also done in this stage, identifying electrons, muons, pions, and protons using the fitter information, the simulated track response, and the actual detector response.

Events were monitored throughout this entire process, keeping track of where events were cut, and this information was summarized at the end. Remaining events were written to tape if so desired (Stage 10).

There are also many branch points in the program to handle special events, such as detector calibration events. Typically these events were processed early in the analysis, then once the derived commons were written out,

discarded.

6.1 Monte Carlo

The Monte Carlo simulation of the detector and particle decays gave us much of our knowledge of how things behave, since the interaction of detector geometry and particle kinematics make it very difficult to understand *a priori* the resulting experimentally observable quantities of momentum, energy, position, and their distributions. By using the MC simulator, we can optimize the detector and the cuts used to reduce the data.

The MC simulation began with the generation of a particle within the target. An x-y point was randomly[1] generated from a uniform probability distribution 10 m downstream of the target within a 100 μsr swath 100 cm high by 10 cm wide. A momentum was selected for this parent particle based on a momentum distribution (this point will be examined in detail later). These two quantities determined the momentum vector of the decay, which was then Lorentz-boosted to the lab frame. The lifetime of the particle was chosen randomly from an exponential distribution such that it decayed within a preselected region in z, usually chosen to be within the vacuum decay region. There was no point in generating decays which would not be accepted by the detector; thus limitations were placed on the momentum, lifetime, and decay point of the generated particle to make best use of our computer time. If desired, the branch that the particle decays into was also chosen randomly proportional to the physical branching fractions, though for many purposes, the simulation was

[1] Of course, 'random' in this case, and in all cases of computer generated probabilities is really pseudo-random.

forced into a single branch to clarify a particular background or decay.

Once the decay position and branch of the parent was chosen, the daughters of the decay were generated in the same manner. The momentum of the daughters was chosen from Dalitz distributions of the appropriate two- or three-body decay and the direction of decay chosen in the parent's center-of-mass frame, then the daughters boosted to the lab frame. If the daughters were also unstable, these particles were also decayed in the same manner, until a step was reached where the particles decay into fundamental particles or stable neutral particles that could not be tracked by our detector. Electrons, protons, and gammas were of course stable and decayed no further, while the muon, with a $c\tau$ of 659 m, was essentially a stable particle.

For kaon decays, the momentum of the generated kaon was chosen from a distribution based on the parameterization of Skubic *et al.* [76]. This spectrum was studied in detail and its shape agreed very well with the observed kaon decay properties. H and Λ momentum spectra will be considered in detail in Chapter 10.

Once the daughters were generated, the tracks of these particles were projected through the detector and its magnetic fields. Those tracks which were projected to exit the detector were discarded. The projection of the tracks included simulated effects of multiple scattering and bremsstrahlung. The magnetic field maps used to adjust the track positions of the particles were the same as those used for fitting the tracks of real particles. As a result, MC events typically had better event reconstruction characteristics, because they were refit by being projected through the same magnetic field used to generate them, whereas real particles were fit using a field which only approximated the

magnetic field they encountered in the detector.

Once the positions of the particles passing through the detector were determined, the response of the detector to the particles was simulated and digitized. The responses of detectors were based on measured quantities, and the results smeared according to measured distributions. For instance, the finite drift chamber resolution was simulated by smearing the detector response according to a Gaussian distribution with a width of 150 μm. Simulated hit times were quantized according to the resolution of the appropriate TDC, as were pulse heights measured by ADCs.

In general, the response of the particle ID detectors was not calculated, since the MC simulation tended to be better than real data for reasons which were not well understood, and because simulating them took too much CPU time. The response of these detectors (CER, PbG, MHO, and MRG) was studied by using data from minimum bias triggers.

After the detector response was digitized, the events were packed into a raw event buffer, identically to real data. The processing of MC events was then identical to real data in all stages thereafter.

The Monte Carlo program is described more fully in Ref. [72].

6.2 Pattern Recognition

After an event was unpacked and derived, pattern recognition (PR) was applied to the event. This was the process of connecting hits in the TSCs and DCs to form tracks. First we must define a good hit in the DCs and TSCs.

Drift chamber hits were determined by the distance-of-closest-approach

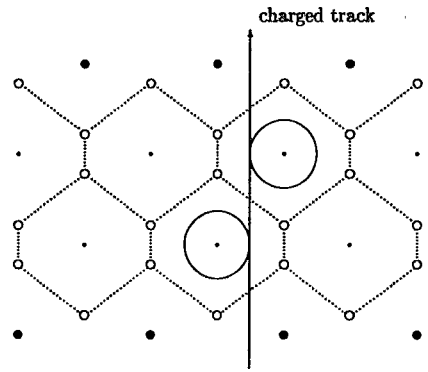

Figure 6.2: An idealized track in a drift chamber. The *distance of closest approach* is the solid circle around the sense wire.

(DOCA) of a particle track to a wire, derived from the TDC information and the known drift velocity of the gas. Good hits had a relatively constant sum of DOCAs. Figure 6.2 shows an idealized DC hit and the DOCAs of the hit wires. This situation could be complicated by high angle tracks which caused hits in more than two wires, or by inefficient wires, which would cause only a single hit. Noise in the wires and accidental coincidences could also cloud the situation. DC hits had to pass a DOCA cut which removed the worst noise. Tracks were required to have at least one single, double, or triple hit in both views of each plane of the DCs. Also, three of the five planes in each view were required to have good DOCA pairs or triples.

TSC hits were found from the TDC information and TSC latch modules.

Early hits in the TSCs could result in either no hit or a hit with a time of zero recorded. Good hits were defined as hits with good TDC times or as a hit with $t = 0$ and a latch hit. Two good x-view TSC hits in each track were required.

To form a track, good hits in the upstream and downstream TSCs were correllated. This was done separately in each arm of the detector, in both x and y. These correllated tracks were projected upstream to DC4 and DC5, and hits in the proper regions of these chambers were associated with the track projection. These tracks were then extended to DC3, but since the momentum and charge of the particle was unknown, the region in which a valid hit could have occurred was large. Once a hit was associated with the track in DC3, though, the window in which a hit would be accepted from DC1 and DC2 was quite constrained, since there was now a momentum and charge to predict the location of the next upstream hit.

The two-dimensional tracks formed by this method were evaluated by their χ^2, defined by the quality of the track segments in DC1-2 and DC4-5, and the bad tracks rejected by a χ^2 cut. The χ^2 was calculated by comparing the track positions determined by the DOCAs in these chambers to a straight line projection, and the expected position in DC3 to the actual hits. From the good 2-D tracks remaining, 3-D tracks were formed, and another χ^2 cut applied. The 3-D χ^2 cut was composed of the sum of the 2-D χ^2s and the front-back momentum differences. The momenta were found from a magnetic field integral look-up table.

Once tracks were formed using all the drift chambers, all the candidate x and y tracks were looped over to find the pair of tracks forming the vertex with the smallest distance of closest approach. The opening angle and the track

momenta were now known, and pattern recognition could calculate various two-body invariant mass hypotheses ($p\pi$, πp, $\pi\pi$, etc.).

The track angle information found by forming tracks was used to resolve some of the left-right ambiguities in the DCs from triples or adjacent pairs of hits. Single hits were simply assigned the position of the wire.

Pattern recognition is described more fully in [64, 65].

6.3 Fitting

Once tracks have been associated with DC and TSC hits, the pattern recognition information was passed to the more accurate track fitting routines. E888 used two fitters, colloquially known as FT and QT, working by very different methods. The results quoted throughout this dissertation are taken from the QT fitter, and only that fitter will be described here. The FT results were also carried through in parallel as a check. The results of the two fitters did not differ significantly.

The QT fitter worked by projecting tracks through the measured magnetic fields of the upstream and downstream magnets independently ("swimming") and requiring them to meet at DC3. This was done iteratively to obtain the best fit to the hits in the chambers. To define a best fit, we must define some event quality parameters by which to judge an event.

A particle's trajectory is completely defined by its three-momentum and three-position. The z position was fixed by the DCs location. The remaining five variables were taken by the QT fitter to be p, x, y, θ_x, and θ_y. Each track had ten position measurements, five x and five y, leaving 5 degrees of freedom

to fit the track.

Each trajectory was swum from DC5(1) to DC4(2) based on pattern recognition information. The trajectory was then swum through the magnetic field to DC3, where it was required to be within 10 μm of the DC3 hit. In y (where there was nominally no magnetic field bending of the track), the tracks were extended to DC2(4), where the angle difference between the two tracks was calculated ($\delta\theta_{y_{2,4}}$). For the x-view, the angle $\delta\theta_{x_2}$ was calculated; these differences were the scattering angle corrections, and were used in the next iteration to improve the fit. If these angles were not zero, a kink was introduced into the track. Another useful measure was δp, the difference in momentum between the two halves of the spectrometer. Unfortunately, δp and $\delta\theta_{x_2}$ were correllated by the charge of the track, so a normalized degree of freedom orthogonal to δp was constructed: $\delta q \equiv \frac{\delta p}{\sigma_p} + q\frac{\delta\theta_{x_2}}{\sigma_{\theta_{x_2}}}$.

The χ^2s used to define track quality were

$$\chi^2_x = \frac{1}{2}\begin{pmatrix} \delta p & \delta q \end{pmatrix}\begin{pmatrix} \sigma_{pp} & \sigma_{pq} \\ \sigma_{pq} & \sigma_{qq} \end{pmatrix}^{-1}\begin{pmatrix} \delta p \\ \delta q \end{pmatrix} \tag{6.1}$$

$$\chi^2_y = \frac{1}{3}\begin{pmatrix} \delta\theta_{y2} & \delta\theta_{y3} & \delta\theta_{y4} \end{pmatrix}\begin{pmatrix} \sigma_{22} & \sigma_{23} & \sigma_{24} \\ \sigma_{23} & \sigma_{33} & \sigma_{34} \\ \sigma_{24} & \sigma_{34} & \sigma_{44} \end{pmatrix}^{-1}\begin{pmatrix} \delta\theta_{y2} \\ \delta\theta_{y3} \\ \delta\theta_{y4} \end{pmatrix} \tag{6.2}$$

The covariance matrices were calculated from Monte Carlo simulations of the detector.

The vertex χ^2 was calculated from the minimum DOCA of the tracks forming the vertex (d) and the uncertainty of the projection of the tracks at the first drift chamber ($\sigma^2_{\theta L,R}$)

$$\chi^2_{vtx} = \frac{d^2}{(z_{DC1} - z_{vtx})^2(\sigma^2_{\theta L} + \sigma^2_{\theta R})} \tag{6.3}$$

where z_{DC1} is the z position of DC1 and z_{vtx} is the vertex z position.

The QT fitter is described in detail in Ref. [64, 65, 73].

Chapter 7

Data Reduction

The art of our necessities is strange,
That can make vile things precious.
–William Shakespeare, King Lear

During the data-taking phase of the E888 H-decay seach (May 29, 1992 to June 11, 1992), 354 6250 bpi tapes were written and consecutively numbered from 30000-369 (a bad batch of tapes accounts for the discrepancy between the number of tapes written and the tape numbers). These are the *raw* data tapes. Each tape corresponded to one run number. All further references will be to these run numbers.

The first 54 runs were largely calibration tapes for different detectors. Run 30054 contains the first data with beam, but Level 3 was in a pass-through mode until 30138, *i.e.*, it calculated all quantities, but made no cuts based on its results. 30138-369 thus constitute the bulk of the H-decay data. A total of 207 runs with a L1 physics trigger were taken and processed, 175 with physics (non-passthrough) L3 code operating. Approximately half the runs were taken with He-N_2 in both Čerenkov counters and half with Freon in the left Čerenkov (30269 and up). The remaining non-physics runs were minimum bias and calibration L1 triggers, which were periodically taken in order to monitor the

detector.

The events were required to pass through several stages of analysis and data reduction. In the first stage, called Pass 1, both minimum bias and physics events were subjected to pattern recognition and fit. A very loose mass cut was made on physics events in this pass. Data passing the fit and the mass cut was written to tape for further analysis. After Pass 1, the data was divided into two streams, Λ physics and minimum bias, and the two written out separately. At this stage, loose cuts were made on event quality and kinematic characteristics. This reduced the physics data down to a manageable level, eighteen 200 MB tapes of minimum bias and eighteen of Λ physics data. The Λ physics stream was then divided into three non-exclusive streams (high-p_T, low θ_C^2, and Λ mass) and these written to tape. The high-p_T data formed the H selection sample; the low θ_C^2 data the normalization sample. All of these data reduction steps will be discussed in detail in the following sections.

7.1 Pass 1

The first analysis and data reduction occurred in Pass 1. Here the raw events written to tape were checked for errors, pattern recognized and fit. Surviving events were written to tape. Due to problems with drift-chamber calibrations and survey in the initial production, this Pass 1 was done twice. This production is described in detail in [74]. The mass resolution of $K_L \rightarrow \pi^+\pi^-$ was reduced from a σ_m of 1.73 MeV in the first production to 1.54 MeV, which compares well to previous E791 results of 1.5 MeV [65].

In Pass 1, events were sorted on the basis of the L1 bits. Figure 7.1 shows the flow of events through Pass 1. Every 5000^{th} event was selected and

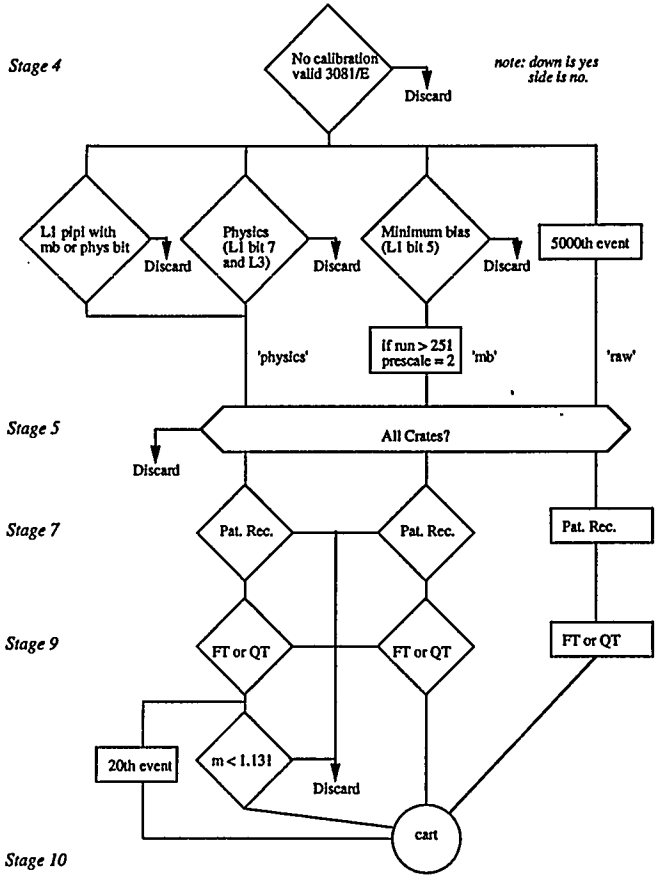

Figure 7.1: Flowchart of events through Pass1.

Total number of:	
Events recorded	21 629 429
Events reconstructed	11 382 580
Events surviving Pass 1	6 015 610
Physics events recorded	17 323 564
Physics events surviving Pass 1	4 327 993
MB events recorded	3 933 047
MB events surviving Pass 1	1 415 618
Raw events surviving Pass 1	4 251

Table 7.1: Summary of events recorded by the experiment and written out by Pass 1.

written to tape ('raw' events), regardless of whether that event passed PR and fitting. In the He-N_2 sample, all MB events passing PR and fitting were written out. In the Freon sample, MB events were prescaled by a factor of two before pattern recognition because of a L1 prescale change during the data-taking. All Freon MB events passing the MB prescale, PR and fitting were written out. In order to not have to calculate the L3 efficiency, only physics events which passed L3 were processed (no pass-through L3). All physics events passing pattern recognition and the fitter with $m_{p\pi} < 1.131$ GeV were written out. A prescaled sample of the events passing pattern recognition and the fit regardless of the mass cut were kept. All events other than these were discarded.

The result of this strip was a one-to-one transfer of stripped events: one raw data tape resulted in one Pass 1 output tape. The average raw data tape contained 130 000 events; the average Pass 1 output tape contained 60 000 events with each event now expanded to include information derived from the pattern recognition, fit, and Pass 1 analysis. Table 7.1 gives a breakdown of the total numbers of events taken, reconstructed, and written to tape.

7.2 Event Strips

To reduce the original 175 Pass 1 output tapes to a manageable number, the Pass 1 tapes were stripped into two streams, physics and minimum bias. Minimal event quality, kinematic, and particle identification (PID) cuts were applied to the physics (Λ) stream. These requirements are listed in Table A.1 under PSL4, and are discussed in detail in Section 9. This reduced the number of tapes to 18, each containing roughly 50 000 events (total 908 116 events).

The minimum bias sample was subjected to fewer cuts. The only cut made to reduce the MB sample was the cut $m_{\pi\pi} < 364$ MeV. This single cut allowed the MB sample to be reduced to 18 tapes, with roughly the same number of events as the signal sample. The MB sample was later stripped again to obtain a $K_L \to \pi^+\pi^-$ sample, using the relevant cuts from those applied to the Λ normalization sample, since both were two-body hadronic decays. These events were used to measure detector performance and resolution and estimate kaon background. These cuts are shown in Table A.4.

The 18 Λ tapes were processed again, and the events divided into three non-exclusive classes, which were stripped onto separate tapes:

signal: $p_T > 145$ MeV – the high-p_T Λ sample, 49 392 (32 201) events from the He-N_2 (Freon) samples,

target: $\theta_C^2 < 10$ mrad^2 – the low-θ_C^2 Λ normalization set, 44 438 events, and

lambda: $|m_{p\pi} - m_\Lambda| < 2.5$ MeV – the lambda mass set, 168 530 events.

In each step of this processing, every event was also reconstructed as $\overline{\Lambda} \to \pi^+ \bar{p}$, though anti-lambdas are produced much less frequently in the target. This sample of two-body events reconstructing to a $\overline{\Lambda}$ provide a valuable window on background, as these events are almost all assuredly K_{e3}s masquerading as $\overline{\Lambda}$s.

This reduced the data set to seven tapes: one normalization, one signal from each of the He-N_2 and Freon samples, and four of events passing the m_Λ cut.

Using the relevant cuts from the target sample reduction, the minimum bias events were stripped from eighteen to one tape of $K_L \to \pi^+\pi^-$ candidates.

These eight tapes are the sample from which we will extract our signal, derive our normalization, and estimate our background.

Chapter 8

Background

A 'strange coincidence', to use a phrase
By which such things are settled now-a-days.
– Lord Byron

The E888 analysis was done 'blind' – that is, all cuts were made without looking within a predetermined region where the signal was expected to occur. This region was defined by studying the characteristics of H decays and the predominant background processes. The signal events sought were contained in the high-p_T sample. To further narrow the search, cuts must be made to remove background processes which mimic signal. This required a thorough understanding of the characteristics of the decay sought, and of the possible backgrounds.

The defining characteristic of an H in this experiment is the missing p_T ($\not{p}_T$) signature given by the unseen neutral particles in the decays $H \to \Lambda n$ or $H \to \Sigma^0 n$ ($\Sigma^0 \to \Lambda\gamma$). If the H mass is less than the $\Sigma^0 n$ threshold (decaying to Λn only), the identifying characteristic of H decays will be a Jacobian peak in the $\not{p}_T$ spectrum, with a cutoff at the kinematic endpoint. For Hs with mass greater than $\Sigma^0 n$, the spectrum will be less well-defined due to the unseen γ, but still having a cutoff at the kinematic endpoint. The

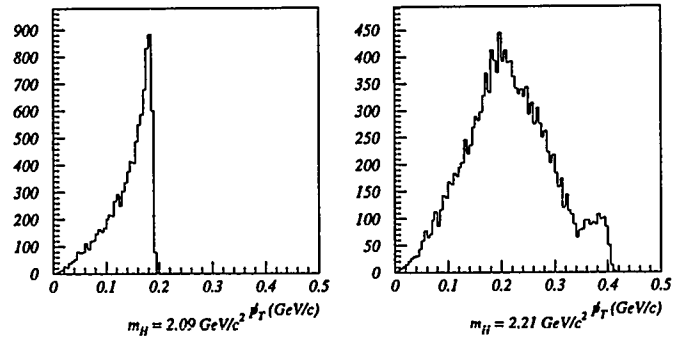

Figure 8.1: $\not{p}_T$ signature of Monte Carlo Hs accepted into the detector below and above the $m_{\Sigma n}$ threshold. The endpoint is smeared because the H decay position is unknown; only the Λ vertex is seen.

relative ratio of $\Sigma^0 n$:Λn is roughly 2:1 above this threshold. Figure 8.1 shows Monte Carlo simulations of these two $\not{p}_T$ spectra. The maximum $\not{p}_T$ of the Λ from the H decay was set by the $2m_\Lambda$ mass threshold at 433 MeV. The minimum $\not{p}_T$ available to this search was set by the backgrounds.

Let us consider the possible background processes. There are three types: Λs with missing p_T from other particles in the beam, kaon decays which have one or both particles misidentified, and secondary neutral beam interactions.

8.1 Backgrounds

8.1.1 Lambda daughters

An obvious background mimicking H decays were particles created in the target which also decayed to a Λ and a neutral. The process $\Xi^0 \to \Lambda\pi^0$

is similar to $H \rightarrow \Lambda n$, producing a Λ with missing-p_T due to the unobserved neutral. This decay sets the lower limit on the $\not{p}_T$ region in which Hs can be identified. The $\not{p}_T$ endpoint of this decay is 135 MeV, corresponding to m_H of 2.074 GeV. The characteristic decay length, $c\tau_\Xi$, for this decay is 8.69 cm, similar to $c\tau_\Lambda$ of 7.89 cm, so a relatively large fraction of these should survive to the decay volume. $\Sigma^0 \rightarrow \Lambda\gamma$ decays are also missing-p_T decays, but are indistinguishable from a target Λ decay, since the decay is electromagnetic, and the γ will be converted in the lead foils downstream of the target. The Λ production cross section used in the normalization includes Λs from Σ^0 production in the target.

8.1.2 Kaons

The most numerous particle decay background was the copious K_L decay. The detector had a larger acceptance for kaons than Λs (5% versus 0.5%), due to the longer lifetime of the kaon; indeed, the detector was originally optimized to study K_L decays. There were three modes of kaon decay to consider:

$K_L \rightarrow \pi^+\pi^-\pi^0$ ($K_{3\pi}$, $\not{p}_{T\,max} = 133$ MeV) – This decay could be reconstructed as an H, as the π^0 from this decay would not be detected, and it was kinematically possible for the π^+ and π^- to have the momentum asymmetry necessary to be reconstructed as m_Λ if the π^+ were misidentified as the proton from a Λ decay. The $\not{p}_T > 135$ MeV cut used to reject $\Xi^0 \rightarrow \Lambda\pi^0$ will reject this decay.

$K_L \rightarrow \pi\mu\bar{\nu}$ ($K_{\mu 3}$, $\not{p}_{T\,max} = 189$ MeV) – This decay could mimic the H if the $\overline{\nu}$ had a large p_T, the π was misidentified as a proton, and the momentum of the μ was low enough that it did not penetrate the MHO or MRG so that

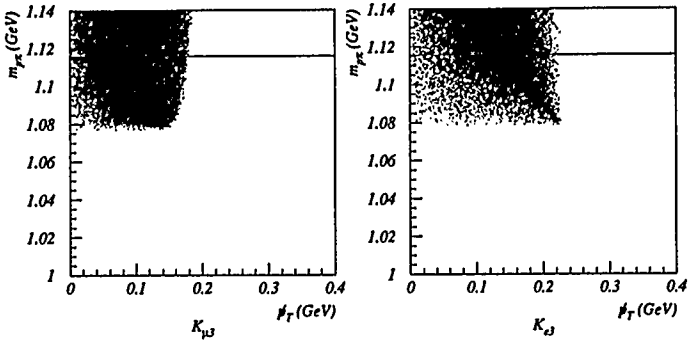

Figure 8.2: Monte Carlo $K_{\ell 3}$ decays reconstructed as $p\pi$ versus $\not{p}_T$. These plots show the region of phase space available to $K_{\ell 3}$s which can mimic Λs. The horizontal line is at 1.11568 GeV, the Λ mass.

it was misidentified as a π. For $K_{\mu 3}$ decays which could reconstruct to the Λ mass, the endpoint of $\not{p}_T$ is 180 MeV. We rely on the MHO and MRG to reject this decay.

$K_L \rightarrow \pi e\bar{\nu}$ (K_{e3}, $\not{p}_{T\,max} = 229$ MeV) – This was the most troublesome kaon decay. Should the pion be misidentified as a proton, and the low momentum electron not trigger the Čerenkov or deposit enough energy in the PbG, the decay could be reconstructed to have m_Λ with high $\not{p}_T$. We studied the lead-glass response carefully to reject these events.

The opposite situation of mistaking the μ or the e for the proton, which at first glance seems more likely because it requires only a single misidentification of the particles, is not likely, because the μ^+ or e^+ must have a high momentum for the event to reconstruct to m_Λ, and it is unlikely that high-momentum electrons will escape both the CER and PbG, or that high-

momentum muons will escape the MHO.

Figure 8.2 shows $m_{p\pi}$ versus $\not{p}_T$ for MC K_{e3}s and $K_{\mu 3}$s (collectively referred to as $K_{\ell 3}$s) reconstructed as Λs. The phase space available to these decays to mimic the Λ if the particles are misidentified, and to have high-p_T is quite limited. The momentum asymmetry necessary for $K_{\ell 3}$s to be near the Λ mass is quite striking; in both cases the lepton momentum must be less than 2 GeV and the pion momentum greater than 3 GeV. Figures 8.3 and 8.4 show the pion and lepton momenta for these decays.

8.1.3 Secondary neutral interactions

The most insidious background of this experiment were lambdas and kaons produced by secondary neutral interactions (SNI) in the collimators, magnets, and vacuum chamber walls of the experiment[1], via associated production:

$$n + N \rightarrow \Lambda + K^0 + X$$

$$K_L + N \rightarrow \Lambda + X.$$

To reject the secondary kaon background, which with the additional apparent $\not{p}_T$ resulting from their production outside the target could mimic a missing p_T Λ, two additional kinematic cuts were made. $K_{3\pi}$s cannot reconstruct with $m_{\pi\pi} > m_K - m_{\pi^0}$, so events with $m_{\pi\pi} < 364$ MeV were cut This turned out to have the additional benefit of cutting $K_{\mu 3}$s: see Figure 8.5. To reject $K_{L,S} \rightarrow \pi^+\pi^-$ decays ($K_{2\pi}$), events with $|m_K - m_{\pi\pi}| < 6$ MeV were

[1]This leads to the question of neutral interactions with the remaining gas molecules in the vacuum decay regions. To study this, at the end of the run the vacuum was spoiled to observe any increase in rate. This is discussed in Section 9.6.

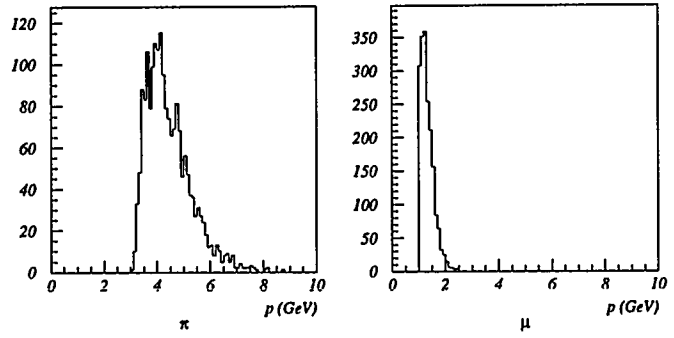

Figure 8.3: Momentum of the pion and muon from MC $K_{\mu 3}$s which, if reconstructed under the mass hypothesis of $p\pi$, were within 2.5 MeV of m_Λ.

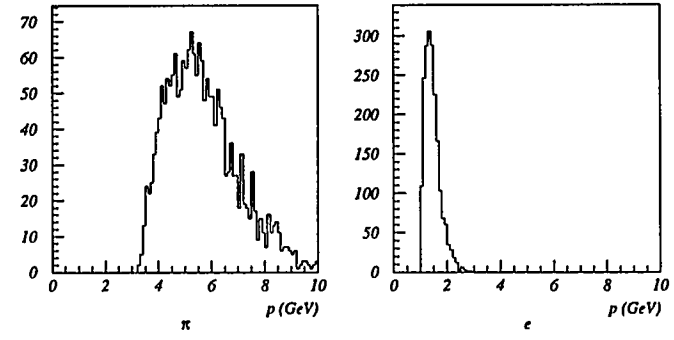

Figure 8.4: Momentum of the pion and electron from MC K_{e3}s which, if reconstructed under the mass hypothesis of $p\pi$, were within 2.5 MeV of m_Λ.

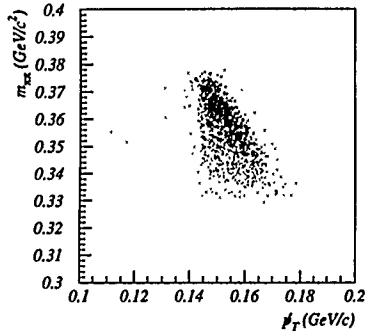

Figure 8.5: Monte Carlo $K_{\mu 3}$s under the mass hypothesis $m_{\pi\pi}$ versus $\not{p}_T$, passing all cuts except particle identification. This figure shows why the cut on $m_{\pi\pi} < 364$ MeV resulted in an effective $\not{p}_T$ cut.

rejected. This cut was also made to reject this decay in the Λ normalization samples.

More troublesome were Λs from SNI. The only way to reject this background was to cut events originating from obvious sources (where Λ production rate was higher than average, presumably from neutral beam scraping), and to require that the Λ decay vertex be far enough from a possible source that the probability that the Λ came from the source was small.

Since every Λ with $\not{p}_T$ – whether from an H created within the target, a $\Xi^0 \rightarrow \Lambda\pi^0$, or a Λ created by a SNI – did not point back to the target, but to some part of the detector upstream of its decay vertex, the first requirement imposed was that the reconstructed Λ vertex be far enough from the nearest possible interaction point that the Λ was very unlikely to have come from there. Since the probability that a particle travels a distance d from its origin without

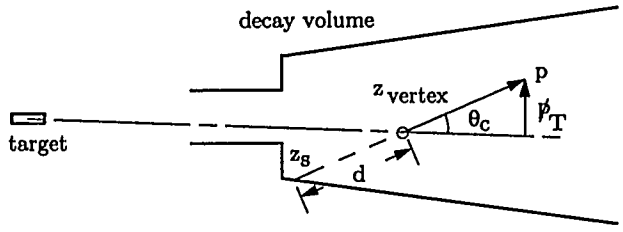

Figure 8.6: Schematic diagram of target and decay volume, showing definitions of collinearity (θ_C), p_T, d/p, and z_s. Not to scale.

decaying is

$$P(d) = e^{-dm/pc\tau} = e^{-t/\gamma\tau} \tag{8.1}$$

the natural measure was the distance of the vertex in number of Λ decay lifetimes (τ_Λ) away from the nearest material in which it could have been created ($N_\tau = t/\gamma\tau_\Lambda$ or equivalently, d/p. For Λs, N_τ is equivalent to 14.1 d/p.). Figure 8.6 shows the quantities defined here.

To find the distance d, the blueprints of the decay volumes, magnets, and collimators were carefully studied and mapped. To determine the point from which a secondary Λ originated, the momentum vector of each Λ was projected backwards to the nearest beamline element. The z-position of this point was referred to as z_s, and was the point from which N_τ was calculated[2].

[2]Note that z_{vertex} was not the same quantity as z_s: the former was the distance of the decay vertex from the target; the latter the z point of the beamline to which the momentum vector passing through z_{vertex} points back. One must also keep in mind that our knowledge of where Λs originate was limited by our knowledge of the beamline – in some sense, Λs seemed to point back to some part of the beamline because that's where we thought the beamline was.

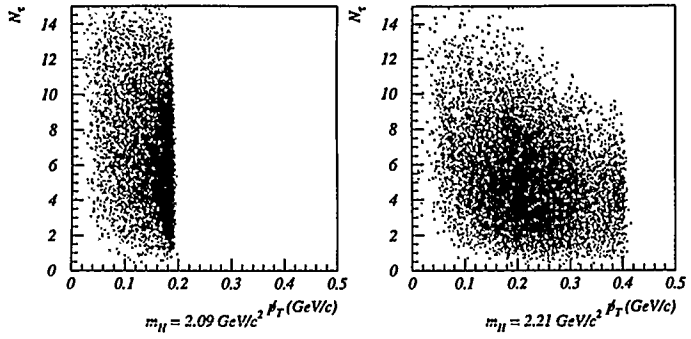

Figure 8.7: N_τ versus $\not{p}_T$ for Monte Carlo Hs.

Valid H candidates have Λ daughters which decay far from any part of the beamline; Λs from SNI appear at small N_τ.

Then N_τ and $\not{p}_T$ are the two parameters which define the signal region. Figure 8.7 shows N_τ versus $\not{p}_T$ of the H for two values of mass and lifetime at either end of the range to which the decay search was sensitive. Figure 8.8 shows N_τ versus $\not{p}_T$ for Monte Carlo $K_{\ell 3}$s reconstructed as Hs. This figure, N_τ versus $\not{p}_T$, for signal and background events, will be our touchstone throughout the H analysis.

The blind signal box was formed by masking out an area with $\not{p}_T > 165$ MeV and $N_\tau > 4.24$ ($d/p = 0.3$). The size of this box was adjusted as the backgrounds were studied, though these limits could only be moved to make the box smaller, never larger. This, then, was the starting point for the analysis. In the following sections, we will discuss the methods used to estimate the background inside the blind signal region and the cuts used to reject background

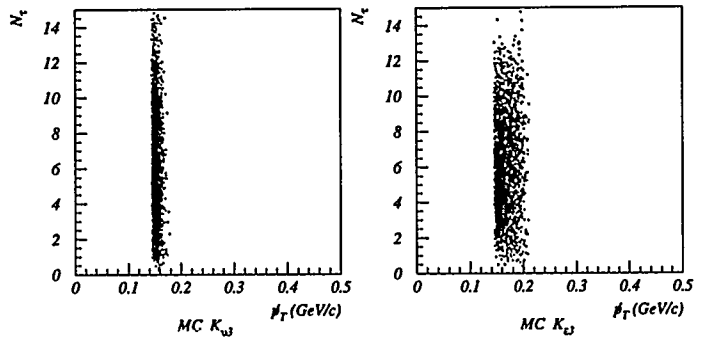

Figure 8.8: N_τ versus $\not{p}_T$ for Monte Carlo $K_{\mu 3}$s and K_{e3}s. The left edge is due to the 145 MeV $\not{p}_T$ cut.

and ensure event quality.

8.2 Background Estimation

To proceed rationally, a measure of profitability must be made for cuts. Given that the analysis was blind, how does one tell if the cuts made were effective in removing background, and not signal sensitivity? There are two avenues of background estimation, both using events passing the signal sample cuts. The first estimates both kaon and SNI background by using similar non-signal events, such as $\overline{\Lambda}$ events, SNI events from an obvious source, and mass sidebands; the second estimates kaon contamination by counting kaon decays in the minimum bias sample.

The other measure of a cut was the loss of sensitivity. Carried to extremes, all events could be cut, removing all background, but with a corresponding loss of sensitivity. The production cross section limit (Equation 5.3)

depends on the ratio of events in the signal box to the number of Λs in the normalization sample after the same cuts are made to each sample. The measure of these cuts is the percentage of the normalization sample of target Λs lost by making the cut. Obviously, this is only relevant for the kinematic, PID, and event quality cuts which were common to both samples. Cuts on quantities such as $\not{p}_T$ and N_τ cannot be made on the target Λ sample. The measure of these cuts was how much H acceptance was lost, and was calculated from Monte Carlo simulations. In this dissertation, the coalescence spectrum ([19], Figure 10.11) was used to obtain the acceptance losses, as it is a more conservative estimate of these losses.

8.2.1 Counting kaons

Background from $K_{\ell 3}$ decays was estimated in several ways:

Method 1

The first was by making the signal cuts to the mass sidebands of the Λ and $\overline{\Lambda}$ signal samples. These must have been almost exclusively $K_{\ell 3}$s, since Λs were unlikely to appear here. The background was estimated by counting the number of events existing within some mass range, and scaling to the mass range within which signal events were accepted.

Method 2

The $\overline{\Lambda}$ sample provided another valuable window into the background. Since very few $\overline{\Lambda}$s were produced in the target, almost all events which reconstructed as $\overline{\Lambda}$ were $K_{\ell 3}$s. By making the signal cuts on the sample of events reconstructing to $\overline{\Lambda}$, the background could be estimated by counting the events

in the identical signal and background regions as the Λ signal sample.

Method 3

The minimum bias sample provides another method of estimating the kaon background. The same cuts used to count target Λs (except for mass cuts) can be made on the minimum bias sample, and the decay $K_L \rightarrow \pi^+\pi^-$ counted. Both Λ and $K_{2\pi}$ decays are two-body hadronic decays. Then the number of $K_{\ell 3}$s that should appear as background was

$$N_K^{bck} = N(K_L \rightarrow \pi^+\pi^-)\frac{\mathrm{Br}(K_L \rightarrow \pi\ell\bar{\nu})}{\mathrm{Br}(K_L \rightarrow \pi^+\pi^-)}\, A_H^K\, \epsilon_{L3}\, \bar{\epsilon}_{PID} \qquad (8.2)$$

where $N(K_L \rightarrow \pi^+\pi^-)$ is the number of $K_L \rightarrow \pi^+\pi^-$ decays passing all relevant cuts (and includes the $K_L \rightarrow \pi^+\pi^-$ acceptance), A_H^K is the acceptance of $K_{\ell 3}$s as Hs, ϵ_{L3} is the efficiency of L3, and $\bar{\epsilon}_{PID}$ is the inefficiency of the particle identification. The L3 efficiency must be included since minimum bias events did not have to pass L3, whereas $K_{\ell 3}$s accepted into the H sample did. The PID inefficiency is included because MC acceptances did not include PID.

Method 4

An independent estimate of kaon background can be obtained by using Equation 5.1, with H replaced by K, detector and particle identification efficiencies taken from Section 10.4, and acceptance calculated from Monte Carlo simulations of $K_{\ell 3}$s mimicking Hs.

Method 5

Another method of estimating $K_{\ell 3}$ background came about because of a second strip done on the data. To show that the Freon sample with no

CER veto had identical $K_{\mu 3}$ background as the He-N_2 sample, this sample was restripped, with all particle identification cuts removed (no CER cuts, no PbG cuts, no $K_{2\pi}$ or $K_{3\pi}$ cuts), but with the requirements that $|m_\Lambda - m_{p\pi}| < 10$ MeV and $\not{p}_T > 145$ MeV. This turned out to be such a useful set of data that we went back and restripped the He-N_2 data with these cuts also. We used this data to estimate the $K_{\ell 3}$ background by applying particle ID cuts in various combinations.

8.2.2 Counting secondary neutral interaction Λ background

To estimate the background from SNI, we chose a region of the detector from which a large number of secondary Λs originated (such as z_s from a flange region), and plotted N_τ versus $\not{p}_T$ for these events; then the number of events within the box and the total number of events from that region were counted. Figure 8.9 shows the definition of each region. The background estimated within the signal box was

$$N_{box}^{est} = \frac{N_{box}^{bck}}{N_{\overline{box}}^{bck}} N_{\overline{box}}^{sig} \tag{8.3}$$

where N_{box}^{bck} is the number of events inside the box from the flange region, $N_{\overline{box}}^{bck}$ is the number outside the box from the flange region, and $N_{\overline{box}}^{sig}$ is the number outside the box from the signal regions ($\overline{box}$ denotes events *not* in the box). For the background reference signal, the events pointing back to $9.36 < z_s < 9.4$ m were chosen (see Figure 9.5). This region was by far the largest source of secondary Λs. This estimation of course undercounted the number of background events from farther upstream; this was taken care of by making a cut on z_s.

These are the characteristics of the H decay sought, and the processes

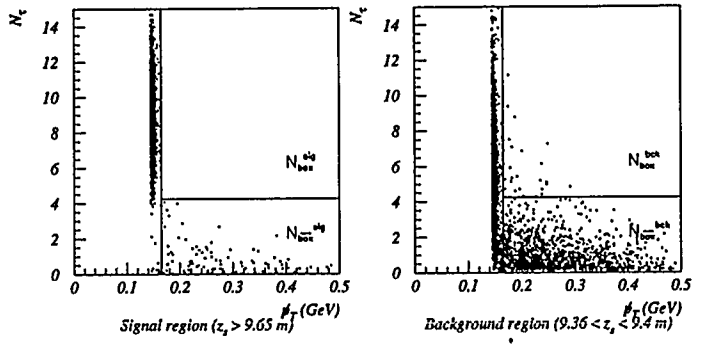

Figure 8.9: Definitions of quantities used to estimate background from SNI inside blind signal box.

which might mimic it. With these in mind, we can proceed to the selection of the H events.

Chapter 9

H selection

Such labour'd nothings, in so strange a style,
Amaze th' unlearn'd, and make the learned smile.
–Alexander Pope

The cuts used to select H's and reject background can be divided into four groups: event quality, fiducial volume, particle identification, and kinematic. The selection of events is described in two stages, corresponding to the method of analysis. First, general cuts were made based on knowledge of the detector from previous E791 analysis; these were the cuts used to reduce the data to from 354 to 18 tapes. The cuts are summarized in Table A.1 under the headings PSL4 and PSL5. Then the cuts specific to the H selection are discussed. These are shown Table A.2 under the heading PSL10. The final cuts cannot be made independent of the background estimates, so discussion of the background estimates are intertwined with the discussion of the final cuts.

9.1 General Cuts

9.1.1 Event quality

Each event was required to be fit by the QT fitter in PSL4 and pass Level 3, so as not to have to calculate the L3 efficiency. Each event was required

to have two tracks of opposite charge. Each track was required to occur within 4 ns of the TSC signal, and to have at least two hits in the TSC.

Each event was required to be reconstructed with errors less than a reasonable amount. The measure of event quality includes the χ^2 of track and vertex reconstruction. These quantities were defined in Section 6.3. In the E791 rare kaon decay analysis, a vertex χ^2 upper limit of 25 was used; track χ^2 of 50. The initial selection of events in this analysis began with these limits.

9.1.2 Fiducial volume

To ensure that events did not traverse fringe or high-mass regions of the detector, several aperture cuts were made. The first of these was to require that the vertex of the event be within the vacuum decay regions, *i.e.*, $z_{vertex} > 9.5$ m (the upstream decay volume started at 9.31 m). This was the point where the fringe fields from the upstream sweeping magnets became negligible. Events whose projected tracks intersected the downstream vacuum window flange were cut. Events which did not intersect the PbG were cut. Each track was required to project through the MHO active area so that muons were guaranteed to encounter this detector (barring multiple scattering).

9.1.3 Particle identification

The next step in reducing the background was to use particle identification information to identify pions and protons and reject electrons and muons. Since K_{e3} decays could not kinematically mimic a Λ decay unless they had the appropriate momentum asymmetry of a high-momentum pion and a low-momentum lepton, during the second half of the experiment the left-side

Čerenkov counter was filled with Freon so that pions from these decays could be vetoed. A first pass of electron and muon rejection was made in the L1 trigger, where a veto was placed on in-time hits from the Čerenkov counters (both sides for the He-N_2 sample, right side only for the Freon sample) and the MHO.

Electrons

To reject electrons, the Čerenkov counters were checked for an in-time hit which was consistent with the particle track as projected by the QT fitter using the drift chambers (*i.e.*, the PMT hit must correspond to the mirror projected to by the particle track).

The other handle on electron and hadron discrimination was the lead-glass calorimeter. Since the lead-glass was 13.8 radiation lengths long, it was very likely that an electron would deposit all its energy in the glass. The hadronic interaction length was 1.21 so that pions and protons typically deposited much less of their energy in the glass. Two criteria were used to reject electrons. The ratio of energy deposited in the calorimeter to spectrometer momentum was one (E/p); the other was the ratio of energy deposited in the converter blocks to the total energy deposited in the calorimeter (E_c/E_T). Figure 9.1 shows these two quantities for minimum bias events. At this stage, events with E/p greater than 70% were rejected.

Muons

Muons were identified by a signal in the MHO. Located downstream of the lead-glass and almost a meter of iron (a total of 5.43 hadronic interaction

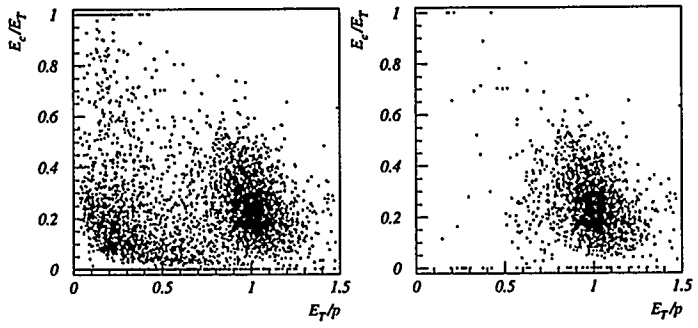

Figure 9.1: Lead glass response to minimum bias events. *Left:* MB events selected with only a MHO veto. There are two quite distinctive bands of events. *Right:* The same MB events selected with the requirement that one side have a CER hit and the other be quiet – the remaining events are electrons.

lengths), primarily only muons gave a signal in this detector. To reject these, any track with a MHO x and y view hit within 4 ns of the TSC time and within 4 ns of each other and consistent with the scintillator that the track pointed to caused the event to be discarded.

A small fraction of hadrons survived the lead-glass and iron, so the MRG was used to further discriminate muons and hadrons. If the MRG was hit, the point at which a particle stopped in the MRG was compared to the distance that a minimum-ionizing particle of that momentum should have traveled in the aluminum/marble stack. If this difference was less than 3.5 gaps (each gap being a 10% energy decrement), *i.e.*, if the track had greater than 65% of the expected range of a muon of that energy, the particle was identified as a muon. Hadrons which survived the iron filter would shower in the MRG stack and stop shorter than a muon of the same energy. Figure 8.3 shows the momenta

of the pion and muon for $K_{\mu 3}$ decays which reconstruct to m_Λ. Muons with less than about 1.6 GeV would not survive the iron hadron filter.

9.1.4 Kinematic

Before a particle could be accepted as a Λ decay, several kinematic cuts were made. The first was an event quality cut: each track must have $p > 1$ GeV. This requirement eliminated low acceptance tracks for which PID was not well-understood.

Since a small portion of the phase space of $K_{2\pi}$ and $K_{3\pi}$ could have their mass reconstructed to m_Λ if the tracks were misidentified as $p\pi$ from a Λ decay, two cuts were made to reject these events. If $m_{\pi\pi} < 364$ GeV ($m_K - m_{\pi^0}$), then the event was cut to reject $K_{3\pi}$. This mass cut costs from 2-13% ($m_H =$ 2.21-2.09 GeV) in H acceptance. If $\mid m_K - m_{\pi\pi} \mid < 6$ MeV, the event was cut to reject $K_S \rightarrow \pi^+\pi^-$ resulting from secondary interactions. The detector energy resolution for $K_{2\pi}$ was 1.5 MeV, so this cut was 4σ away from the peak. This cut cost 0.2-2.6% ($m_H = 2.09$-2.21 GeV) in H acceptance.

The reconstructed mass $m_{p\pi}$ was required to be within 2.5 MeV of the Λ mass. The σ of the normalization Λ mass peak was 0.55 MeV (Figure 10.2), (this was smaller than the $K_{2\pi}$ mass peak because $\Lambda \rightarrow p\pi^-$ has very little excess kinetic energy to impart to the decay).

Having now selected a sample of $\not{p}_T$ events based on the event quality standards previously determined by E791 and kinematic background cuts, the final cuts on the data were made after studying the backgrounds outside the signal box. These are the so-called *tight* cuts.

9.2 Tight Cuts

9.2.1 Fiducial volume

Hot spots

Since a significant background was Λs caused by secondary neutral interactions in the beamline, we looked to see if there were any points in the upstream collimating and sweeping regions which had an anomalous number of Λs emanating from them. This was done by finding Λs whose reconstructed momentum vectors when followed upstream converged at a distinctive point. If many Λs pointed back to a particular spot, we assumed the Λs originated there, and excised them. Note that this exercise differs slightly from finding z_s. There, we were trying to find the point farthest downstream from which the Λ could have originated, and therefore the smallest N_τ; here, we were trying to locate places where many secondary interactions occur.

There were three z positions to which Λs appeared to converge: the collimator widening at $z = 8.3$ m, the flange coupling the collimator to the upstream decay volume at 9.3 m, and a small spot at 11 m. Figure 9.2 shows the x-y distribution of events at these positions. Figure 9.3 is a set of snapshots showing the focusing of the events at 11 m in z. Not all Λs which point back to these positions should be cut. One would expect a uniform distribution in x and y for a random distribution of high-$\not{p}_T$ Λs, so the hot spots are those areas where the number of Λs pointing back to that spot are greater than average. Any Λs which projected back to these points were cut in PSL10.

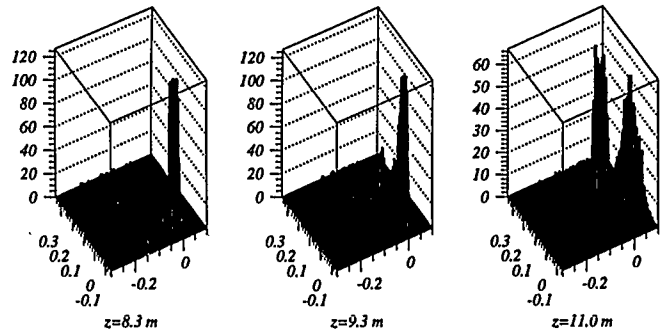

Figure 9.2: x-y distribution of projected Λ intersections with the decay volume at three z points where hot spots were found. Noticeable peaks at sources can be seen. Events from the source at 8.3 m show up in all three plots, but the angular distribution of the apparent source diverges when viewed from downstream.

Secondary Λs

Figure 3.4 shows the layout of the beamline in the region of interest. Figure 9.4 shows the collimators and decay volumes as they are mapped by the intersection of backward projection of the Λ momentum vector and the decay volume. Figure 9.5 shows the N_T versus z_s distribution of events from the signal sample. The regions below $z_s < 9.65$ m show obvious signatures of Λs created by secondary neutral interactions, while for $z_s > 9.65$ m there were few events at low N_T. Much of the background can be cut by requiring that $9.65 < z_s < 13$ m. This cut cost 67-71% (m_H = 2.09-2.21 GeV) in H acceptance (based on the coalescence H momentum spectrum – the central spectrum shows a loss of 53% at 2.15 GeV). This cut caused a regrettable loss of acceptance, but it was unavoidable.

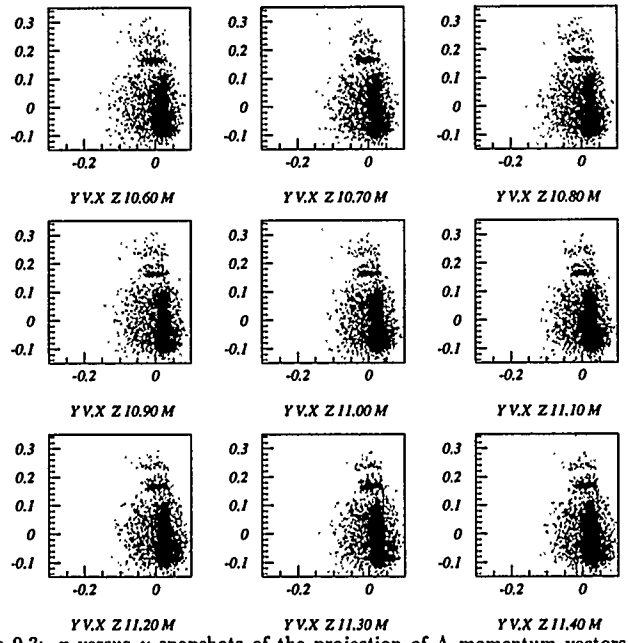

Figure 9.3: x versus y snapshots of the projection of Λ momentum vectors to specific z positions. This series of scatter plots shows the focusing of the projection at 11 m (the small horizontal spot at $y_s \simeq 1.5$).

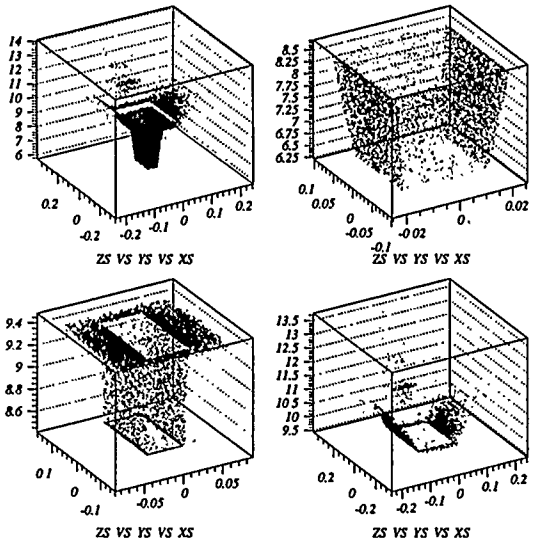

Figure 9.4: Collimators and decay volumes of E888 detector as mapped by projected Λs. The upper left figure is the total volume from which decays were accepted; the three other figures are subdivided into z regions of interest.

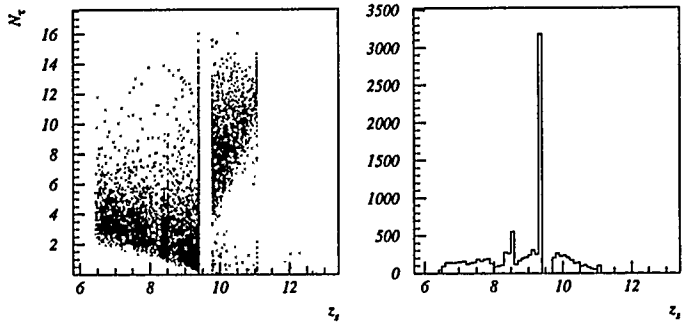

Figure 9.5: Distribution of signal events versus z_s and N_τ. The area with few events at low z_s and low N_τ is due to the lack of acceptance in this area. The signal region is those events with z_s greater than 9.65 m, where there are few events at low N_τ. There is an obvious source at $z_s \sim 9.4$ m; this is the region used to estimate background from SNIs.

9.2.2 Event quality

After the z_s cut, most of the background disappeared, but there were still a few events near the boundaries of the box, both in N_τ and $\not{p}_T$. In the $\overline{\Lambda}$ sample, there were events inside the box. These events were dumped and their kinematic and reconstruction characteristics studied to determine what parameters could be used to excise these events (and their invisible counterparts inside the box). After looking at these dumps, several parameters were identified which allow further reduction of the background. These are track χ^2, vertex χ^2, and the number of hits used in the QT fit.

Several of these boundary events had relatively high vertex and track χ^2s. Figures 9.6 and 9.7 show the vertex χ^2 and track χ^2 before the tight cuts. These parameters were tightened to 5 and 15 without cutting into the peak

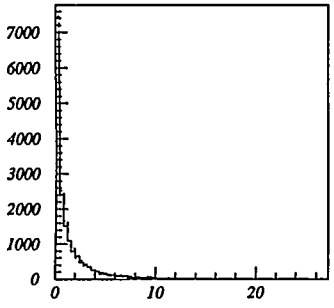

Figure 9.6: QT vertex χ^2 of the target Λ sample, before the tight cuts. The MC distribution (dashed line), normalized to the same number of events, is superimposed.

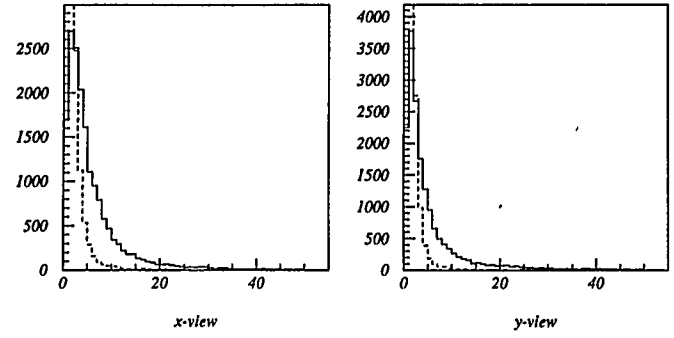

Figure 9.7: x- and y-view track QT χ^2s of the target Λ sample, before the tight cuts. The Monte Carlo distributions (dashed line), normalized to the same number of events, are superimposed. The data distribution is thought to be wider than the MC because of uncertainties in the magnetic field maps to which the MC events were not subject.

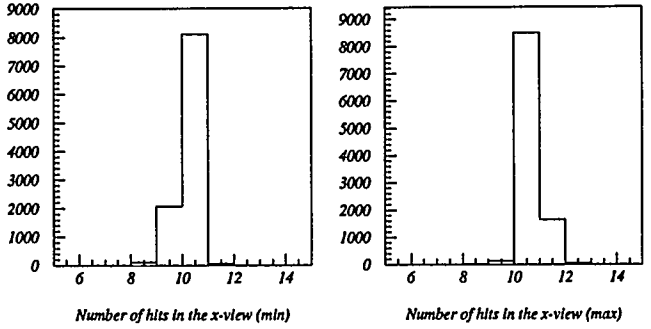

Figure 9.8: Number of hits used by the fitter to fit the track in the x-view. *Min/Max* was the minimum/maximum number of hits used in either the left or right track.

of the distribution. This cut 12.4% and 7.1% of the normalization sample, respectively.

The QT fitter fit tracks to the hits in the drift chambers. There were 10 planes of wires in each view (x and y) of each arm of the detector, and each plane could have more than one hit for a track. The optimal number of hits that the fitter should use was 10; more implied noise or accidental hits, fewer, a less-than-ideal reconstruction of the track due to L/R track ambiguities. Looking at the dumped events, several of the tracks had anomalous numbers of hits in the x-view (the view in which the magnets bend the tracks). Figure 9.8 shows the distribution of hits in the x-view. Requiring that each track have 9, 10, or 11 hits cut 2.05% of the normalization sample.

9.2.3 Electron particle identification

After making these cuts, the N_τ versus $\not{p}_T$ plot was examined again for events near the signal boundary. Equation 8.3 estimated a background of 0.305 (0.349) events inside the signal box for He-N_2 (Freon). Again, remaining events near the boundary and events inside the $\overline{\Lambda}$ box were dumped and studied. It appeared that many of these events were K_{e3}s with a soft electron track that just missed being cut by the $E/p > .60$ cut. To get rid of these events, we required that events with $p < 2$ GeV have $E/p < 0.52$. This cut 0.3% of the normalization sample.

Unfortunately, K_{e3} decays which mimicked Λ decays had soft right-side electrons for the same reason that Λ decays had soft right-side pions, and the CER was inefficient[1] for low momentum electrons. Figure 8.4 shows the momenta of the pion and electron for K_{e3} decays which reconstruct to m_Λ.

The CER inefficiency was measured by selecting events from $K_L \rightarrow \pi e \bar{\nu}$ decays in the minimum bias sample using the following stringent electron *selection* criteria:

- $E/p|_{L,R} > 0.65$
- $E/p|_{R,L} < 0.65$
- $\frac{E_c}{E_T}\Big|_{L,R}$ above contour cut
- $\frac{E_c}{E_T}\Big|_{R,L}$ below contour cut
- no MHO hits.

[1] I use inefficiency as the figure of merit here, because we wish to know how many electrons we failed to reject, rather than how efficient we were in selecting them.

Then, for each electron thus identified by the PbG, the CER was checked for a hit. The inefficiency was defined as the number of electrons meeting the PbG electron selection requirements not having a CER hit, divided by the number of electrons identified by the PbG. Figure 9.9 shows the CER inefficiency versus momentum. We obtain a single number for CER inefficiency by multiplying the inefficiency momentum spectrum by the momentum spectrum of electrons from MC K_{e3}s which pass all the H signal cuts barring PID (Figure 8.4). The CER was not very effective at these low momenta, and was 65% inefficient, that is, only 35% of electrons from K_{e3}s mimicking Λs were rejected by the CER.

To measure PbG electron rejection inefficiency, a hit was required in one side of the CER with the momentum of the track less than the pion Čerenkov threshold, no hit in the other side, and no MHO hits. Then the inefficiency of the PbG was defined as the number of events triggering the CER but not triggering any of the PbG cuts, divided by the number of events triggering the CER. Figure 9.9 shows the PbG inefficiency with the final PbG cuts made, the remainder of which are discussed below. With all the PbG cuts in place, the PbG was 1.1% inefficient.

9.2.4 Kinematic

Signal box size

Figure 9.10 shows the He-N_2 and Freon signal sample distributions for the analysis at this stage. At this point, the background estimated was 0.238 (0.210) in the He-N_2 (Freon) sample. The probability of observing no events in the signal box was $e^{-0.238}e^{-0.210} = 0.64$, for a 36% chance of seeing a background

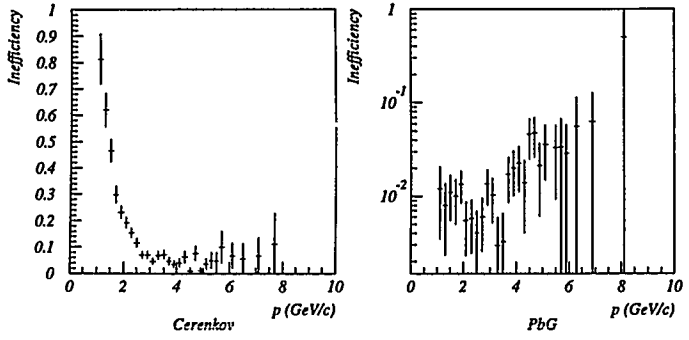

Figure 9.9: Electron rejection inefficiencies of Čerenkov counter and lead-glass calorimeter versus momentum.

event inside this signal box. This was still a higher than one would like, so we used the only remaining variables and narrowed the signal box to cut events with $N_\tau < 5$ and $\not{p}_T < 174$ MeV. This reduced the background estimate to 0.1221 (0.1026) for He-N_2 (Freon), giving a 20% probability of finding one background event in the signal box. Because the $\not{p}_T$ of the H is determined by the H mass, the $\not{p}_T$ cut also limited the H mass range to which this search was sensitive to $m_H > 2.085$ GeV. No events were found in the newly visibly region. This cut cost between 19-29% ($m_H = 2.21$-2.09 GeV) in H acceptance.

9.3 Opening the Box

Having determined that the probability of finding background inside the signal box was acceptably low, we opened the box. We found three candidate events in the He-N_2 signal box and no events in the Freon signal box. The He-N_2 events had large N_τ and approximately the same $\not{p}_T$ of 190 MeV, which

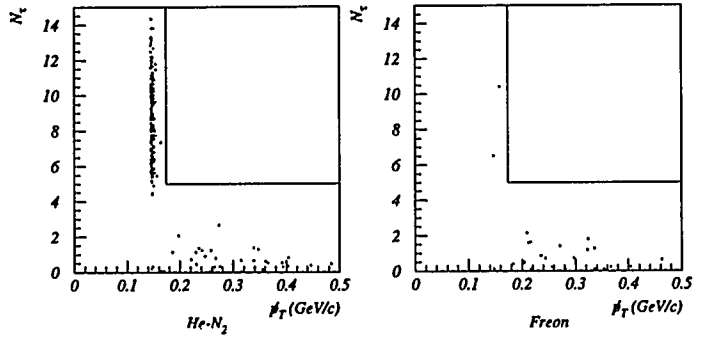

Figure 9.10: The signal region before opening the box. All cuts have been made. The prominent band in the He-N_2 sample are $K_{\mu 3}$s. The left edge is due to the $\not{p}_T > 145$ MeV requirement; the right edge is the kinematic limit of $K_{\mu 3}$s passing the $m_{\pi\pi} < 364$ MeV cut. There is no band in the Freon sample because the pion from these decays was vetoed by the left Čerenkov counter.

was indeed the signature one would expect from an H. These events were also kinematically consistent with K_{e3}s.

At this point, we realized that we had no independent estimate of K_{e3} background from the signal sample. We decided – before knowing any characteristics of the candidates other than N_τ and $\not{p}_T$ – to repeat the analysis for events in the sidebands of the Λ and $\overline{\Lambda}$ mass peaks ($m_\Lambda \pm 4 < m_{p\pi} < m_\Lambda \pm 14.5$ MeV). Events in the mass sideband passing signal cuts must be K_{e3}s, since $K_{\mu 3}$s were rejected by the $K_{3\pi}$ and $\not{p}_T$ cuts and secondary Λs cannot be in the mass sideband. Four events passing all analysis cuts were found in the sidebands. This gave background estimate of $4 \times \frac{0.0025}{0.0105} = 0.95$ event. Upon further study, it became clear that these events were K_{e3}s: one event had a high E/p of 0.64, while the other three had high E_c/E_T. We decided to

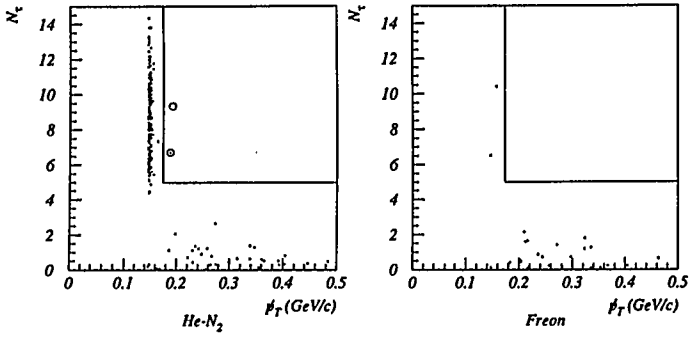

Figure 9.11: The final N_τ versus $\not{p}_T$ distributions. The candidate events found within the blind signal box are highlighted with circles. The signal region is demarcated by the solid lines.

eliminate this background by requiring that $E/p < 0.60$ and $E_c/E_T|_R < 0.66$ (the stiff left track cannot be an electron because it is unlikely that a hard electron will have low E/p). The normalization loss of these cuts was 6.2% and 8.5%, respectively. These cuts removed all the Λ sideband signal events. Applied to the $\overline{\Lambda}$ mass sideband sample, these cuts removed all but two events. Based on the result of no events in the Λ mass sidebands, and two in the $\overline{\Lambda}$ sidebands, we estimated a background of less than $2 \times \frac{0.0025}{0.0210} \simeq 0.24$ events from K_{e3} decays.

Applying these cuts to the signal sample removed one of the candidate events, leaving two. We take these two events as our final candidates. Figure 9.11 shows the final sample.

To summarize, the final PbG cuts applied were $E/p > 0.60$ ($E/p > 0.52$) for $p > 2$ ($p < 2$) GeV, and $E_c/E_T|_R > 0.66$. With these cuts, the PbG was

98.9% efficient in rejecting electrons (Figure 9.9). A summary of all cuts made to the signal sample is shown in Table A.2 under PSL10. With these cuts, the background from secondary neutral interactions was estimated to be 0.087 (0.064) He-N_2 (Freon), for a total SNI background of 0.15 event.

9.4 Re-analysis without Particle Identification

It was suspicious that both candidates occurred in the He-N_2 sample, where backgrounds from $K_{\ell 3}$s were expected to be higher, while the Freon sample was clean.

If the He-N_2 and Freon data were taken to be sufficiently distinct samples due to the differences in the detector, trigger, and software configurations that one could say two different experiments had been conducted, then it would be reasonable to argue that the results of the Freon experiment at the 90% C.L. rule out those of the He-N_2 experiment, and that the He-N_2 experiment could be regarded as background limited.

If a limit were based on the Freon data only, the limit would be slightly lower than that gotten using the full data set with two events ($\sim 2 \times 2.3\times$ the single event sensitivity (SES) versus $5.32 \times SES$ using the full data set; the factor of 2 is due to the decrease in sensitivity by using 1/2 the data set). Can the two data sets be regarded as the results of two different experiments?

The Freon sample had less background because $K_{\ell 3}$s which had the necessary momentum imbalance to reconstruct as a Λ had a high momentum left-side pion, which was vetoed by the Freon-filled left-side CER counter (this is why the distinctive $K_{\mu 3}$ band does not appear in the Freon N_τ versus $\not{p}_T$

plots). The L1 trigger for these runs had a CER veto on the right-side only, and the left-side CER rejection was made in PSL4. If this software veto were removed, the Freon sample should then resemble the He-N_2 sample, and if the Freon CER veto were rejecting K_{e3} events within the signal box, these would then reappear.

To check this, the data was re-analyzed without the offline particle ID, including the left-side CER veto (the L1 vetoes on the MHO and right-side CER cannot be removed). Figure 9.12 shows the Freon sample without the left-side CER veto, but with all other cuts. Though the $K_{\mu 3}$ band reappears, indicating that the CER veto was indeed working as expected, no additional events were found within the signal region. This is one more strike against the two candidates being K_{e3}s. Since the left-side CER Freon veto did not seem to be rejecting similar background events within the signal region, the appearance of two candidates in the He-N_2 sample and none in the Freon sample can only be attributed to random chance and not the detector/trigger/software configuration. Thus there is no justification for using only the Freon sample to set the limit.

9.5 Other Background Estimates

Since K_{e3}s were the kaon decay of most interest, can we estimate by other means how many should have been observed in the signal sample? The estimates used above corresponds to Methods 1 and 2 discussed in Section 8.2.1. Let us consider the remaining methods.

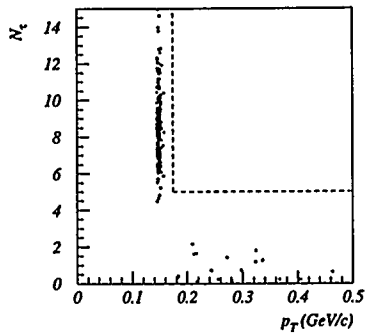

Figure 9.12: Freon data re-analyzed without the left-side Čerenkov veto. The distinctive $K_{\mu 3}$ band reappears, but no additional candidates in the signal region were found.

Method 3

By counting $K_L \rightarrow \pi^+\pi^-$ decays from the minimum bias sample, and multiplying by the appropriate minimum bias prescale factors, we find that 7.86×10^5 $K_{2\pi}$ decays were accepted into the detector. Taking the L3 efficiency as 85% (from E791 measurements), the PbG inefficiency as 1.1%, and the CER inefficiency for low momentum electrons as 65% and substituting these numbers into Equation 8.2, the number of K_{e3} decays expected to appear in the signal region and escape PID rejection was 1.7 events.

Method 4

Using Equation 5.1, substituting K for H and taking the beam intensity and detector efficiencies from Section 10.5, production cross section and probability of decay from MC simulations using the Skubic parameters, and ac-

ceptance for kaons of K_{e3} decays passing all H cuts except PID (1.84×10^{-6}) multiplied by the branching ratio of $K_L \rightarrow \pi e \bar{\nu}$ (39%)

$$N_K^{pred} = (0.748)(2 \times 10^{16}) \left(\frac{(112)(65 \times 10^{-6})}{801} \right) (4.8 \times 10^{-2})(1.84 \times 10^{-6})(0.39)(0.65)(0.80)(0.6) \quad (9.1)$$

which gives ~ 1460 K_{e3}s in the signal region before PID. All of these decays had low momentum electrons on the right side. Multiplying the number of decays by the probability that PID would not reject the decay ((0.011)(0.65)) leaves ~ 10 background events in the signal box. We have reason to think that the magnitude of the kaon production cross section is smaller than that given by the Skubic parameterization (though the shape and therefore the acceptance is the same) so if we further correct by a factor of 366/827 (the factor by which the Abe Λ production cross section was smaller than Skubic – see Section 10.2.1), the number of K_{e3}s estimated to survive in the signal region was ~ 4.5.

Of these two estimates, the first is more reliable. It relies only on counting a well-understood decay mode, scaling by the appropriate branching ratios, and the Monte Carlo acceptance. Its worst uncertainty is in the estimate of L3 efficiency. The second estimate relies on many not-well-understood estimates of beam intensities and detector efficiencies, and absolute magnitude of the kaon production cross section (something which we have reason to doubt we know very well); still, it is reassuring that the two matched this closely. However, both disagree with the background estimate of fewer than 0.24 K_{e3} events obtained from studying the mass sidebands of actual data.

Method 5

The re-analysis of data without the offline particle identification cuts discussed above resulted in a serendipitous method of independently estimating K_{e3} backgrounds. Since few particle ID cuts were made on this sample, it can be studied to determine the background.

A sample of minimum bias events was selected by requiring a CER hit on one side, and no CER hit on the other, and that the events pass all other signal cuts except PbG and the m_Λ cut (which would cut nearly all the events). Instead, events within 5 MeV of the m_Λ were cut to exclude any Λs in the MB sample, and to obtain a similar asymmetry to that of Λs, the momentum of the right side track was required to be less than 3 GeV. The remaining events were almost all K_{e3}s.

From this sample, the number of events which passed the signal PbG cuts was counted. Call this number b, the number of K_{e3}s which would not be rejected by the PbG signal cuts (Section 9.3). Then let B be the number of events also from this MB sample which pass all signal cuts except the PbG cuts and have $E/p > 0.8$ on the side of the CER hit. We thus have the number of MB K_{e3}s which have $E/p > 0.8$, and the number of MB K_{e3}s which pass the PbG signal cuts, but are similar to events in the signal sample. The requirement that $E/p > 0.8$ and the CER criteria used to select the MB K_{e3}s are individually sufficient to select electrons; we can now use the former criteria alone on the signal sample to count the number of K_{e3}s in the signal sample, and estimate the number of K_{e3}s in the signal region.

Let S be the number of events in the signal sample which passed all cuts

except the PbG signal cuts and have $E/p > 0.8$ on the side of the CER hit. These are K_{e3}s. Then the number of K_{e3}s in the signal sample one would expect to pass the PbG cuts was $(b/B) \times S$. We found $b = 0$, $B = 625$, $S = 128$, so the background expected from K_{e3}s which pass the PbG cuts in the signal sample is less than $1 \times \frac{128}{625} \simeq 0.21$, which agrees with the measurement made from the mass sidebands.

This estimate of background is attractive because it was made independently of any cuts made to the data sample. While the resulting estimate is similar to that gotten by studying the Λ and $\overline{\Lambda}$ mass sidebands, the events from the mass sidebands were used to determine the final set of PbG cuts, and are therefore biased. The estimate of Method 5 is unbiased.

The final kaon background measurements will be taken from Methods 1, 2, and 5, as these are based on measurements from data, while the results of Methods 3 and 4, while useful as checks, require too many estimates of detector performance and beam quality.

9.6 Background from Secondary Neutral Interactions in Gas

To estimate the background from secondary neutral interactions with residual gas molecules in the vacuum decay region, the vacuum was spoiled from 3×10^{-4} to 8×10^{-1} torr for 1% of the data. A single signal event in this sample indicated that the background in the rest of the data due to interactions with residual gas molecules in the vacuum decay region is less than $99 \times 1 \times \frac{3 \times 10^{-4}}{8 \times 10^{-1}} \simeq 0.04$ event.

Chapter 10

Normalization

The note I wanted; that of the strange and sinister embroidered on the very type of the normal and easy.
–Henry James

Now that the final set of cuts on the signal sample have been obtained, these cuts, where appropriate, can be applied to the target Λ sample, and the number of normalization Λs observed found. Then the remainder of the terms in Equation 5.3 can be defined and measured based on these cuts.

10.1 Counting Target Lambdas

The 'target' Λ sample was the set of events decaying to $p\pi^-$ with collinearity[1] squared (θ_C^2) less than 10×10^{-6} rad^2, and surviving the other cuts listed in Table A.1 under PSL5. These Λs were then required to pass the same cuts as the final H signal sample (PSL10), excepting the p_T, d/p, and z_s signal cuts. They were instead required to pass a tighter collinearity cut of 1.5×10^{-6} rad^2. Figures 10.1 and 10.2 show mass and collinearity after all the tight cuts except the mass and θ_C^2 cuts. The final target Λ cuts are shown in

[1] Collinearity is defined as the angle between the reconstructed total momentum vector of the decaying particle and a line passing through the reconstructed decay vertex and the center of the target. See Figure 8.6.

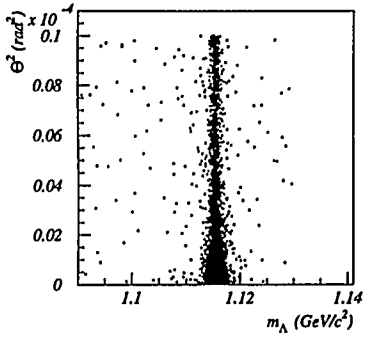

Figure 10.1: θ_C^2 versus mass of the target Λ sample, with all cuts except mass and collinearity.

Table A.3 under PSL9.

After all cuts are made to the target Λ sample, 20 433 target Λs were observed (N_Λ^{obs}, 10 590 from the He-N sample (runs 30268 and earlier), 9 843 from the Freon sample (runs 30269 and up). The gas in the left Čerenkov counter was changed from He-N_2 to Freon over a period of about 20 runs, beginning at 30252; 30268/9 was a nominal division between the two data sets.

10.2 Acceptance

The definition of acceptance is an important concept in the analysis that follows. To minimize the computation time of the Monte Carlo, events were generated only within a 100 μsr beam angle, decaying between the z limits of 9 m $\leq z \leq$ 18 m, and with a momentum spectrum $\mathcal{P}(p)$ between 5-20 GeV (p_L and p_H). The z limits were roughly defined by the endpoints of the vacuum

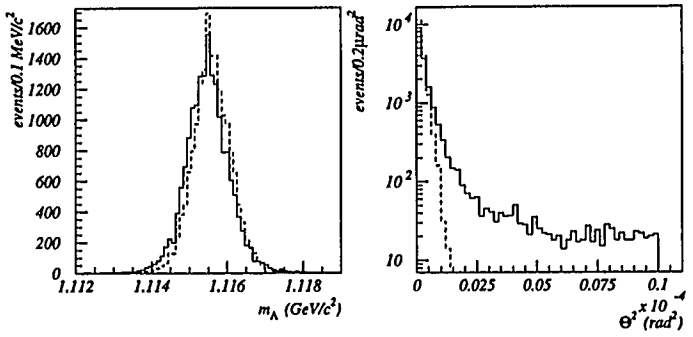

Figure 10.2: *Left:* Target Λ mass peak after the tight cuts of PSL9 (except for mass). The final mass cut was $|m_\Lambda - m_{p\pi}| < 2.5$ MeV. *Right:* Target Λ θ_C^2 after the tight cuts of PSL9 (except for θ_C^2). The initial θ_C^2 selection cut was 10×10^{-6} and the final cut was at 1.5×10^{-6} rad^2. Also shown in each plot is the equivalent MC data (dashed line). The plots have been normalized so that the number of MC and data events are the same.

decay region (VDR); the upper momentum limit comes from kinematic limits of particle production in a 24 GeV beam, the lower limit from the fact that particles with lower momentum are not likely to survive to decay within the VDR (see Figure 10.6 and Figure 10.10). So acceptance is defined as

$$A \equiv \frac{\text{number of events which pass all cuts}}{\text{number of events generated in 100 } \mu\text{sr with } \mathcal{P}(p) \text{ which decay in } \Delta z}$$

or mathematically

$$A = \int_{p_L}^{p_H} \alpha(p)\mathcal{P}(p)(e^{-z_1 m/pc\tau} - e^{-z_2 m/pc\tau})\, dp \qquad (10.1)$$

where $\mathcal{P}(p) \equiv$ the probability that a particle has momentum p at the target; $\mathcal{P}(p)(e^{-z_1 m/pc\tau} - e^{-z_2 m/pc\tau})$ is then the momentum spectrum in the decay

volume, and

$$\alpha(p) \equiv \frac{\text{number of events with momentum } p \text{ passing all cuts}}{\text{number of events generated in the VDR with momentum } p}. \quad (10.2)$$

$\alpha(p)$ is the probability that a particle having momentum p in the VDR made it through the detector and survived all the cuts. Stated another way, this is the acceptance as a function of momentum only.

Since the Monte Carlo created events into a 100 μsr beam angle (for historical reasons), and the detector collimators had a 65 μsr opening, a beam size correction factor $\beta^A = 0.65$ must be applied to the acceptance when calculating N_H^{pred} or N_Λ^{pred}.

10.2.1 Production

In order to determine the acceptance of target Λs, the inclusive momentum spectrum of Λs from $p + \text{Cu} \rightarrow \Lambda + X$ must be known. There are three experimental results which are most relevant to this experiment. Beretvas *et al.* [75] measured Λ production at 400 GeV and angles of less than 10 mrad and fit their data in terms of the Skubic *et al.* parameterization [76]. This parameterization has long been used by E791 for MC kaon generation, and is coded into the offline, so was most convenient to use, and well-understood. Abe *et al.* [77, 78] measured Λ production at 12 GeV and angles of 61 mrad (3.5°) and greater. Blobel *et al.* [79] measured the $p + p \rightarrow \Lambda + X$ in a bubble chamber experiment at 24 GeV. None of these experiments precisely matched the characteristics of the E888 (Table 10.1); it ran at 24 GeV and 48 mrad (2.75°). All have their advantages and disadvantages, so each was studied to determine the best possible match.

	E (GeV)	Angle (mrad)	$\sqrt{s}$ (GeV)	p_T (GeV)	x_F
E888	24	48	6.84	0.24-1.05	0.07-0.85
Beretvas	400	0.0-9.8	27.43	0.0-4.92	0.212-0.962
Abe	12	61-166	4.93	0.25-1.71	0.23-0.82
Blobel	24	na	6.84	0.075-1.0	0-1.0

Table 10.1: Comparison of kinematic variables of E888 and the Beretvas, Abe, and Blobel Λ production experiments.

To reconstruct a Λ momentum spectrum from E888 target Λ data which could be compared to the spectra from the other experiments, MC Λs with a flat momentum spectrum in the VDR were generated. The number of these Λs accepted was divided by the number created, per momentum bin, and thus the acceptance of the detector as a function of momentum only was found. This was multiplied by the observed Λ momentum spectrum from data to find the original spectrum of the Λs which decayed in the VDR:

$$N^{observed}(p) = \frac{N^{det}}{\alpha_\Lambda} = \frac{N^{det}(p) N^{flat}(p)}{N^{acc}(p)}. \quad (10.3)$$

$N^{det}(p)$ is the spectrum of Λs from the target data as seen in the detector, $N^{flat}(p)$ is the number of MC Λs generated with a flat momentum spectrum in the VDR, $N^{acc}(p)$ is the spectrum of these MC Λs passing all the cuts, and $N^{observed}(p)$ is the spectrum of Λs which decay in the VDR, each as a function of momentum. α_Λ is then the same acceptance defined in Equation 10.2. $N^{observed}(p)$ can be compared to the other spectrum of Λs as they appear when decaying in the VDR. $N^{observed}(p)$ is the target Λ production spectrum weighted by the probability that a Λ of that momentum will decay in the VDR, but rather than deconvolving the probability, we will apply the probability function to the other proposed Λ spectra and compare those.

	Beretvas	Abe	Blobel
C_1	3.44	1.91	-1.71
C_2	1.96	1.45	-5.42
C_3	-1.79	-2.45	7.51
C_4	-0.92	-4.23	-3.40
C_5	-2.21	-1.115	-0.88
C_6	0.31	-0.024	-4.83
C_7	-0.023	-0.039	3.12
C_8	0.99	1.60	0.91
C_9	0.12	0.021	-0.76

Table 10.2: Coefficients of the fits of Beretvas, Abe, and Blobel data to the Skubic parameterization.

Beretvas

Skubic parameterized the invariant cross section of strange particle production (based on Regge pole theory) as

$$E\frac{d\sigma}{dp^3} = \frac{E}{p^2}\frac{d^3\sigma}{d\Omega dp} = \frac{E^*}{\pi p^*_{\parallel max}}\frac{d^2\sigma}{dx{dp_T}^2} = f(x,p_T)$$

$$= \exp(C_1 + C_2x^2 + C_3x + C_4xp_T + C_5p_T^2 + C_6p_T^4 + C_7p_T^6)(1-x)^{C_8+C_9p_T^2} \quad (10.4)$$

where here p_T is the transverse momentum of the produced particles with respect to the incident beam, and Feynman $x_F = p^*_{\parallel}/p^*_{\parallel max}$ (the * denotes center-of-mass variables). Beretvas *et al.* fit their measured data to this parameterization and found the coefficients for Λ production by protons on a copper target. These are listed in Table 10.2.

Abe

Abe *et al.* measured the Λ production spectrum at energies and angles nearer that of E888. The Skubic parameterization allowed us to insert a different set of energies and angles, and then compare the Beretvas fit to the Abe data. Using the relevant values from Abe (12 GeV proton beam on a copper target, 3.5° and higher beam angles) to generate x_F and p_T and using the Beretvas coefficients, the magnitude of the Λ production cross section from the Beretvas fit can be compared to Abe data (Figure 10.3). The Beretvas fit is not a good match to this data, as it is too large overall. Does this mean that the Beretvas fit is invalid for E888? The ranges of x_F and p_T overlap for all three experiments, so it seems that the production cross section does not scale with these variables.

Given that the Beretvas coefficients do not seem to describe the Abe data very well, can we use the Skubic equation and the Abe data points to get a better fit? Using Minuit to fit the Abe data at 3.5°, 5.0°, and 6.5° to Equation 10.4 and using the Beretvas coefficients as the initial conditions, the coefficients shown in Table 10.2 were obtained. Figure 10.3 also shows the data and this fit at 3.5° and 6.5°. This figure also shows a comparison of the two fits at E888 energies and angles. The Abe fit is clearly a better fit to the Abe experimental data than the Beretvas fit.

Blobel

The data from Blobel might seem to be the best comparison to E888, since it was taken at the same energies, though it was $p+p \rightarrow \Lambda+X$, but the cross section should scale as $\sim A^{2/3}$. Unfortunately, unlike the Beretvas and Abe data, this data is available only in the form of very small and hard-to-read figures in the original paper, with no error bars (a request for the original data from several of the collaborators was unsuccessful). One of our collaborators,

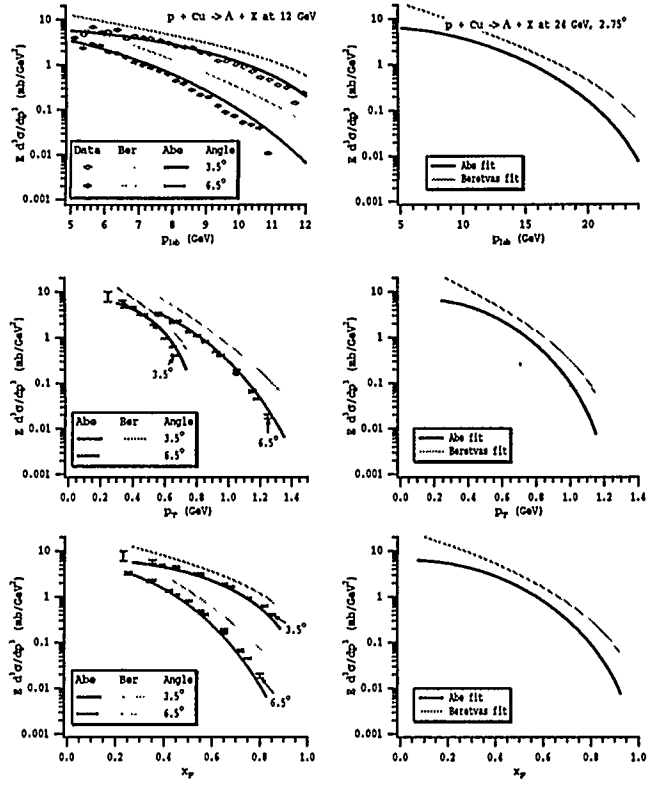

Figure 10.3: *Left:* Invariant cross section versus p_{lab}, x_F, and p_T for the Abe data and the fits of the Beretvas and Abe data to the Skubic parameterization at 12 GeV. *Right:* Abe and Beretvas fits at the E888 energy and angle.

R. Cousins, fit this data using the Skubic parameterization and obtained the coefficients shown in the final column of Table 10.2. This fit was used to calculate the H $\Lambda\Lambda$ coalescence production cross section [19]. A comparison of this fit to the Abe data and the Beretvas fit is shown in Figure 10.4.

Comparison

The Lorentz invariant cross section for each of the fits is shown in Figure 10.5. It can be seen that the Abe and Beretvas fits have much the same shape, but that the Abe fit is significantly smaller. Overall, the Blobel fit is about the same magnitude as Beretvas, but behaves differently at high and low momenta.

From Figure 10.3 and Figure 10.4, we see that the Beretvas fit is much the same shape as the 12 GeV Abe data, but has a much larger magnitude. So by using this spectrum, A_Λ and $P_\Lambda^{dk}(\Delta z)$ would be accurate, but $d\sigma_\Lambda/d\Omega$ would be too large. The Blobel fit does not match either the shape or magnitude of the Abe data, implying that this fit is less robust than the other two.

These fits can be used to generate MC events, then compared to the observed spectrum using Equation 10.3. Figure 10.6 shows this comparison. The acceptance effects of the detector wash out much of the spectrum dependence of any given fit, but it seems that the Abe and Beretvas spectra match the E888 data most closely, as can be seen by taking the ratio of the spectra. They have similar shapes, except at high and low momentum where the acceptance (and thus statistics) are low. The Blobel fit is too large at high momentum.

Since it seems likely that the match between the Abe data at $\sqrt{s} = 4.93$ GeV and 61 mrad is closer to the E888 data of $\sqrt{s} = 6.84$ GeV and 48 mrad

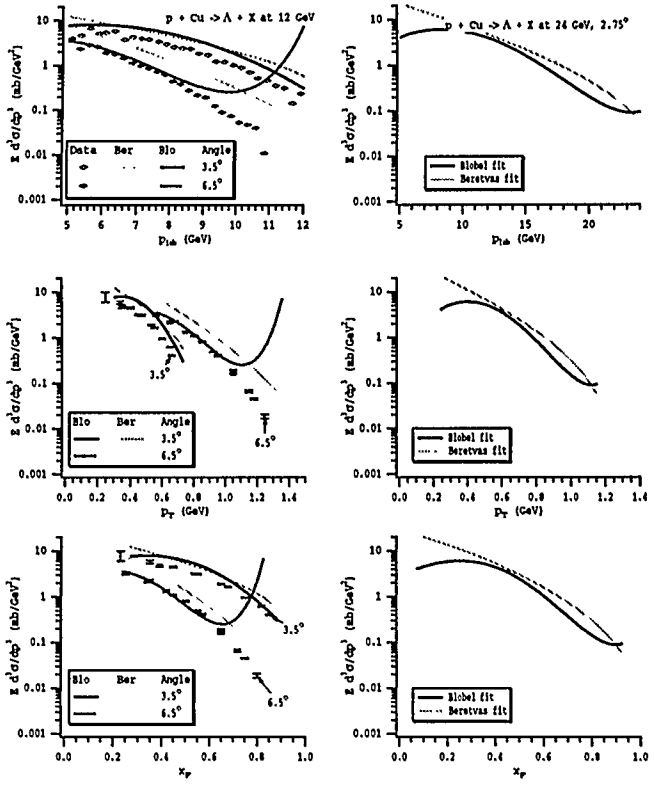

Figure 10.4: *Left:* Invariant cross section versus p_{lab}, x_F, and p_T for the Abe data and the fits of the Blobel and Abe data to the Skubic parameterization at 12 GeV. *Right:* Abe and Blobel fits at the E888 energy and angle.

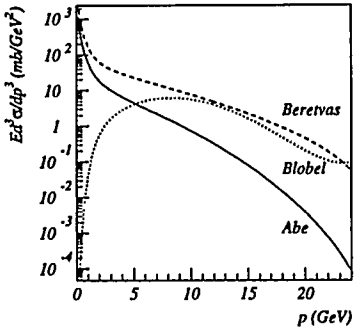

Figure 10.5: Comparison of the Lorentz invariant cross sections of the Beretvas, Abe, and Blobel fits.

than is the Beretvas $\sqrt{s} = 27.43$ GeV and 9.8 mrad, and the Blobel fit does not seem to match either the Beretvas or Abe data, or the observed Λ spectrum, the Abe fit will be used to calculate the Λ production momentum spectrum in this dissertation.

Figures 10.2, 10.7, 10.8, and 10.9 show some of the resulting kinematic quantities for the Monte Carlo simulated Abe fit versus data from the target Λ sample. The number of events in each of these figures was normalized so that both data (solid line) and MC (dashed line) have the same number of events.

10.2.2 Numerical results

Using the Abe fit, 3.61×10^6 MC Λs between $5 \leq p \leq 20$ GeV were generated. Applying the cuts shown in Table A.3 under PSL9MC, the acceptance for target Λs is $17\,141/3\,617\,212 = 4.74 \times 10^{-3}$.

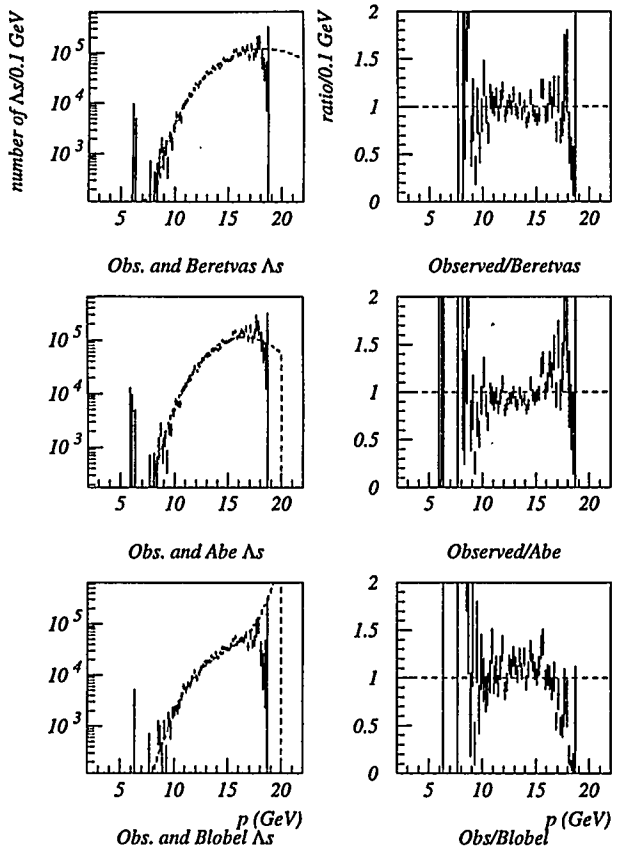

Figure 10.6: Comparison of observed data to the fits of Beretvas, Abe, and Blobel Λ momentum spectra, as seen in the VDR. *Left:* Data with error bars is the observed spectrum, dashes are Beretvas, Abe, and Blobel fit spectra. *Right:* Ratio of the two curves. The horizontal lines at unity are eyeguides; the curves were normalized so that the ratio would be near unity.

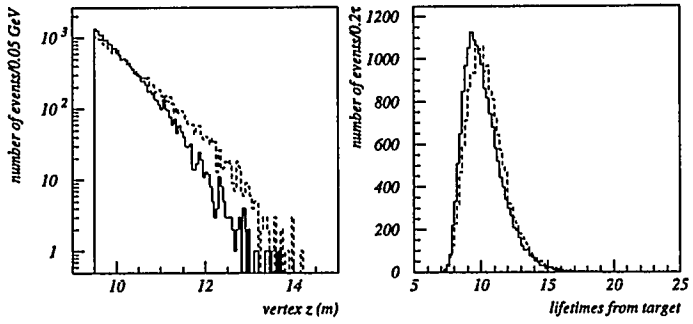

Figure 10.7: *Left:* z vertex of reconstructed target and MC Λs. *Right:* Number of lifetimes vertex is distant from the target.

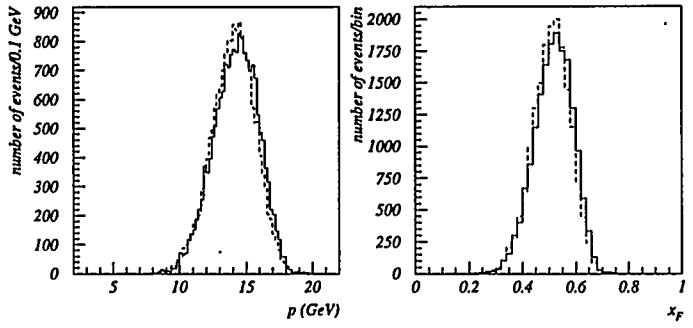

Figure 10.8: *Left:* Total reconstructed momentum of target and MC Λs. *Right:* Feynman x.

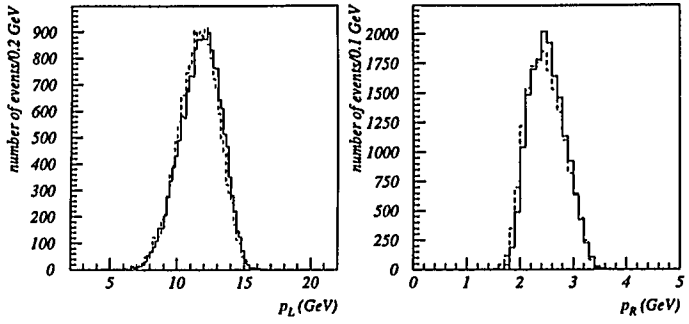

Figure 10.9: Momentum of left and right tracks of reconstructed target and MC Λs.

We can also find the differential cross section of Λ production by integrating Equation 10.4

$$\frac{d\sigma_\Lambda}{d\Omega} = \int_5^{20} \frac{d^3\sigma_\Lambda}{d\Omega dp}\, dp = \int_5^{20} \frac{p^2}{E} f(x, p_T)\, dp \tag{10.5}$$

and the probability that a Λ decayed in the decay region (Equation 5.2)

$$P_\Lambda^{dk}(\Delta z) = \frac{\int_5^{20} \frac{d^3\sigma_\Lambda}{d\Omega dp} P_\Lambda^{dk}(\Delta z, p)\, dp}{\int_5^{20} \frac{d^3\sigma_\Lambda}{d\Omega dp}\, dp}. \tag{10.6}$$

The former is 366 mb/sr; the latter 8.26×10^{-5}.

These numerical integrations were done using an E791-modified version of GAUSS, a CERNLIB integration routine.

10.3 H Acceptance

The momentum spectrum of Hs produced at the target is of course unknown, though predictions of its shape can be made using various models.

In order to find the acceptance of the detector for Hs given that many different momentum spectra may be used, a more general approach was taken. Monte Carlo Hs of a given mass and lifetime were generated with a *flat* momentum spectrum in the VDR and written to tape. The acceptance as a function of momentum [$\alpha_{flat}(p)$ (see Equation 10.1)] was found by applying the cuts determined from the H selection. Then for any *proposed* momentum spectrum at the target [$\mathcal{P}_H(p)$], the acceptance [A_H] was obtained by multiplying the proposed spectrum by the flat acceptance and the probability that an H of that mass, lifetime, and momentum would decay in Δz [$P_H^{dk}(\Delta z, p)$], without having to regenerate MC events for each proposed initial momentum spectrum. This method was checked by generating MC events with a specific spectrum and comparing the acceptances. The two results agreed to within 5%.

A sample acceptance A_H is shown in Figure 10.10 for an H of mass 2.21 GeV and $c\tau$ = 1.875 m. Similar plots were generated for a range of lifetimes and masses. From these plots, the acceptance as a function of momentum was integrated to find A_H. From the initial momentum spectra shown in Figure 10.11, the probability that an H decayed in the VDR was (see Equation 10.6)

$$P_H^{dk}(\Delta z) = \frac{\sum_{p=5}^{p=20} \frac{dN_H(p)}{d\Omega dp} P_H^{dk}(\Delta z, p)\Delta p}{\sum_{p=5}^{p=20} \frac{dN_H(p)}{d\Omega dp}\Delta p}. \tag{10.7}$$

The relationship between mass, lifetime, and branching ratio used to generate Monte Carlo events and calculate sensitivities was taken from Donoghue, *et al.* (Figure 1.2) [2], as described in Section 1.2. The specific values used are shown in Table 10.3. The values of acceptance [$\alpha_{flat}(p)$] used to make these calculations are shown in Appendix B. These are the only numbers needed to

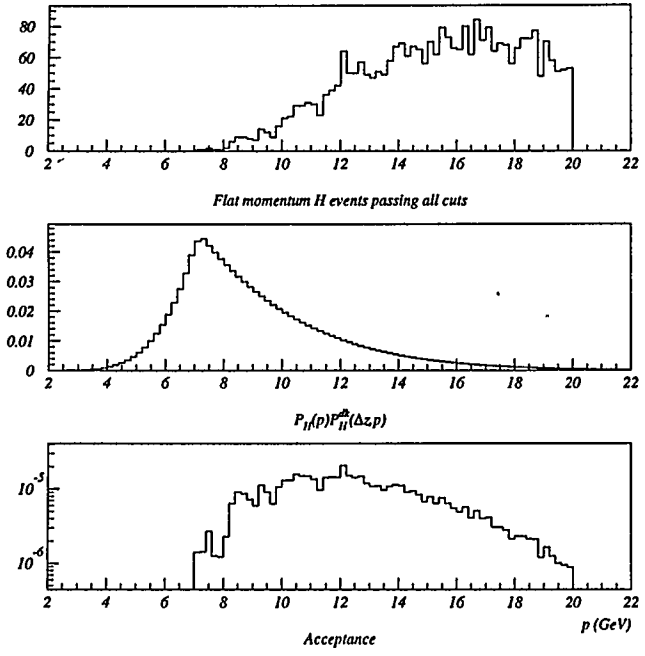

Figure 10.10: Monte Carlo calculation of H acceptance for an H of mass 2.21 GeV and $c\tau$ = 1.875 m. *Top:* Relative number of events passing all cuts given a flat momentum spectrum in the decay volume. *Center:* Probability that an H decays in the decay volume given the original coalescence production spectrum. *Bottom:* Resulting acceptance.

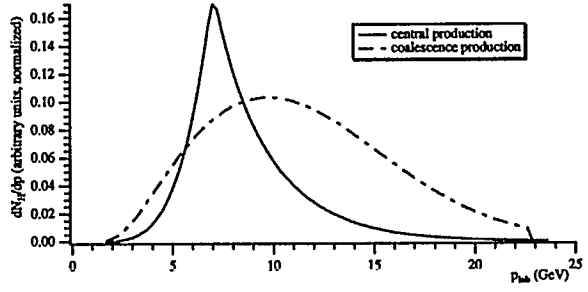

Figure 10.11: The H production momentum spectra from coalescence models used to calculate the H acceptance.

redo this calculation for a different H production momentum spectrum. These numbers are primarily dependent on the lifetime; the mass has little effect on the acceptance of the decay.

Two initial momentum spectra for H production were used to calculate acceptance (Figure 10.11, Section 1.3). These spectra were generated from a coalescence model calculation of H production [18, 19]. The more peaked spectrum was a central production coalescence model; the updated spectrum is based on improvements in the model. Both spectra were used to calculate the acceptance.

10.4 Single Event Sensitivity

All the numbers needed to calculate the H single event sensitivity from Equation 5.3 are now at hand. If the number of Hs is taken to be 1, this

m_H (GeV)	$c\tau_H$ (m)	τ_H (ns)	Br($H \rightarrow \Sigma^0 n$): Br($H \rightarrow \Lambda n$)
2.09	69.0	230	0:1
2.12	43.5	145	0:1
2.15	3.00	10	0.39:0.30
2.18	2.40	8	0.42:0.22
2.21	1.875	6.25	0.43:0.20

Table 10.3: Mass, $c\tau$, lifetime, and branching ratio of the H used in this analysis, taken from Donoghue, *et al.* [2]

equation gives the single event sensitivity (SES). The final production cross section limit will be determined by the number of events observed in the H signal sample and the estimated background. Summarizing,

$\frac{d\sigma_\Lambda}{d\Omega} = 366$ mb/sr

$A_\Lambda = 4.74 \times 10^{-3}$

$P_\Lambda^{dk}(\Delta z) = 8.26 \times 10^{-5}$

$N_H^{obs} = 1$ (single event sensitivity)

$N_\Lambda^{obs} = 20\,433$

$\mathrm{Br}(\Lambda \rightarrow p\pi^-) = 0.64.$

The remaining terms in Equation 5.3 vary as the H mass and lifetime and are presented in Table 10.4 for a representative selection of values, along with the result for each term.

	Central			*Coalescence*		
m_H (GeV)	A_H	$P_H^{dk}(\Delta z)$	$d\sigma_H/d\Omega$ (μb/sr)	A_H	$P_H^{dk}(\Delta z)$	$d\sigma_H/d\Omega$ (μb/sr)
2.09	6.44×10^{-6}	0.0318	19.5	1.24×10^{-5}	0.0257	12.5
2.12	2.12×10^{-5}	0.0496	3.81	4.52×10^{-5}	0.0403	2.19
2.15	6.32×10^{-5}	0.2375	0.387	1.50×10^{-4}	0.2338	0.166
2.18	8.94×10^{-5}	0.2227	0.313	2.26×10^{-4}	0.2322	0.119
2.21	9.74×10^{-5}	0.1916	0.342	2.54×10^{-4}	0.2165	0.116

Table 10.4: H single event sensitivity.

10.5 Estimated Λ Production

As a check on the validity of the calculations, these numbers can be substituted into Equation 5.1, replacing the H subscripts with Λ, and the results compared to the number of Λs actually observed. The only numbers in this equation which have not been discussed are N_p and ϵ_Λ^{det}. N_p was measured by the E888 secondary emission counters (B5SEC) as 3.3×10^4 Tp (using 1746 counts/TP) and by the B5T1 telescopes as 2.0×10^4 Tp (12 500 counts/Tp). The latter is used here as it accounts for targeting efficiency. Physics deadtime was less than 1%, and the detector efficiency (including pattern recognition) was approximately 70%. Level 3 efficiency was unknown, but in the past has been measured to be greater than 85% (L3 efficiency was a function of the opening angle of the decay, which is larger for $K_{2\pi}$ than for Λ), so that $\epsilon_\Lambda^{det} = 0.6$. The normalization loss due to acceptance and particle ID cuts was $\epsilon_\Lambda^{cut} = 0.8$. The proton absorption cross section in copper is $\sigma_p^{abs} = 801$ mb [80]. Then

$$
\begin{aligned}
N_\Lambda^{pred} &= (0.748)(2.0 \times 10^{16}) \left(\frac{(366)\, 65 \times 10^{-6}}{801} \right) \\
&\times (8.26 \times 10^{-5})(0.64)(4.74 \times 10^{-3})(0.65)(0.80)(0.6) \\
&= 3.45 \times 10^4 \text{ } \Lambda\text{s predicted} \qquad (10.8)
\end{aligned}
$$

compared to $N_\Lambda^{obs} = 2.3 \times 10^4$ Λs observed.

This last equation can be used to compare the validity of the Abe, Beretvas, and Blobel fits to once again justify the chosen target Λ spectrum. Table 10.5 contains several of the Λ and H parameters upon which the final limit depends for each fit. The most relevant is N_Λ^{obs}. The Blobel fit predicted only 40% of the Λs seen (a factor of 2.5 off). The Abe fit overestimated the number of Λs by 70% (factor of 1.7). The Beretvas fit was too large by almost a factor of three. The Abe fit again seems the best of the three.

	A_Λ	$P_\Lambda^{dk}(\Delta z)$	$d\sigma_\Lambda/d\Omega$	$\propto d\sigma_H/d\Omega$	N_Λ^{pred}
Beretvas	3.70×10^{-3}	7.97×10^{-5}	827	2.44×10^{-4}	6×10^4
Abe	4.74×10^{-3}	8.26×10^{-5}	366	1.43×10^{-4}	3.45×10^4
Blobel	7.86×10^{-4}	8.21×10^{-5}	520	3.36×10^{-5}	8.13×10^3

Table 10.5: Comparison of E888 results using the Beretvas, Abe, and Blobel lambda fits. N_Λ^{obs} was 20433. The Abe fit predicts the number of observed lambdas most closely.

Chapter 11

Results

...and in his brain, -
Which is as dry as the remainder biscuit
After a voyage, -he hath strange places cramm'd
With observation, the which he vents
In mangled forms.
-William Shakespeare, As You Like It

11.1 Summary

Now the results of the H selection and the target Λ normalization can be combined to find the sensitivity of the experiment.

Two events were found in the signal region, both in the He-N_2 sample; both appeared to be golden Λs with very good reconstruction and event quality characteristics (Table 11.1). Their $\not{p}_T$ were 187 and 191 MeV, a region kinematically forbidden to $K_{\mu 3}$s given the cuts made[1] (Figure 11.1, and also Figure 8.5). These events had N_τ of 6.7 and 9.4, making them unlikely to be Λs from secondary interactions. The PbG response for the candidate tracks was uncharacteristic of electrons (Figure 11.2).

[1]There is an event in Figure 9.11 which is separate from the $K_{\mu 3}$ band at $N_\tau \simeq 7$ and $\not{p}_T = 164$ MeV/c, which corresponds to the event in the left plot of Figure 11.1 at $m_{\pi\pi} \simeq 0.395$ GeV/c^2, clearly distinct from the $K_{\mu 3}$s.

The background from secondary interactions in the He-N_2 (Freon) sample was estimated to be fewer than 0.087 (0.064) events. A measurement of $K_{\ell 3}$ background from data indicated fewer than 0.21 background events from semi-leptonic kaon decays. The background from interactions with residual gas molecules in the vacuum decay region was less than 0.04 event. The total expected background was then less than 0.40 events. The probability of 0.40 background events fluctuating up to two or more events is 0.063; if such a fluctuation occurred, it is remarkable that the p_T of the events is so similar.

SIGNAL EVENT CHARACTERISTICS		
Run Number	30217	30241
$m_{p\pi}$ (GeV)	1.1164	1.1138
$\not{p}_T$ (GeV)	0.1871	0.1910
N_τ	6.7	9.4
z_s (m)	10.465	11.005
z_{vertex} (m)	13.789	14.458
p (GeV)	7.017	5.225
p L,R (GeV)	5.51/1.50	4.10/1.12
vertex χ^2	3.85	0.054
x track χ^2 L/R	0.80/2.37	2.27/5.31
y track χ^2 L/R	9.94/2.13	1.37/7.59
# hits x L/R	11/10	10/10
# hits x L/R	10/10	10/10
E/p L/R	0.36/0.44	0.18/0.27
E_c/E_{tot} L/R	0.034/0.00	0.107/0.000
TSC time (ns)	-0.11	-1.28

Table 11.1: Summary of signal event characteristics.

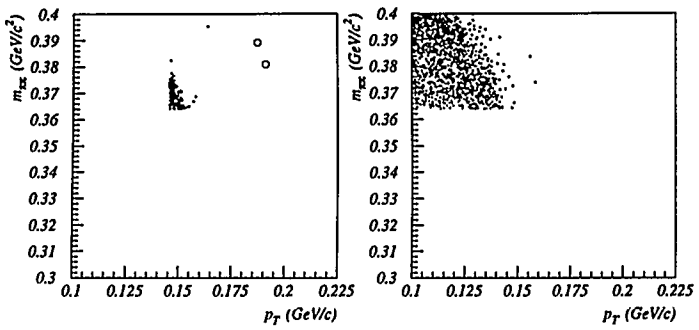

Figure 11.1: *Left:* The events in Figure 9.11 plotted as $m_{\pi\pi}$ versus $\not{p}_T$. The candidate events' response is circled. *Right:* MB $K_{\mu 3}$s. This plot clearly shows that the candidate events are kinematically unlikely to be $K_{\mu 3}$s, and that the band of events in the He-N_2 sample are $K_{\mu 3}$s.

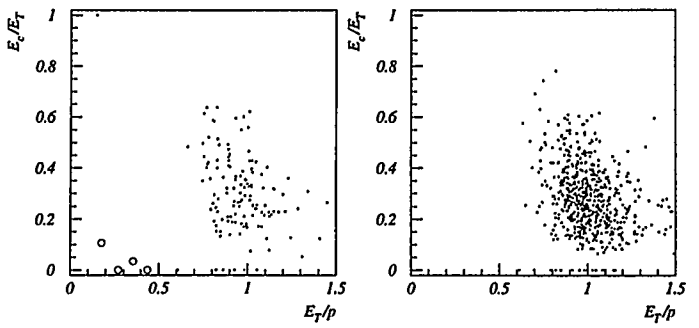

Figure 11.2: *Left:* The PbG response of the final event sample with all cuts *except* the PbG cuts, including the N_τ and p_T cuts. The candidate events' response is circled (two tracks/event). *Right:* MB K_{e3}s selected using the CER counters, and chosen to have the same track momentum asymmetry as a Λ.

11.2 Differential Production Cross Section Measurement

The production cross section limit is found from

$$\frac{d\sigma_H}{d\Omega} = \frac{\xi}{N_\Lambda^{obs}} \frac{\mathrm{Br}(\Lambda \rightarrow p\pi^-)}{\mathrm{Br}(H \rightarrow \Lambda X)} \frac{A_\Lambda}{A_H} \frac{P_\Lambda^{dk}}{P_H^{dk}} \frac{d\sigma_\Lambda}{d\Omega}. \tag{11.1}$$

which was derived earlier (Equation 5.3) and is repeated here for convenience. N_H^{obs} has been replaced with ξ, the Poisson multiplier for the 90% C.L. given the number of events observed. Based on two events with fewer than 0.50 background events predicted from data, we set a 90% C.L. limit of $5.32 \times SES$.

Table 11.2 contains the H production cross section limit for several values of H mass and lifetime and both spectra. The more conservative central production spectrum will be used to set the limit.

Since the absolute magnitude of the Λ production cross section is not well known at our energies and beam angles (although we do know the shape, and thus the acceptance and $P_\Lambda^{dk}(\Delta z)$, independent of the magnitude), we can remove this dependence from the limit (Table 11.3). Figure 11.3 shows these values graphically.

Donoghue *et al.* [2] stated that the lifetime of the H by their calculations could be as much as half less than they stated, due to the unknown P-wave contribution. Table 11.3 and Figure 11.3 also contains the limit of the central production spectrum based on the shorter lifetimes.

For $m_H = 2.15$ GeV, Jaffe's original prediction, and $\tau_H = 10$ ns from Donoghue,

$$\left.\frac{d\sigma_H}{d\Omega}\right|_{48\ \mathrm{mr}} < \left(6.3 \times 10^{-6}\right) \left.\frac{d\sigma_\Lambda}{d\Omega}\right|_{48\ \mathrm{mr}} \quad (90\%\ \mathrm{C.L.}) \tag{11.2}$$

From Section 10.2.2, $d\sigma_\Lambda/d\Omega|_{48\ \mathrm{mr}} = 366$ mb/sr, so $d\sigma_H/d\Omega|_{48\ \mathrm{mr}} < 2.3$ μb/sr.

	Central	*Coalescence*
m_H (GeV)	$d\sigma_H/d\Omega$ (μb/sr)	$d\sigma_H/d\Omega$ (μb/sr)
2.09	117	74.7
2.12	22.8	13.1
2.15	2.31	1.0
2.18	1.87	0.71
2.21	2.04	0.69

Table 11.2: H production cross section limit (90% C.L.).

		Central	*Coalescence*	*Central, 1/2 lifetime*
H Mass (GeV/c^2)	H lifetime (ns)	$\frac{d\sigma_H/d\Omega}{d\sigma_\Lambda/d\Omega}$	$\frac{d\sigma_H/d\Omega}{d\sigma_\Lambda/d\Omega}$	$\frac{d\sigma_H/d\Omega}{d\sigma_\Lambda/d\Omega}$
2.09	230	320×10^{-6}	204×10^{-6}	86.3×10^{-6}
2.12	145	62.2×10^{-6}	35.8×10^{-6}	18.4×10^{-6}
2.15	10	6.32×10^{-6}	2.71×10^{-6}	10.9×10^{-6}
2.18	8	5.12×10^{-6}	1.94×10^{-6}	12.8×10^{-6}
2.21	6.25	5.58×10^{-6}	1.89×10^{-6}	26.0×10^{-6}

Table 11.3: 90% C.L. production cross section limit, relative to the Λ production cross section. Also shown is the relative cross section for the central production momentum with a lifetime half that shown, since lifetimes may be 50% lower than shown.

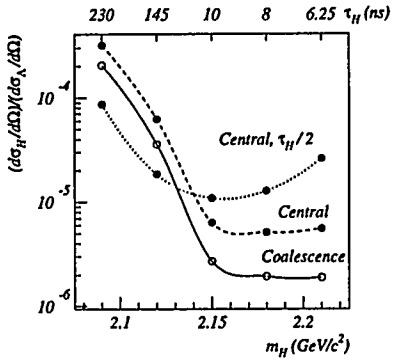

Figure 11.3: 90% C.L. H production cross section in terms of the Λ production cross section. Filled circles are the central production model, open circles the coalescence production model. The dotted line with filled circles corresponds to the Donoghue masses with half the lifetime shown on the top axis.

11.3 Total Production Cross Section Estimate

The result presented above, while being a precise statement of the quantity measured by this experiment, leaves something to be desired in terms of generality and comparison to other experiments. Instead of a differential cross section in a small region of phase space, a total cross section is more useful as a comparison, though it may be further removed from the experimental data. To extrapolate the total cross section from the differential requires knowledge of the analytic form of the differential cross section, or a numerical model containing both quantities [81].

A common analytic form for the invariant cross section of inclusive production is

$$E\frac{d^3\sigma}{dp^3} = \eta\sigma_H(1-|x_F|)^{C_5}e^{-C_6p_T^2}. \qquad (11.3)$$

The coefficients C_5 and C_8 are used to show the similarity to Equation 10.4, and η is a normalization constant. Equation 11.3 can be restated as

$$\frac{d^2\sigma}{dp\,d\theta} = 2\pi p_T \eta \sigma_H (\frac{p}{E})(1-|x_F|)^{C_8} e^{-C_5 p_T^2}. \quad (11.4)$$

Then since production is azimuthally symmetric,

$$\frac{d^2\sigma}{dp\,d\Omega} = \frac{1}{2\pi sin\theta}\frac{d^2\sigma}{dp\,d\theta} \quad (11.5)$$

For Ξ^0 production on a copper target (also $S=-2$), Beretvas found $C_5 = 3.52$ and $C_8 = 1.48$. This slope parameter for p_T^2 is low for these energies, so the value measured by the dissociation phase of E888 for ΛK_S production, 9 GeV^{-2}, will be used [46]. Transforming to the center-of-mass frame (where p and θ are not constrained by each other), numerical integration results in $\eta = 5.57$. In this frame, our limit can be stated as

$$\frac{d^2\sigma}{dp^*\,d\theta^*} < 0.12 \frac{\mu b}{\text{rad GeV/c}}, \quad (11.6)$$

where the asterisk denotes center-of-mass variables.

Equating 11.4 and 11.6 and inserting the relevant values for p_T (0.36 GeV) gives a limit of $\sigma_H < 32$ nb. Varying C_8 from 6-12 and C_5 from 1.5-6.5, σ_H varies by a factor of three, from 19 nb to 61 nb. Scaling the most conservative limit by $A^{2/3}$, $\sigma_H < 3.8$ nb/nucleon.

Chapter 12

Conclusion

It seemed that out of battle I escaped
Down some profound dull tunnel, long since scooped
Through granites which titanic wars had groined.

'Strange friend,' I said, 'here is no cause to mourn.'
'None,' said the other, 'save the undone years,
The hopelessness. Whatever hope is yours
Was my life also; I went hunting wild
After the wildest beauty in the world.'
–Wilfred Owen, Strange Meeting

This experiment searched for the H dibaryon in a neutral beam for two weeks in 1992. Though people started thinking about using E791 to search for the H a year earlier, the experiment was not proposed until January 1992, received approval in March, and began to run in May 1992. This short interval did not hinder preparations for the run, and despite some serious setbacks, the experiment began taking data on time. After the initial flurry of activity, the analysis proceeded in fits and starts for the next three years, interrupted by other work deemed more crucial. What difference if the H was found this year or next?

After all this, what can be said about the H? Perhaps the question can be stated in terms of what we might have expected to find. The result that

would have been easiest to interpret would have been numerous Λs clustered in a Gaussian peak around m_Λ, with a well-formed Jacobian peak in p_T, which could have been fit to an H mass assuming an undetected neutron. The lifetime could then have been found from the distribution of the particles in z. Of course this did not happen, making interpretation of the results more difficult.

The simplest answer is that we found no convincing evidence of the Hs existence, though we did find two events which are not inconsistent with an H of mass 2.093 GeV/c^2, and are significantly above our conservative background estimate of less than 0.4 events. Based on these two events, this phase of the E888 experiment placed a limit on the differential production cross section within a restricted region of phase space, though one hitherto unexplored. Our measurement of $d\sigma_H/d\Omega < 2.3$ μb/sr for an H of mass 2.15 GeV/c^2 [82] and the lifetime of 10 ns predicted by Ref. [2] can be compared to the coalescence model prediction of Cousins and Klein of ~ 100 μb/sr for this targeting angle and beam energy [19].

The differential cross section, however, is inconvenient to compare to other experiments or theory. In the previous section, this limit was extrapolated to a limit on the total cross section, which is more useful for comparison, and the conservative estimate of $\sigma_H = 61$ nb for p+Cu $\rightarrow$ H+X inclusive production at AGS energies was obtained. This can be compared to the theoretical prediction of Cole of $\sigma_H = 15$ μb at AGS energies, and Rotondo's 1.2 μb at Fermilab energies. Scaling by $A^{2/3}$ to nuclear targets, our limit of $\sigma_H < 3.8$ nb/nucleon can be compared to the experimental results of Carroll of $\sigma_H < 40$ nb/nucleon for $2.1 < m_H < 2.23$ GeV/c^2 (at 5 GeV/c and based on the assumption of flat production phase space), and Gustafson's $\sigma_H < 65$ nb/nucleon for neutral particles with lifetime greater than 100 ns. The RISK experiment found $\sigma_H < 160$ μb, while Shahbazian measured 60 nb, based on the Hs they claimed to see. Alexseev found a limit of $\sigma_H \mathrm{Br}(H \rightarrow \Lambda p\pi^-)P_H = 18$ nb based on their single event, so unless the branching ratio of this decay was greater than 30% (Ref. [2] implies that it occurs at the level of a few percent), E888 was more sensitive than all of these.

Other experiments have stated their results in terms of processes which are difficult to convert to a more general cross section. The experiments which have reported observation of one or a few Hs are either questionable for various reasons, or disagree with one another, and provide no definitive evidence of existence. The early double hypernuclei events observed are doubtful, and the most recent has yet to be verified by another experiment. All are open to interpretation as H decays.

From an experimental standpoint, I conclude that the E888 decay search was an order-of-magnitude more sensitive than previous experiments. In any case, E888 explored a different region of H production phase space than any previous experiment. Comparison of our results to current theoretical estimates leads to the conclusion that either the H does not exist or that the models used to estimate H production are in significant need of revision.

Appendix

Appendix A

Cut Summaries

	Λ strip	High p_T, low θ_C^2, Λ mass sample selection
Code	PSL4	PSL5
Event quality		
L3	no	yes
vertex χ^2 (QT)	> 25	> 25
track χ^2 (QT)	> 50	> 50
opposite charge	yes	yes
# of tracks	< 2	< 2
# hits in fit	no	no
TSC in time	$\mid t_{avg} \mid$ > 4ns	$\mid t_{avg} \mid$ > 4ns
TSC hits	< 2	< 2
Fiducial Volume		
z vertex	no	< 9.5
vacuum flange	yes	yes
PbG acceptance	yes	yes
aperture projection	yes	yes
MIIO acceptance	no	no
upstream SNI projection	no	no
Particle Identification		
CER	$\mid t_{cer} - t_{avg} \mid$ > 4ns	$\mid t_{cer} - t_{avg} \mid$ > 4ns
PbG	$E/p > 0.70$	$E/p > 0.70$
MIIO	no	no
MRG	no	no
Kinematic		
track $p_{L,R}$	< 1.0	< 1.0
$K_L \to \pi^+\pi^-\pi^0$	$m_{\pi\pi}$ < 364 MeV	$m_{\pi\pi}$ < 364 MeV
$K_L \to \pi^+\pi^-$	$\mid m_K - m_{\pi\pi} \mid$ < 6 MeV	$\mid m_K - m_{\pi\pi} \mid$ < 6 MeV
Signal and Normalization		
θ_C^2	no	($\geq$ 10 mrad^2)
m_Λ	no	($\mid m_\Lambda - m_{p\pi} \mid \geq$ 2.5 MeV)
$\not{p}_T$	no	(< 0.145)
N_τ	no	no
z_s	no	no

Table A.1: Summary of initial cuts applied to the physics data. PSL4 selected events from the physics sample on the basis of event quality, and these events were stripped into three classes in PSL5. Masses and momenta in GeV and distance in meters unless otherwise noted.

	H selection on high p_T PSL5 events	MC H selection
Code	PSL10	PSL8MC
Event quality		
L3	yes [5]	n/a
*vertex χ^2	> 5	> 25
*track χ^2	> 15	> 5
opposite charge	yes [5]	yes
*# of tracks	< 2 [5]	n/a
*# hits in fit	< 9 or > 11	n/a
TSC in time	$\mid t_{avg} \mid$ > 4ns [5]	n/a
TSC hits	< 2 [5]	n/a
Fiducial Volume		
z vertex	< 9.5 [5]	< 9.5
vacuum flange	yes [5]	yes
PbG acceptance	yes [5]	yes
aperture projection	yes [5]	yes
MIIO acceptance	yes	yes
upstream SNI projection	hot spot cut at $z_s = 8.3, 9.3, 11.0$ m	hot spot cut at $z_s = 8.3, 9.3, 11.0$ m
Particle Identification		
CER	$\mid t_{cer} - t_{avg} \mid$ > 4ns [5]	n/a
*PbG	p < 2 GeV, E/p > 0.52 p > 2 GeV, E/p > 0.60 $(E_c/E_T)_R$ > 0.66	n/a
MIIO	x and y hits, in time (4 ns)	no pion decay upstream of z_{mho}
MRG	> 65% expected range	n/a
Kinematic		
track $p_{L,R}$	< 1.0 [5]	< 1.0
$K_L \to \pi^+\pi^-\pi^0$	$m_{\pi\pi}$ < 364 MeV[5]	$m_{\pi\pi}$ < 364 MeV
$K_L \to \pi^+\pi^-$	$\mid m_K - m_{\pi\pi} \mid$ < 6 MeV[5]	$\mid m_K - m_{\pi\pi} \mid$ < 6 MeV
Signal and Normalization		
*θ_C^2	no	no
*m_Λ	$\mid m_\Lambda - m_{p\pi} \mid \geq$ 2.5 MeV	$\mid m_\Lambda - m_{p\pi} \mid \geq$ 2.5 MeV
*$\not{p}_T$	< 0.174	< 0.174
*N_τ	< 5	< 5
*z_s	z_s < 9.65, z_s > 13.0	z_s < 9.65 z_s > 13.0

Table A.2: Summary of cuts applied to the high-$\not{p}_T$ H-decay data selected in PSL5 to obtain the final signal sample, and the corresponding cuts applied to the Monte Carlo data used to calculated acceptance. The *starred items in the first column are the *tight cuts*. The items denoted with [5] means that cut was made in the PSL5 strip.

	Target Λ selection on low $\theta_C{}^2$ PSL5 events	MC Λ selection
Code	PSL9	PSL9MC
Event quality		
L3	yes [5]	n/a
*vertex χ^2 (QT)	> 5	> 25
*track χ^2 (QT)	> 15	> 50
opposite charge	yes [5]	yes
# of tracks	< 2 [5]	n/a
*# hits in fit	< 9 or > 11	n/a
TSC in time	$\mid t_{avg} \mid > 4$ns [5]	n/a
TSC hits	< 2 [5]	n/a
Fiducial Volume		
z vertex	< 9.5 [5]	< 9.5
vacuum flange	yes [5]	yes
PbG acceptance	yes [5]	yes
aperture projection	yes [5]	yes
MHO acceptance	yes	yes
upstream SNI projection	hot spot cut at $z_s = 8.3, 9.3, 11.0$ m	hot spot cut at $z_s = 8.3, 9.3, 11.0$ m
Particle Identification		
CER	$\mid t_{cer} - t_{avg} \mid > 4$ns [5]	n/a
*PbG	$p < 2$ GeV, $E/p > 0.52$ $p > 2$ GeV, $E/p > 0.60$ $(E_c/E_T)_R > 0.66$	n/a
MHO	x and y hits, in time (4ns)	no pion decay upstream of z_{mho}
MRG	$> 65\%$ expected range	n/a
Kinematic		
track $p_{L,R}$	< 1.0 [5]	< 1.0
$K_L \to \pi^+\pi^-\pi^0$	$m_{\pi\pi} < 364$ MeV [5]	$m_{\pi\pi} < 364$ MeV
$K_L \to \pi^+\pi^-$	$\mid m_K - m_{\pi\pi} \mid < 6$ MeV [5]	$\mid m_K - m_{\pi\pi} \mid < 6$ MeV
Signal and Normalization		
*θ_C^2	$\geq$ 1.5 mrad^2	$\geq$ 1.5 mrad^2
*m_Λ	$\mid m_\Lambda - m_{p\pi} \mid \geq 2.5$ MeV	$\mid m_\Lambda - m_{p\pi} \mid \geq 2.5$ MeV
*$\not{p}_T$	no	no
*N_τ	no	no
*z_s	no	no

Table A.3: Summary of cuts applied to the low-θ_C^2 normalization data selected in PSL5, and the corresponding cuts applied to the Monte Carlo data used to calculate acceptance. The *starred items in the first column are the *tight cuts*. The items denoted with [5] means that cut was made in the PSL5 strip.

Code	$K_L \to \pi^+\pi^-$ Selection PSPP9	MC $K_L \to \pi^+\pi^-$ selection PSPP9MC
Event quality		
L3	no	n/a
*vertex χ^2	> 5	> 25
*track χ^2	> 15	> 50
opposite charge	yes	yes
# of tracks	< 2	n/a
*# hits in fit	< 9 or > 11	n/a
TSC in time	$\mid t_{avg} \mid > 4$ns	n/a
TSC hits	< 2	n/a
Aperture		
z vertex	< 9.5	< 9.5
vacuum flange	yes	yes
PbG acceptance	yes	yes
Fiducial volume	yes	yes
MHO acceptance	yes	yes
upstream SNI projection	no	no
Particle Identification		
CER	$\mid t_{cer} - t_{avg} \mid > 4$ns	n/a
*PbG	$p < 2$ GeV, $E/p > 0.52$ $p > 2$ GeV, $E/p > 0.60$ $(E_c/E_T)_R > 0.66$	n/a
MHO	x and y hits, in time (4ns)	no pion decay upstream of z_{mho}
MRG	$> 65\%$ expected range	n/a
Kinematic		
track $p_{L,R}$	< 1.0	< 1.0
$K_L \to \pi^+\pi^-\pi^0$	$m_{\pi\pi} < 364$ MeV	$m_{\pi\pi} < 364$ MeV
$K_L \to \pi^+\pi^-$	$\mid m_K - m_{\pi\pi} \mid > 6$ MeV	$\mid m_K - m_{\pi\pi} \mid > 6$ MeV
Signal and Normalization		
*θ_C^2	$\geq$ 1.5 mrad^2	$\geq$ 1.5 mrad^2
*m_Λ	no	no
*$\not{p}_T$	no	no
*N_τ	no	no
*z_s	no	no

Table A.4: Summary of cuts applied to the minimum bias data and the corresponding cuts on Monte Carlo data. The *starred items in the first column are the *tight cuts*. All masses and momenta in GeV and distance in meters unless otherwise noted.

Appendix B

Acceptance

m_{ll}(GeV/c^2)	2.09	2.12	2.15	2.18	2.21
τ (ns)	230	145	10	8	6.25
p (GeV/c)	*Acceptance as a function of momentum*				
7.30					3.21×10^{-5}
7.50			9.06×10^{-5}		6.41×10^{-5}
7.70		9.20×10^{-5}	5.97×10^{-5}	3.14×10^{-5}	3.16×10^{-5}
7.90		3.11×10^{-5}	6.04×10^{-5}	1.27×10^{-4}	3.23×10^{-5}
8.10	5.78×10^{-5}	1.54×10^{-4}	8.94×10^{-5}	6.33×10^{-5}	6.42×10^{-5}
8.30	5.79×10^{-5}	1.85×10^{-4}	1.20×10^{-4}	9.53×10^{-5}	1.91×10^{-4}
8.50	1.45×10^{-4}	2.47×10^{-4}	6.04×10^{-5}	1.59×10^{-4}	2.86×10^{-4}
8.70	1.73×10^{-4}	3.07×10^{-4}	1.20×10^{-4}	1.91×10^{-4}	2.89×10^{-4}
8.90	1.16×10^{-4}	1.85×10^{-4}	1.80×10^{-4}	1.27×10^{-4}	2.56×10^{-4}
9.10	3.18×10^{-4}	2.78×10^{-4}	1.81×10^{-4}	1.26×10^{-4}	2.24×10^{-4}
9.30	4.36×10^{-4}	5.87×10^{-4}	2.72×10^{-4}	2.54×10^{-4}	4.50×10^{-4}
9.50	2.89×10^{-4}	8.33×10^{-4}	3.58×10^{-4}	3.78×10^{-4}	3.85×10^{-4}
9.70	6.63×10^{-4}	7.08×10^{-4}	5.08×10^{-4}	4.71×10^{-4}	2.86×10^{-4}
9.90	6.09×10^{-4}	9.88×10^{-4}	3.30×10^{-4}	4.74×10^{-4}	5.13×10^{-4}
10.1	4.94×10^{-4}	1.02×10^{-3}	3.64×10^{-4}	6.00×10^{-4}	6.68×10^{-4}
10.3	6.17×10^{-4}	1.28×10^{-3}	2.43×10^{-4}	6.72×10^{-4}	7.15×10^{-4}
10.5	8.94×10^{-4}	1.17×10^{-3}	6.27×10^{-4}	8.86×10^{-4}	9.20×10^{-4}
10.7	8.44×10^{-4}	1.64×10^{-3}	3.62×10^{-4}	8.28×10^{-4}	9.27×10^{-4}
10.9	5.19×10^{-4}	1.63×10^{-3}	6.56×10^{-4}	6.94×10^{-4}	9.90×10^{-4}
11.1	7.53×10^{-4}	1.42×10^{-3}	4.51×10^{-4}	8.88×10^{-4}	9.56×10^{-4}
11.3	7.53×10^{-4}	1.72×10^{-3}	6.93×10^{-4}	8.57×10^{-4}	7.36×10^{-4}
11.5	9.30×10^{-4}	2.06×10^{-3}	7.56×10^{-4}	1.11×10^{-3}	1.15×10^{-3}
11.7	8.98×10^{-4}	2.01×10^{-3}	8.08×10^{-4}	1.43×10^{-3}	1.25×10^{-3}
11.9	1.20×10^{-3}	2.42×10^{-3}	1.02×10^{-3}	1.23×10^{-3}	1.32×10^{-3}
12.1	9.24×10^{-4}	1.94×10^{-3}	1.07×10^{-3}	1.45×10^{-3}	2.03×10^{-3}
12.3	9.82×10^{-4}	2.21×10^{-3}	8.66×10^{-4}	1.18×10^{-3}	1.60×10^{-3}
12.5	9.52×10^{-4}	2.12×10^{-3}	9.31×10^{-4}	1.11×10^{-3}	1.61×10^{-3}
12.7	1.16×10^{-3}	2.27×10^{-3}	1.05×10^{-3}	1.39×10^{-3}	1.80×10^{-3}
12.9	1.29×10^{-3}	3.07×10^{-3}	9.85×10^{-4}	1.84×10^{-3}	1.55×10^{-3}
13.1	1.01×10^{-3}	2.40×10^{-3}	1.23×10^{-3}	1.52×10^{-3}	1.51×10^{-3}
13.3	1.66×10^{-3}	2.96×10^{-3}	1.45×10^{-3}	2.02×10^{-3}	1.63×10^{-3}
13.5	1.19×10^{-3}	2.49×10^{-3}	1.14×10^{-3}	1.80×10^{-3}	1.57×10^{-3}
13.7	9.30×10^{-4}	2.57×10^{-3}	1.02×10^{-3}	1.56×10^{-3}	1.87×10^{-3}
13.9	8.31×10^{-4}	2.45×10^{-3}	1.41×10^{-3}	2.05×10^{-3}	2.12×10^{-3}

Table B.1: Acceptance of E888 detector based on a flat momentum spectrum in the VDR. These values can be used to find the acceptance of this experiment for any initial H production momentum spectra (see Section 10.3).

m_H(GeV/c^2)	2.09	2.12	2.15	2.18	2.21
τ (ns)	230	145	10	8	6.25
p (GeV/c)	*Acceptance as a function of momentum, continued*				
14.1	1.18×10^{-3}	3.35×10^{-3}	1.17×10^{-3}	1.87×10^{-3}	2.20×10^{-3}
14.3	1.01×10^{-3}	3.02×10^{-3}	1.52×10^{-3}	1.89×10^{-3}	1.93×10^{-3}
14.5	1.28×10^{-3}	3.04×10^{-3}	1.27×10^{-3}	1.90×10^{-3}	2.15×10^{-3}
14.7	1.28×10^{-3}	2.72×10^{-3}	1.38×10^{-3}	2.30×10^{-3}	2.08×10^{-3}
14.9	8.66×10^{-4}	2.73×10^{-3}	1.56×10^{-3}	1.77×10^{-3}	1.78×10^{-3}
15.1	1.12×10^{-3}	3.10×10^{-3}	1.14×10^{-3}	1.79×10^{-3}	2.25×10^{-3}
15.3	1.32×10^{-3}	2.70×10^{-3}	1.20×10^{-3}	2.40×10^{-3}	1.97×10^{-3}
15.5	9.18×10^{-4}	3.22×10^{-3}	1.33×10^{-3}	1.89×10^{-3}	2.52×10^{-3}
15.7	1.03×10^{-3}	3.07×10^{-3}	1.48×10^{-3}	1.76×10^{-3}	2.29×10^{-3}
15.9	1.01×10^{-3}	2.82×10^{-3}	1.45×10^{-3}	1.91×10^{-3}	2.12×10^{-3}
16.1	1.29×10^{-3}	2.42×10^{-3}	1.06×10^{-3}	2.02×10^{-3}	2.05×10^{-3}
16.3	6.07×10^{-4}	3.11×10^{-3}	1.41×10^{-3}	2.02×10^{-3}	2.55×10^{-3}
16.5	8.43×10^{-4}	2.68×10^{-3}	1.36×10^{-3}	2.05×10^{-3}	1.98×10^{-3}
16.7	9.50×10^{-4}	2.80×10^{-3}	1.34×10^{-3}	2.01×10^{-3}	2.66×10^{-3}
16.9	9.55×10^{-4}	2.29×10^{-3}	1.48×10^{-3}	1.76×10^{-3}	2.27×10^{-3}
17.1	6.39×10^{-4}	2.69×10^{-3}	1.02×10^{-3}	1.55×10^{-3}	2.52×10^{-3}
17.3	9.77×10^{-4}	2.61×10^{-3}	1.26×10^{-3}	1.86×10^{-3}	2.04×10^{-3}
17.5	1.00×10^{-3}	2.75×10^{-3}	1.19×10^{-3}	1.66×10^{-3}	2.19×10^{-3}
17.7	9.83×10^{-4}	2.33×10^{-3}	1.14×10^{-3}	1.65×10^{-3}	2.17×10^{-3}
17.9	8.74×10^{-4}	2.46×10^{-3}	1.22×10^{-3}	1.51×10^{-3}	1.80×10^{-3}
18.1	6.33×10^{-4}	2.44×10^{-3}	1.34×10^{-3}	2.05×10^{-3}	2.10×10^{-3}
18.3	5.49×10^{-4}	2.12×10^{-3}	1.28×10^{-3}	1.57×10^{-3}	2.28×10^{-3}
18.5	6.92×10^{-4}	2.27×10^{-3}	1.37×10^{-3}	1.42×10^{-3}	2.29×10^{-3}
18.7	8.11×10^{-4}	2.41×10^{-3}	7.18×10^{-4}	2.03×10^{-3}	2.45×10^{-3}
18.9	5.75×10^{-4}	1.99×10^{-3}	1.16×10^{-3}	1.88×10^{-3}	1.53×10^{-3}
19.1	8.02×10^{-4}	2.22×10^{-3}	1.04×10^{-3}	1.65×10^{-3}	2.24×10^{-3}
19.3	5.42×10^{-4}	1.76×10^{-3}	7.81×10^{-4}	1.39×10^{-3}	1.86×10^{-3}
19.5	3.46×10^{-4}	1.82×10^{-3}	1.18×10^{-3}	1.69×10^{-3}	1.64×10^{-3}
19.7	3.76×10^{-4}	1.54×10^{-3}	9.54×10^{-4}	1.20×10^{-3}	1.66×10^{-3}
19.9	4.33×10^{-4}	1.96×10^{-3}	8.39×10^{-4}	1.39×10^{-3}	1.69×10^{-3}

Table B.2: Acceptance of E888 detector based on a flat momentum spectrum in the VDR, continued.

m_H(GeV/c^2)	2.09	2.12	2.15	2.18	2.21
τ (ns)	115	72.5	5	4	3.125
p (GeV/c)	*Acceptance as a function of momentum*				
7.30			2.10×10^{-5}		4.54×10^{-5}
7.50		4.29×10^{-5}	2.11×10^{-5}		2.27×10^{-5}
7.70		6.43×10^{-5}	4.19×10^{-5}	4.48×10^{-5}	2.25×10^{-5}
7.90	2.03×10^{-5}	8.62×10^{-5}	8.43×10^{-5}	6.78×10^{-5}	4.57×10^{-5}
8.10	6.03×10^{-5}	8.59×10^{-5}	6.31×10^{-5}		1.35×10^{-4}
8.30	4.02×10^{-5}	1.72×10^{-4}	6.25×10^{-5}	1.35×10^{-4}	6.78×10^{-5}
8.50	3.43×10^{-4}	2.36×10^{-4}	1.48×10^{-4}	2.25×10^{-4}	1.36×10^{-4}
8.70	1.41×10^{-4}	2.58×10^{-4}	1.26×10^{-4}	2.49×10^{-4}	2.28×10^{-4}
8.90	2.82×10^{-4}	3.23×10^{-4}	1.89×10^{-4}	2.26×10^{-4}	2.73×10^{-4}
9.10	2.42×10^{-4}	3.02×10^{-4}	1.90×10^{-4}	2.94×10^{-4}	3.41×10^{-4}
9.30	3.03×10^{-4}	7.12×10^{-4}	1.48×10^{-4}	2.94×10^{-4}	2.73×10^{-4}
9.50	5.04×10^{-4}	5.80×10^{-4}	2.94×10^{-4}	2.47×10^{-4}	3.64×10^{-4}
9.70	3.82×10^{-4}	6.88×10^{-4}	2.09×10^{-4}	4.96×10^{-4}	4.74×10^{-4}
9.90	5.26×10^{-4}	6.89×10^{-4}	4.43×10^{-4}	5.20×10^{-4}	4.56×10^{-4}
10.1	5.41×10^{-4}	1.24×10^{-3}	2.94×10^{-4}	6.52×10^{-4}	5.23×10^{-4}
10.3	8.93×10^{-4}	1.11×10^{-3}	4.24×10^{-4}	5.01×10^{-4}	6.89×10^{-4}
10.5	7.28×10^{-4}	1.29×10^{-3}	3.57×10^{-4}	7.85×10^{-4}	7.67×10^{-4}
10.7	6.26×10^{-4}	1.42×10^{-3}	3.98×10^{-4}	8.15×10^{-4}	7.51×10^{-4}
10.9	6.43×10^{-4}	1.55×10^{-3}	5.66×10^{-4}	7.66×10^{-4}	1.05×10^{-3}
11.1	7.24×10^{-4}	1.78×10^{-3}	8.03×10^{-4}	1.13×10^{-3}	9.78×10^{-4}
11.3	9.45×10^{-4}	1.55×10^{-3}	5.48×10^{-4}	9.06×10^{-4}	1.03×10^{-3}
11.5	8.47×10^{-4}	1.38×10^{-3}	8.22×10^{-4}	1.18×10^{-3}	8.21×10^{-4}
11.7	7.65×10^{-4}	1.86×10^{-3}	7.96×10^{-4}	1.17×10^{-3}	1.18×10^{-3}
11.9	9.93×10^{-4}	2.62×10^{-3}	1.21×10^{-3}	1.27×10^{-3}	1.26×10^{-3}
12.1	8.43×10^{-4}	2.19×10^{-3}	9.87×10^{-4}	1.13×10^{-3}	1.42×10^{-3}
12.3	1.15×10^{-3}	1.94×10^{-3}	8.81×10^{-4}	9.51×10^{-4}	1.44×10^{-3}
12.5	1.01×10^{-3}	2.47×10^{-3}	1.05×10^{-3}	1.34×10^{-3}	1.26×10^{-3}
12.7	1.35×10^{-3}	2.65×10^{-3}	1.07×10^{-3}	1.53×10^{-3}	1.22×10^{-3}
12.9	1.22×10^{-3}	2.09×10^{-3}	1.13×10^{-3}	1.46×10^{-3}	1.19×10^{-3}
13.1	1.37×10^{-3}	2.41×10^{-3}	1.22×10^{-3}	1.48×10^{-3}	1.56×10^{-3}
13.3	1.38×10^{-3}	2.62×10^{-3}	1.16×10^{-3}	1.67×10^{-3}	1.41×10^{-3}
13.5	9.91×10^{-4}	2.53×10^{-3}	1.03×10^{-3}	1.49×10^{-3}	1.50×10^{-3}
13.7	9.41×10^{-4}	2.94×10^{-3}	8.43×10^{-4}	1.89×10^{-3}	1.71×10^{-3}
13.9	1.16×10^{-3}	3.19×10^{-3}	1.16×10^{-3}	1.69×10^{-3}	1.82×10^{-3}

Table B.3: Acceptance of E888 detector based on a flat momentum spectrum in the VDR. These values can be used to find the acceptance of this experiment for any initial H production momentum spectra (see Section 10.3).

m_H(GeV/c^2)	2.09	2.12	2.15	2.18	2.21
τ (ns)	115	72.5	5	4	3.125
p (GeV/c)	*Acceptance as a function of momentum, continued*				
14.1	1.12×10^{-3}	2.93×10^{-3}	1.01×10^{-3}	2.26×10^{-3}	1.86×10^{-3}
14.3	9.83×10^{-4}	3.09×10^{-3}	1.13×10^{-3}	2.18×10^{-3}	2.25×10^{-3}
14.5	8.99×10^{-4}	2.55×10^{-3}	1.13×10^{-3}	1.91×10^{-3}	2.07×10^{-3}
14.7	1.45×10^{-3}	2.84×10^{-3}	1.44×10^{-3}	1.53×10^{-3}	2.17×10^{-3}
14.9	7.89×10^{-4}	2.95×10^{-3}	8.87×10^{-4}	1.85×10^{-3}	2.14×10^{-3}
15.1	1.00×10^{-3}	2.77×10^{-3}	1.33×10^{-3}	1.99×10^{-3}	1.80×10^{-3}
15.3	9.45×10^{-4}	2.68×10^{-3}	1.55×10^{-3}	2.02×10^{-3}	1.97×10^{-3}
15.5	8.61×10^{-4}	2.77×10^{-3}	1.28×10^{-3}	2.18×10^{-3}	2.28×10^{-3}
15.7	9.20×10^{-4}	3.09×10^{-3}	1.31×10^{-3}	1.74×10^{-3}	1.91×10^{-3}
15.9	1.03×10^{-3}	2.30×10^{-3}	1.10×10^{-3}	1.70×10^{-3}	2.47×10^{-3}
16.1	8.45×10^{-4}	3.13×10^{-3}	1.04×10^{-3}	1.85×10^{-3}	2.11×10^{-3}
16.3	8.08×10^{-4}	2.79×10^{-3}	1.28×10^{-3}	1.56×10^{-3}	1.73×10^{-3}
16.5	1.02×10^{-3}	3.35×10^{-3}	1.22×10^{-3}	1.57×10^{-3}	2.01×10^{-3}
16.7	9.65×10^{-4}	2.36×10^{-3}	1.41×10^{-3}	1.74×10^{-3}	2.39×10^{-3}
16.9	8.32×10^{-4}	2.46×10^{-3}	1.38×10^{-3}	1.68×10^{-3}	1.99×10^{-3}
17.1	9.27×10^{-4}	2.49×10^{-3}	1.26×10^{-3}	1.80×10^{-3}	1.87×10^{-3}
17.3	9.04×10^{-4}	2.45×10^{-3}	1.36×10^{-3}	1.79×10^{-3}	2.20×10^{-3}
17.5	8.46×10^{-4}	2.40×10^{-3}	1.47×10^{-3}	1.91×10^{-3}	2.13×10^{-3}
17.7	9.45×10^{-4}	1.89×10^{-3}	1.07×10^{-3}	1.64×10^{-3}	2.09×10^{-3}
17.9	7.87×10^{-4}	2.19×10^{-3}	9.65×10^{-4}	1.77×10^{-3}	1.98×10^{-3}
18.1	7.62×10^{-4}	2.49×10^{-3}	1.26×10^{-3}	1.94×10^{-3}	1.52×10^{-3}
18.3	6.82×10^{-4}	2.37×10^{-3}	9.85×10^{-4}	1.64×10^{-3}	2.34×10^{-3}
18.5	9.40×10^{-4}	2.40×10^{-3}	9.63×10^{-4}	1.60×10^{-3}	1.97×10^{-3}
18.7	7.06×10^{-4}	2.07×10^{-3}	1.12×10^{-3}	1.70×10^{-3}	2.03×10^{-3}
18.9	6.20×10^{-4}	2.36×10^{-3}	1.03×10^{-3}	1.63×10^{-3}	1.83×10^{-3}
19.1	5.79×10^{-4}	1.85×10^{-3}	8.36×10^{-4}	1.69×10^{-3}	1.62×10^{-3}
19.3	6.42×10^{-4}	1.85×10^{-3}	8.13×10^{-4}	1.28×10^{-3}	1.63×10^{-3}
19.5	5.66×10^{-4}	1.61×10^{-3}	9.04×10^{-4}	1.47×10^{-3}	1.77×10^{-3}
19.7	4.03×10^{-4}	1.99×10^{-3}	9.09×10^{-4}	1.33×10^{-3}	1.48×10^{-3}
19.9	2.42×10^{-4}	1.97×10^{-3}	7.54×10^{-4}	1.30×10^{-3}	1.90×10^{-3}

Table B.4: Acceptance of E888 detector based on a flat momentum spectrum in the VDR, continued.

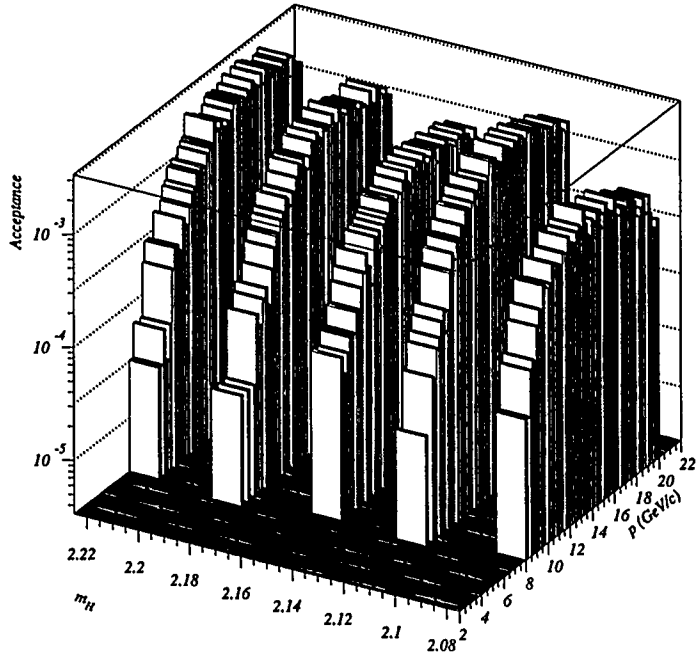

Figure B.1: Acceptance of E888 detector based on a flat momentum spectrum in the VDR, corresponding to the mass and lifetime values shown in Table B.1.

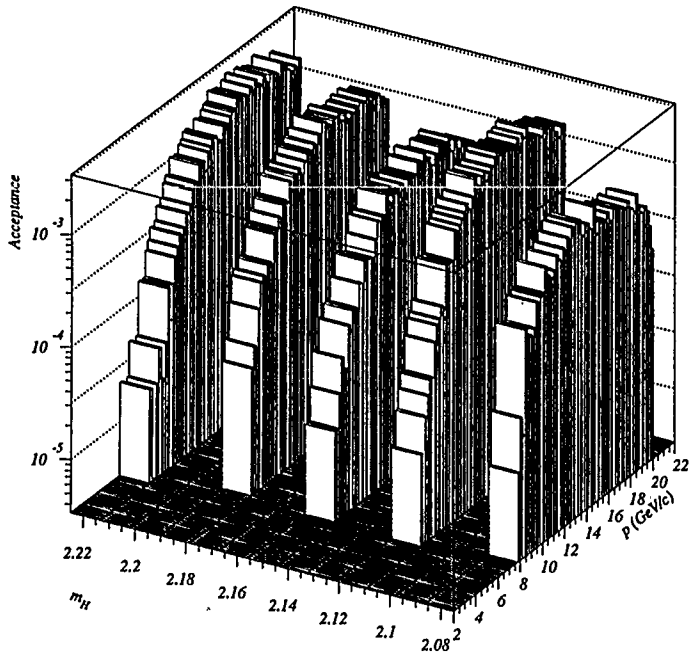

Figure B.2: Acceptance of E888 detector based on a flat momentum spectrum in the VDR, corresponding to the mass and lifetime values shown in Table B.3.

Appendix C

BNL E888 Collaboration

Brookhaven National Laboratory, *Upton, NY 11973*
Morgan May, Sebastian N. White

University of California, *Irvine, California 92717*
William R. Molzon

University of California, *Los Angeles, California 90024*
Robert D. Cousins

Princeton University, *Princeton, NJ 08544*
Val L. Fitch, Josh R. Klein, Alan J. Schwartz

Stanford University, *Stanford, California 94309*
Milind V. Diwan, Karl Ecklund, George M. Irwin, Stan G. Wojcicki

Temple University, *Philadelphia, Pennsylvania 19122*
Steve H. Kettell, John Belz, Virgil L. Highland, A. Trandafir

The University of Texas at Austin, *Austin, Texas 78712*
Gerald W. Hoffmann, Karol Lang, Jim McDonough, Peter J. Riley,
Jack L. Ritchie, Brent Ware, Steve Worm

College of William and Mary, *Williamsburg, Virginia 23187*
Morty Eckhause, Dayle Hancock, Chris Hoff, John R. Kane, Yunan Kuang,
Robert Martin, Robert E. Welsh, Michael T. Witkowski

References

[1] R.L. Jaffe, "Perhaps a Stable Dihyperon,"
Phys. Rev. Lett. **38**, 177 (1977).

[2] J.F.Donoghue, E. Golowich, and B.R. Holstein, "Weak decays of the H dibaryon," Phys. Rev. D. **34**, 3434 (1986).

[3] C. Guaraldo, "The case of the H particle," in *Hadronic Physics at Intermediate Energy II*, edited by T. Bressani, B. Minetti, G. Pauli, (Elsevier, Holland, 1987).

[4] K.F. Liu and C.W. Wong, "MIT Bag Model with Center-of-Mass Correction," Phys. Lett. **113B**, 1 (1982).

[5] P.J.Mulders and A.W.Thomas, "Pionic Corrections and Multi-quark bags," J. Phys. G **9**, 1159 (1983).

[6] J.L. Rosner, "SU(3) breaking and the H dibaryon,"
Phys. Rev. D. **33**, 2043 (1986).

[7] E. Golowich and T. Sotirelis, "$O(\alpha_s^2)$ mass contributions to the H dibaryon in a truncated bag model," Phys. Rev. D. **46**, 354 (1992).

[8] Y. Iwasaki, T. Yoshie, and Y.Tsuboi, "The H Dibaryon in Lattice QCD," Phys. Rev. Lett. **60**, 1371 (1988).

[9] A.P. Balachandran, *et al.*, "Doubly Strange Dibaryon in the Chiral Model," Phys. Rev. Lett. **52**, 887 (1984).

[10] G.L. Thomas and N.N. Scoccola, "Dibaryons as axially symmetric skyrmions," Nucl. Phys. **A575**, 623 (1994).

[11] I.R. Klebanov and K.M. Westerberg, "A Simple Description of Strange Dibaryons in the Skyrme Model," Princeton PUPT-1555, hep-ph/9508279, August 1995.

[12] N. Kodama, M. Oka and T. Hatsuda, "H dibaryon in the QCD sum rule," Nucl. Phys. **A580**, 445 (1994).

[13] S. Takeuchi and M. Ota, "Can the H dibaryon survive instantons?," Phys. Rev. Lett. **66**, 1271 (1991).

[14] D. Pal and J.A. McGovern, "Mass of the dihyperon in the colour-dielectric model," J. Phys. G **18**, 593 (1992).

[15] J.F.Donoghue, E. Golowich, and B.R. Holstein, *Dynamics of the Standard Model* (Cambridge University Press, Cambridge, England, 1994).

[16] R.L. Jaffe and F.E. Low, "Connection between quark-model eigenstates and low-energy scattering," Phys. Rev. D. **19**, 2105 (1979).

[17] A.M. Badalyan and Y.A. Simonov, "The hadronic shift and the probability of producing the dilambda state H,"
Sov. J. Nucl. Phys. **36**, 860 (1982).

[18] R.D. Cousins and J.R. Klein, "Estimate of H dibaryon production through $\Lambda\Lambda$ coalescence in $p+A$ collisions," KL-448-H, UCLA HEP 1994-001, (1994).

[19] R.D. Cousins and J.R. Klein, "Estimate of H dibaryon production through $\Lambda\Lambda$ coalescence in $p+A$ collisions," submitted to Phys. Rev. D. (1995)

[20] F.S. Rotondo, "Coalescence estimate of H dibaryon production in high-energy $p+A$ collisions," Phys. Rev. D. **47**, 3871 (1993).

[21] B.A. Cole, M. Moulson, and W.A. Zajc, "Coalescence production of H^0's in p-A collisions," Phys. Lett. **B350**, 147 (1995).

[22] H. Sorge, *et al.*, "Relativistic Quantum Molecular Dynamics Approach to Nuclear Collisions at Ultrarelativistic Energies," Nucl. Phys. **A498**, 567 (1989).

[23] A.T.M Aerts and C.B. Dover, "H dibaryon formation from Ξ^- atoms," Phys. Rev. D. **29**, 433 (1984).

[24] R.L. Jaffe, "$q^2\bar{q}^2$ resonances in the baryon-anti-baryon system," Phys. Rev. D. **17**, 1444 (1978).

[25] M.W. Beinker, B.C. Metsch, and H.R. Petry, "Bound $q^2\bar{q}^2$ states in a constituent quark model," hep-ph/9505215, submitted to Z. Phys. A (1995).

[26] T. Barnes, "The Status of Molecules," ORNL-CCIP-94-08/RAL-94-056, hep-ph/9406215 (1994).

[27] V.A. Dorofeev, *et al.*, (SPHINX Collaboration), "The search for heavy pentaquark exotic baryons with hidden strangeness in the $p+N \rightarrow (p\phi)+N$ and $p+N \rightarrow (\Lambda(1520)K^+)+N$ reactions at $E(p)=70$ GeV," Phys. At. Nucl. **57**, 227 (1994).

[28] By Y. Oh, B. Park, and D. Min, "Pentaquark exotic baryons in the Skyrme model," Phys. Lett. **B331**, 362 (1994).

[29] J. Madsen, "Physical properties of strangelets," in *Workshop on Strangeness in Hot Hadronic Matter: Strangeness '95* Tucson, IFA-95-03, hep-ph/9502242 (1995).

[30] D. Beavis, *et al.*, (BNL E878 Collaboration), "Search for New Metastable Particles Produced in Au + Au Collisions at 10.8A GeV/c," Phys. Rev. Lett. **75**, 3078 (1995).

[31] H.J. Crawford and C.H. Greiner, "The search for strange matter," Scientific American , 72 (January 1994).

[32] E. Farhi and R.L. Jaffe, "Strange Matter," Phys. Rev. D. **30**, 2379 (1984).

[33] J. Schaffner, *et al.*, "Strange hadronic matter," Phys. Rev. Lett. **71**, 1328 (1993).

[34] J. Madsen, ed., *Strange Quark Matter in Physics and Astrophysics*, Nucl. Phys. (Proc. Supp.) **B24**, (1991).

[35] E. Witten, "Cosmic separation of phases," Phys. Rev. D. **30**, 272 (1984).

[36] V.L. Fitch, "Strange Matter," in *Proc. of the 10th Hawaii Conf. in HEP*, (University of Hawaii Press, 1985).

[37] F. Flam, "A New Form of Strange Matter and New Hope for Finding It," Science **262**, 177 (1993).

[38] H.R. Gustafson, *et al.*, "Search for New Massive Long-Lived Neutral Particles," Phys. Rev. Lett. **37**, 474 (1976).

[39] A.S. Carroll, *et al.*, "Search for Six-Quark States," Phys. Rev. Lett. **41**, 777 (1978).

[40] B.A. Shahbazian, *et al.*, Zeitshrift fur Physik **151**, C39 (1988).

[41] B.A. Shahbazian, *et al.*, "Evidences for $S = -2$ neutral H and positively charged H^+ heavy stable dibaryons," Phys. Lett. **B316**, 593 (1993).

[42] A.N. Alekseev, *et al.*, Yad. Fiz. **52**, 1612 (1990).

[43] S. Aoki, *et al.*, "Search for the H Dibaryon in (K^-, K^+) Reactions," Phys. Rev. Lett. **65**, 1729 (1990).

[44] H. Bäwolff, *et al.*, "Search for neutral dibaryon with strangeness -2 in high tranverse momentum π^- nucleus interactions at 40 GeV/c," Ann. Physik Leipzig **43**, 407 (1986).

[45] J. Belz, *et al.*, "Search for Diffractive Dissociation of a Long-Lived H Dibaryon," submitted to Phys. Rev. Lett. (1995)

[46] J.R. Klein, "A Strange Matter: Searching for the H Dibaryon," Princeton HEP/94/09, Ph.D dissertation, Princeton University, June 1994.

[47] M. Danysz, *et al.*, "The identification of a double hyperfragment," Nucl. Phys. **49**, 121 (1963).

[48] D. Prowse, *et al.*, "$_{\Lambda\Lambda}$He^6 Double Hyperfragment," Phys. Rev. Lett. **17**, 782 (1966).

[49] S. Aoki, *et al.*, "Evidence of weak decay of heavy double hypernuclei," Prog. Th. Phys. **85**, 951 (1991).

[50] S. Aoki, *et al.*, "Direct observation of sequential weak decay of a double hypernucleus," Prog. Th. Phys. **85**, 1287 (1991).

[51] C.B. Dover, D.J. Millener, and A. Gal, "Interpretation of a double hypernucleus event," Phys. Rev. C. **44**, 1905 (1991).

[52] R.H. Dalitz, *et al.*, "The identified $\Lambda\Lambda$ hypernuclei and the predicted H particle," Proc. Roy. Soc. London **A426**, 1 (1989).

[53] H. Ejiri, *et al.*, "Search for the H Dihyperon by double weak decay of nuclei," Phys. Lett. **B228**, 24 (1989).

[54] R. Longacre, *et al.*, (E810 Collaboration), "H_0 candidates from the decay $H_0 \rightarrow \Sigma^- p$, observed in heavy ion collisions with $14.6 \times A$ GeV/c Si beam on Pb target," undated communication.

[55] A.J. Schwartz, "Searching for the H dibaryon at Brookhaven," Princeton HEP 93-08, KL-444H, in *Contribution to the XXI Summer Institute on Particle Physics, SLAC*, Stanford (1993).

[56] C.A. Pruneau, "Searches for Strange Matter," in *Proc. of the 8th meeting, Division of Particles and Fields of the American Physical Society* 1336 (1994).

[57] P. Buchholz, *et al.*, (E791 Collaboration), "Recent results of BNL E791: Study of very rare K_L^0 decays," in *Mainz 1988, Proceedings, Proton-antiproton interactions and fundamental symmetries,* Nucl. Phys. B (Proc. Suppl.) **8**, 356 (1989).

[58] Particle Data Group, Review of Particle Properties, Baryon Full Listings, Phys. Rev. D. **50**, (1994).

[59] K. Arisaka, *et al.*, (E791 Collaboration), "Improved Upper Limit on the Branching Ratio B($K_L^0 \rightarrow \mu^{\pm}e^{\mp}$)," Phys. Rev. Lett. **70**, 1049 (1993).

[60] K. Arisaka, *et al.*, (E791 Collaboration), "Improved Sensitivity in a Search for the Rare Decay $K_L^0 \rightarrow e^+e^-$," Phys. Rev. Lett. **71**, 3910 (1993).

[61] A. Heinson, *et al.*, (E791 Collaboration), "Measurement of the Branching Ratio for the Rare Decay $K_L^0 \rightarrow \mu^+\mu^-$," Phys. Rev. D. **51**, 985 (1995).

[62] J. Urheim, "Experimental Search for the Decay $K_L^0 \rightarrow \mu e$," Ph.D dissertation, University of Pennsylvania, 1990.

[63] D. Wagner, "Experimental Search for the Rare Decay of the Long-Lived Neutral Kaon to a Muon and Electron, " Ph.D dissertation, University of California-Los Angeles, UCLA HEP-90-006, KL-311, 1990.

[64] K. Biery, "A measurement of the decay rate of the long-lived neutral kaon to two muons," Ph.D dissertation, Stanford University, 1991.

[65] J. Belz, "A Search for the Decay of the Long-Lived Neutral Kaon into an electron and Positron," Ph.D dissertation, Temple University, May 1993.

[66] J.E. Brau, J.E., *et al.*, "The Lead Glass Columns: A Large Shower Detector at the SLAC Hybrid Facility," Nucl. Instr. Meth. **196**, 403 (1982).

[67] B. Ware, "Radiation Damage in the Lead-Glass," KL-368, 1991.

[68] R. Cousins, *et al.*, "Fast parallel pipelined readout architecture for a completely flash digitizing system with multi-level trigger," Nucl. Inst. Meth. **A277**, 517 (1989).

[69] K. Biery, D. Ouimette, and J. Ritchie, "A Fast Integrating Eight-Bit Bilinear ADC," IEEE Trans. Nucl. Sci **36**, 646 (1989).

[70] R. Cousins, C. Friedman, and P. Mélèse, "32-Channel 6-bit TDC with 2.5 ns Least Count," IEEE Trans. Nucl. Sci. **36**, 650 (1989).

[71] A. Schwartz and D. Ouimette, "Stanford TDCs," KL-243, 1989.

[72] D. Wagner, "Some Monte Carlo Documentation," KL-173, September 1988.

[73] W. Molzon, S. Imlay, "The QFT fitting package and kinematic resolutions," KL-236, 1989.

[74] B. Ware, "E888 H-decay Pass 1 & 2 Production," KL-452H, 1994.

[75] A. Beretvas, *et al.*, "Production of Ξ^0 and $\bar{\Xi}^0$ hyperons Phys. Rev. D. 34, 53 (1986).

[76] P. Skubic, *et al.*, "Neutral-strange-particle production by 300-GeV protons," Phys. Rev. D. 18, 3115 (1978).

[77] F. Abe, *et al.*, "Inclusive Λ^0 production by 12-GeV protons on nuclear targets," Phys. Rev. D. 30, 1861 (1984).

[78] F. Abe, *et al.*, "Production of neutral strange particles K^0_S and Λ^0 by 12-GeV protons on nuclear targets," Phys. Rev. D. 36, 1302 (1987).

[79] V. Biobel, *et al.*, "Inclusive Neutron and Lambda production in Proton-Proton interactions at 12 and 24 GeV/c," Nucl. Phys. B135, 379 (1978).

[80] J.P. Denisov, et al., "Absorption cross sections for pions, kaons, protons, and antiprotons on complex nuclei in the 6 to 60 GeV/c momentum range," Nucl. Phys. B61, 62 (1973).

[81] A. Schwartz, "An E888 Limit on the Total *H* Cross Section," KL-476H, 1995.

[82] J. Belz, *et al.*, "Search for the Weak Decay of an *H* Dibaryon," submitted to Phys. Rev. Lett. (1995)

Vita

Carlton Brent Ware was [redacted]. His parents are Myrtle Alice Ware and Wayne Allen Ware. After graduating from Spearman High School in Spearman, Texas in 1980, Brent attended Texas Tech University in Lubbock, Texas, graduating with a Bachelor of Science in Electrical Engineering in 1984. He worked in the Corporate Research Department of Recognition Equipment, Inc., from May 1984 to August 1988, doing research in neural networks, pattern recognition, digital signal processing, and designing cameras for high-speed optical character recognition systems. During this time, he attended The University of Texas at Arlington, and received a Master of Science in Electrical Engineering in December 1988. In August 1988, he began attending The University of Texas at Austin to study physics. His publications are:

An Analysis of a Nonlinear Neural Network, Masters Thesis, The University of Texas at Arlington, August 1988.

Design and Performance of A Compact Beam Stop for a Rare Kaon Decay Experiment, E871 collaboration, J. Belz, *et al.*, to be submitted to Nucl. Instr. and Meth.

Search for Diffractive Dissociation of a Long-lived H Dibaryon, E888 collaboration, J. Belz, *et al.*, submitted to Phys. Rev. Lett., July 1995.

Search for Weak Decays of a Long-Lived H Dibaryon, E888 Collaboration, J. Belz, *et al.*, submitted to Phys. Rev. Lett., October 1995.

Permanent address: 1800 Palmwood Cove
Austin, Texas 78757

This Dissertation was typeset with LaTeX[‡] by the author.

[‡]LaTeX is a document preparation system developed by Leslie Lamport as a special version of Donald Knuth's TeX Program.